Combined STM/AFM with functionalized tips applied to individual molecules

Chemical reactions, geometric structure and charge distribution

Dissertation zur Erlangung des Doktorgrades
der Naturwissenschaften (Dr. rer. nat.)
der Fakultät für Physik
der Universität Regensburg

vorgelegt von

Florian Albrecht
aus Passau

2016

Die Arbeit wurde von Prof. Dr. Jascha Repp angeleitet.
Das Promotionsgesuch wurde am 5. Juli 2016 eingereicht.
Das Promotionskolloquium fand am 27. Oktober 2016 statt.

Prüfungsausschuss:	Vorsitzender:	PD Dr. Falk Bruckmann
	1. Gutachter:	Prof. Dr. Jascha Repp
	2. Gutachter:	Prof. Dr. Josef Zweck
	weiterer Prüfer:	Prof. Dr. Christoph Strunk

Abstract

Scanning probe microscopy (SPM) methods allow for investigations of the atomistic world in real space. While scanning tunneling microscopy (STM) is sensitive to the electronic structure of the sample, its geometry can be explored by means of atomic force microscopy (AFM). Suitable functionalization of the AFM tip enables resolving the chemical structure of individual molecules at low temperatures in ultrahigh vacuum. Combining STM and AFM detection schemes in one setup facilitates simultaneous examination of the electronic and the geometric structure of single (molecular) adsorbates.

This work employs SPM with functionalized tips on individual molecules in three topics:

The capability of structure determination is widened to non-planar and strongly deformed molecules. The required information is deduced from either full three-dimensional data sets or from images along the adsorbed molecule's symmetry planes that are perpendicular to the sample surface.

On-surface chemical reactions are studied in great detail. For two exemplary cases, we investigate the reaction pathway of a thermally activated planarization reaction, and we examine the interplay of electronic and geometric structure in the tip-induced formation of a metal-organic complex.

Finally, we use AFM to image the charge distribution in individual metal-organic molecules with polar bonds. Introducing a novel spectroscopy technique we resolve charge contrast along individual polar bonds.

Contents

1 Introduction

The invention of the scanning tunneling microscope (STM) by G. Binnig and coworkers paved the way for imaging individual atoms in real space [1]. The capability of STM to move single adsorbates on the sample surface allows for the controlled build-up of atomic structures [2]. Scanning tunneling spectroscopy (STS) enables the detection of the electronic structure of the sample [3]. Using ultra-thin insulators as decoupling layer facilitates probing the unperturbed electronic structure and orbital shape of individual adsorbates [4]. Hence, STM enables experiments and sample design on the single atom level but is limited in two ways: On the one hand, it requires a conducting sample. On the other hand, it probes the electronic structure that, in general, must not be interpreted in terms of the sample's geometry only.

To get access to the geometry on the atomic scale, G. Binnig et al. introduced the atomic force microscope (AFM) [5]. The final step to directly resolve the chemical structure of single molecular adsorbates was introduced by L. Gross and coworkers [6]: Functionalizing the tip with a single carbon monoxide molecule facilitates scanning the sample at such small distances that allow for recording contrast variations on the atomic length scale in individual organic molecules in real space. The qPlus sensor design enables simultaneous STM and AFM experiments on one and the same sample [7].

The combination with single molecular chemistry [8] allows for a detailed characterization of chemical on-surface reactions by means of scanning probe microscopy (SPM). Such reactions can be activated

by the SPM tip [9] or by thermal annealing of the sample [10].

Apart from geometric structure determination, AFM is utilized to detect charges localized on the sample surface with very high lateral resolution [11, 12]. The boost in resolution due to suitable tip functionalization enabled imaging the charge distribution within individual organic molecules [13].

Due to its impressive resolution, AFM with functionalized tips is widely applied nowadays. However, the molecules under investigation so far were mainly planar and adsorbed almost parallel to the sample surface.

Current methods are limited in mapping the charge distribution. Reducing the tip-sample spacing to increase the resolution turned out to be insufficient to detect charges localized on individual atoms in single molecules [14].

There are three main goals of this thesis:

Structure determination of non-planar molecules

We analyze the structure of a helical molecule from a three-dimensional data set in chapter 5. We also determine subtle conformational differences in the structure of two well studied molecular reference systems in chapter 6.

Investigation of on-surface chemical reactions

In chapter 5 we investigate the reaction pathway of a thermally activated on-surface reaction. We also examine the interplay of geometric and electronic coupling upon the tip-induced formation of a metal-organic complex in chapter 7.

Improvement of charge sensing to highest lateral resolution

We investigate intramolecular charge distributions in molecules with bonds of different polarity in chapter 8. We introduce a novel spectroscopy technique that allows us to resolve contrast along individual polar bonds. In chapter 9 we directly compare two different charge detection methods — an established AFM-based one and one that employs the decay of the tunneling current with tip-sample spacing.

2 Theory background

A brief introduction to the basics of the experiments is given in this chapter. Scanning tunneling microscopy is introduced, the basic data acquisition modes and their interpretations are provided. Atomic force microscopy will be explained from its first realization to the herein applied frequency modulation mode. Finally, AFM-based Kelvin probe force methods will be introduced and some relevant aspects of their contrast formation and data interpretation will be pointed out.

2.1 Scanning Tunneling Microscopy

In a classical particle picture, electrons are confined to the volume of a metallic body. In a quantum mechanical picture the electron is represented by its wave function, which may penetrate the volume outside a metal — like an evanescent wave. The decay length of this wave is in the range of Ångstroms. To probe this wave, another solid body — later on called tip — needs to be very close (typically within $\approx 1\,\mathrm{nm}$) to the first one — called sample. To generate a net current flowing from one body to the other, a potential difference — the bias voltage V — is applied . This allows electrons to cross the (small) gap between the two bodies — the electron can tunnel through the barrier (see schematics in Fig. 2.1).

In 1982 G. Binnig et al. demonstrated tunneling through a mechanically controlled vacuum gap [15]. These experiments — not yet generating images — showed that the tunneling current I was exponentially

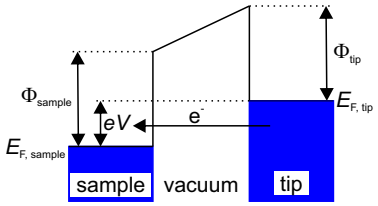

Figure 2.1: Schematic energy levels for tunneling: At low temperatures all electronic states below the Fermi level in a metallic sample and tip are filled. Applying e.g. positive bias voltage V to the sample with respect to the tip allows electrons to tunnel from occupied states in the tip to unoccupied states in the sample.

decaying with the distance z between tip and sample as

$$I(z) \cong I_0 e^{-2\kappa z}, \tag{2.1}$$

like predicted by theory for a one-dimensional tunneling barrier [16]. I_0 denotes a constant prefactor of the tunneling current and

$$\kappa = \frac{\sqrt{2m_\mathrm{e}\phi_\mathrm{b}}}{\hbar} \tag{2.2}$$

is the inverse of the decay constant (m_e denotes the mass of an electron and $\hbar$ the reduced Planck constant). For a tunneling setup, the barrier height ϕ_b is given by the work function and is typically about 5 eV. Hence κ is of the order of 1/Å and the tunneling current changes by an order of magnitude when the tip-sample distance is altered by one Ångstrom. For homogeneous and flat samples the decay of the tunneling current with tip-sample distance can provide qualitative information on the work function of the sample [15]. For samples with pronounced topographic corrugation a (direct) interpretation of the inverse of the decay constant in terms of work function is not possible (see chapter 9).

2.1.1 STM imaging

Shortly after introducing tunneling through a controlled gap, G. Binnig and coworkers were the first to use the tunneling electrons for imaging conducting surfaces on the atomic scale [1, 17, 18] — the STM was born. The theory for the image contrast is based on methods initially developed by J. Bardeen in 1961 [19] and became applicable for STM after J. Tersoff and D. R. Hamann introduced the so-called Tersoff Hamann approximation [20, 21]: Assuming a spherically symmetric wave function of the tip, topography images recorded in constant-current mode can be interpreted in terms of contours of constant local density of states at the sample.

2.1.2 Scanning Tunneling Spectroscopy

As illustrated in Fig. 2.1 electrons can tunnel in an energy range between Fermi level and the applied bias voltage. Hence, the convolution of the density of states of the tip and the sample integrated over the entire bias voltage window gives the net current [22]. Assuming a flat density of states at the tip within the voltage range of the measurement the differential conductance signal dI/dV provides a measure for the local density of states at the sample [3]. This signal can be detected using a lock-in amplifier while sweeping the applied bias voltage with the tip being at a fixed position in real space:

$$I\left(V_0 + V_{\mathrm{mod}} cos(\omega t)\right) \cong I(V_0) + \frac{dI(V_0)}{dV} V_{\mathrm{mod}} cos(\omega t) \tag{2.3}$$

Such scanning tunneling spectroscopy (STS) data recorded on molecules adsorbed on a clean metal surface does, however, not directly provide molecular electronic states. Due to the hybridization of molecular states with the energy levels of the conducting substrate underneath, STS spectra effectively provide information of the entire system [23,

24]. To deduce molecular states and to image molecular orbitals, decoupling of molecules from the metallic substrate is essential. Ultrathin alkali-halide films consisting of only a few atomic layers provide sufficient decoupling while still being thin enough to perform STM and STS experiments [4].

The STM technique allows imaging and spectroscopy with atomic resolution in real space. Yet, there are two main drawbacks of STM: First, the image contrast is a convolution of topography and electronic structure of the sample, which prohibits a direct interpretation of STM topographs in terms of the sample's geometry. Second, STM is limited to (semi-)conducting samples that are required for the tunneling current to flow. The atomic force microscope — which will be introduced in the next section — can overcome these limitations.

2.2 Atomic Force Microscopy

Inspired by the unprecedented lateral and vertical resolution of STM the atomic force microscope (AFM) was invented by G. Binnig and coworkers [5]. This sections will introduce the operation of AFM — first, the originally proposed static mode and then the dynamic mode that is used for the experiments presented in this thesis.

2.2.1 Static AFM

It is well known that a spring is an ideal force sensor. According to Hooke's law [25], the force F acting on a spring with stiffness k_s that causes a deformation Δl in length of the spring is given by $F = k_\mathrm{s} \cdot \Delta l$. To detect small (inter-atomic) forces with such a spring sensor, very high sensitivity in the deflection of the sensor is required. Since the tunneling current changes drastically with the spacing between sample

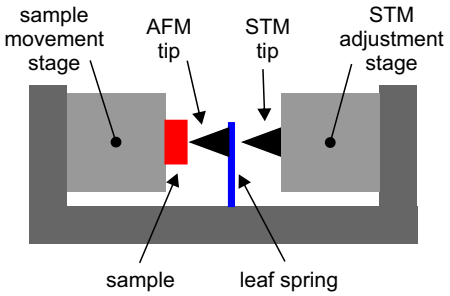

Figure 2.2: Schematic of the first AFM setup: The force acting on the AFM tip in front of the sample deflects the very soft leaf spring the AFM tip is attached to. This deflection is detected by an STM junction. Figure after [5].

and tip (see section 2.1) STM allows extremely sensitive deflection measurements.

Applying this basic mechanics law to the enormous distance sensitivity of STM enabled the first AFM in 1986 [5]. A schematic is depicted in Fig. 2.2: The deflection of a very soft leaf spring the AFM tip is attached to is detected via an STM junction consisting of the leaf spring itself and a second tip. This way, the sample could be scanned by the AFM tip while the deflection of the leaf spring was recorded very precisely by the STM junction.

Referring to the first AFM publication by G. Binnig et al. [5] the force resolution of such a setup can be as small as $2 \cdot 10^{-16}$ N. Such a sensitivity is sufficient to detect inter-atomic forces between single atoms that are typically in the range of 10^{-9} N [6, 26]. Already one year after the birth of AFM, images with ultimate lateral resolution were recorded on a nonconducting sample [27] and with an insulating tip, too [28].

There is a major drawback of performing AFM in static mode. The AFM junction is mechanically unstable due to the very soft cantilever. Figure 2.3 illustrates this problem with the help of a very small AFM

model setup: The sample consisting of a single adatom on a flat substrate is probed by a pyramidal AFM tip that consists of four atomic layers only (see panel a). To achieve high lateral resolution, the last atom of the tip needs to be close to the sample. Apart electrostatics (see section 2.3), there are two main components of the tip-sample interaction forces in this distance regime (see Fig. 2.3c): On the one hand, there are interactions between each individual atomic layer of the tip and the adatom on the sample — of which the interaction of the last tip atom is of interest. These interactions are usually modeled by a Lennard-Jones (LJ) potential [29] and are depicted as dotted colored lines in Fig. 2.3c. On the other hand, the entire tip cluster interacts with the sample substrate. Due to the sample being semi-infinite, the latter one is of a more long range nature [30] and purely attractive in the distance regime of AFM experiments. As a consequence, the main contribution to the sum of all forces acting on the tip is dominated by the attractive interaction between sample and the entire tip (see solid black line in Fig. 2.3c). In the case of this very small model tip the total force becomes repulsive (positive) at very small tip-sample spacings. For a more realistic larger tip, the additional tip layers increase the attractive force and due to the small stiffness of the cantilever the tip may crash into the sample — called snap-in [31].

An oscillation of the cantilever perpendicular to the sample surface can prevent the risk of a snap-in. This method is refereed to as dynamic AFM and will be introduced in the next section.

2.2.2 Dynamic AFM

To increase the stability of an AFM setup the cantilever is actively oscillated perpendicular to the sample surface. The oscillatory deflection of the cantilever provides the required force to counteract the long-range attractive tip-sample interaction. When the tip is at the lower turn-around point (i.e. closest to the sample surface) the restoring

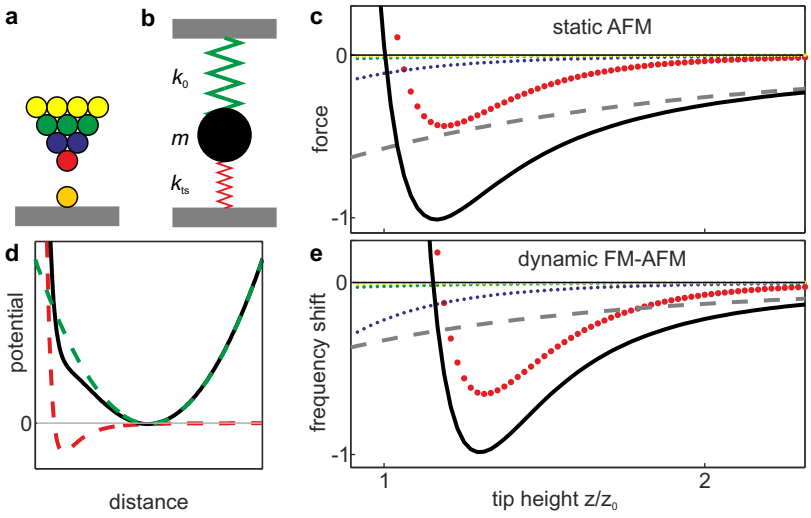

Figure 2.3: Comparison of signals in static and dynamic AFM: **a** Schematic drawing of an AFM tip above an adatom (orange) on a homogeneous sample surface (gray). Different colors for atoms within the tip represent different tip layers. **b** Schematic representation of an FM-AFM setup: The tip with effective mass m is connected to the cantilever having a mechanical stiffness k_0 (green spring). Close to the sample surface, there is an additional coupling k_{ts} between tip and sample (red spring). **c** Forces acting between an adatom on the sample and the different atomic layers of an AFM tip (dotted lines). The dashed gray line represents the van-der-Waals force between the entire tip model and the homogeneous sample. The sum of all forces is shown as solid black line. **d** Parabolic potential of a free cantilever (dashed green line) and a Lennard-Jones type potential for two atoms (dashed red line). A tip oscillating close to the sample surface experiences the sum of the two potentials in dynamic mode (black solid line). **e** Contributions to the Δf signal from different parts of the tip in FM-AFM in the small amplitude regime. Now, the interaction between the last most tip atom and the adatom on the sample dominants. (The color code is the same as in panel c.)

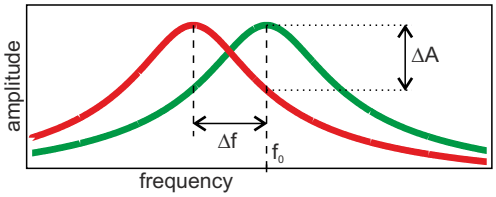

Figure 2.4: Frequency and amplitude modulation in dynamic AFM: The resonance spectrum of the free cantilever (green line) changes due to the tip-sample interaction (red line). In FM-AFM the cantilever is actively oscillated at its resonance frequency and the frequency shift Δf is the observed signal. In AM-AFM the cantilever is excited at its free resonance frequency f_0 and the change in the oscillation amplitude ΔA servers as signal.

force of the cantilever can avoid a snap-in, as long as

$$|F_{\text{attr}}^{\max}| \leq k_0 \cdot A. \tag{2.4}$$

Here, $F_{\text{attr}}^{\max}$ denotes the maximum attractive force between sample and tip. k_0 and A are the cantilever stiffness and the oscillation amplitude, respectively. Note that this holds even true for very soft cantilever.

Figure 2.3d illustrates the potentials for the dynamic AFM mode. The potential of the cantilever oscillator has a parabolic shape and is illustrated as dashed green line. The interaction between tip and sample is represented by an additional LJ-like potential (dashed red line). Cantilever and tip experience the sum of these to interactions, which is shown in black. Hence, the potential acting on the cantilever is different with the tip in proximity to the sample surface compared to the free oscillation. This will affect its oscillatory motion.

Figure 2.4 demonstrates the effect of the potential variation onto the cantilever dynamics: The green curve represents a resonance spectrum of the cantilever without tip-sample interaction. The peak position indicates the resonance frequency f_0. Due to the additional potential contribution from the substrate, the resonance spectrum changes (see

red line in Fig 2.4). Most importantly the resonance frequency has changed.

The two different physical quantities used in dynamic AFM are apparent in this Figure. In the first mode, the cantilever is excited at a constant frequency, e.g. at f_0, and the change in the oscillation amplitude (ΔA) is recorded — called amplitude-modulation AFM (AM-AFM). The second mode utilizes the change in the resonance frequency of the cantilever: The cantilever is excited at its resonance frequency and the oscillation amplitude is kept constant. The shift in resonance frequency Δf provides the signal — referred to as frequency-modulation AFM (FM-AFM). The latter is in general more demanding for the setup since it requires additional feedback loops as compared to AM-AFM. However, FM-AFM provides higher lateral resolution and sensitivity — especially when probing electrostatic tip-sample interactions (see section 2.3). Hence the derivation of the experimental signals in dynamic AFM will be restricted to FM-AFM.

Figure 2.3b shows a schematic of the relevant coupling strengths in dynamic AFM. The tip with effective mass m and the cantilever with stiffness k_0 represent a harmonic oscillator. The interaction between tip and sample is represented by an additional coupling k_{ts} and exemplified by the red spring. Since the tip experiences both couplings the resonance frequency will shift close to the sample surface as compared to the case when the tip is far way from the sample.

The conversion from tip-sample interaction potential to Δf signal is non trivial in general [32, 33]. In the case of constant small oscillation amplitudes and small k_{ts} as compared to k_0 a quick derivation yields a straightforward result: The free resonance frequency f_0 of an unperturbed harmonic oscillator (mass m and spring constant/coupling k_0) is given by

$$f_0 = \frac{1}{2\pi}\sqrt{\frac{k_0}{m}}. \tag{2.5}$$

In case of dynamic the entire coupling of the tip is given by the sum $k = k_0 + k_{\mathrm{ts}}$. Putting this sum into eqn. 2.5 in the limit of $k_0 >> k_{\mathrm{ts}}$ and doing a Taylor expansion of the square root yields:

$$\Delta f = f - f_0 \cong -f_0 \frac{k_{\mathrm{ts}}}{2k_0}. \tag{2.6}$$

Here, f denotes the resonance frequency of the cantilever with the tip being close to the sample surface. Finally, using the relation between spring constant k and force F ($k = \frac{\partial F}{\partial z}$), we get the relation between force and frequency shift:

$$\Delta f \cong -\frac{f_0}{2k_0}\frac{\partial F}{\partial z} = \frac{f_0}{2k_0}\frac{\partial^2 P}{\partial z^2}, \tag{2.7}$$

where P denotes the tip-sample interaction potential.

For large amplitudes, the experimentally observed Δf signal equals the force gradient averaged over the entire z-range of the oscillation cycle weighted by a semicircular weight function [34]. Hence, FM-AFM loses sensitivity to short range tip-sample interactions when operated at large amplitudes. As pointed out in eqn. 2.4, the amplitude required for stable operation is linked to the cantilever stiffness. For soft cantilevers, large amplitudes are required to achieve sufficient restoring forces to prevent the tip from crashing into the sample. However, large amplitudes have the downside of losing the sensitivity to short-range tip-sample interactions. Even though the use of stiff cantilevers reduces the relative frequency shift signal (see eqn. 2.6), it allows for stable small-amplitude operation with high sensitivity to short-range interactions.

Figure 2.3e depicts Δf signals for the previously discussed simple tip-sample model: Due to the slope of the force distance curve being the signal in FM-AFM, the entire tip-sample interaction is now dominated by the LJ-type interaction of the front-most tip atom and the sample adatom. Moreover, the relative weight of individual signal

contributions has shifted towards the two last atomic layers of the tip. The long-range attractive interaction of the entire tip with the sample substrate is less important than in the case of static AFM (compare dashed gray line in Fig. 2.3c and e).

FM-AFM — first introduced in 1990 [35] — has been shown to be capable of atomic resolution on semiconductor surfaces already in 1995 [36, 37]. The final step in terms of resolution and stability for the investigation of individual molecules is a suitable tip functionalization [6]. This method will be introduced in section 3.5.

2.3 Kelvin probe force methods

So far, we were mainly considering the investigation of the geometric structure of a sample. Additionally, AFM can sense other properties of the sample such as those originating from the distribution of electric charges. This is not very surprising since any charge experiences a force when exposed to an electric field, for example. The physics behind the charge detection will be introduced in this section:

Before discussing the charge detection by means of AFM, we will first introduce the concept of work function determination in a more general context, exemplified in Fig. 2.5. The situation for any two metallic bodies in close distance without electric contact is depicted in panel a: The energy levels of sample (left hand side) and probe (right hand side) align such, that the vacuum levels of both bodies match each other. Due to the difference in work function of sample and probe (Φ_s and Φ_p) the Fermi levels $E_{\mathrm{F,s}}$ and $E_{\mathrm{F,p}}$ are not aligned.

When the two bodies are in electrical contact (panel b) electrons flow until the Fermi levels of sample and probe align. Due to the flow of electrons, there are net charges on sample and probe that cause an electric field E in the gap and hence an extra attractive force.

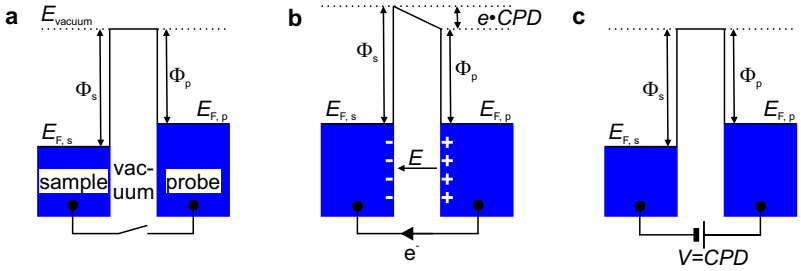

Figure 2.5: Energy levels for KPFM for two metallic surfaces facing each other: **a** No electric connection between sample and probe: Vacuum levels (E_{vacuum}) align and due to different work functions Φ_{s} and Φ_{p} of sample and probe, respectively, the Fermi energies of sample ($E_{\mathrm{F,\,s}}$) and probe ($E_{\mathrm{F,\,p}}$) are unequal. **b** Sample and probe electrically connected: Electrons flow until the Fermi energies are equal. This charge transfer causes an electric field E between sample and probe and hence an attractive force. **c** The situation of panel a is restored by applying an appropriate voltage between sample and probe that compensates the contact potential difference (CPD). Now the electrostatic interaction is minimized. Figure after [38].

Panel c demonstrated how an actively applied appropriate voltage between sample and probe restores the situation depicted panel a. Now, the vacuum levels are aligned again. The voltage $V = CPD$ (contact potential difference) required to minimize electrostatic interactions corresponds to the difference in work functions between sample and probe $CPD = \frac{1}{e}(\Phi_{\mathrm{s}} - \Phi_{\mathrm{p}})$.

The concept of work function and the idea of detecting differences in work function via the electric field between two metals dates back to 1898 and was initially introduced by Lord Kelvin [39]. He realized that an electric current flows when two different metals are brought in close vicinity, but not in direct contact (compare Fig 2.5b). The so-called Kelvin method utilizes a conducting oscillating probe. The electric field between sample and oscillating probe causes a capacitive current. Minimization of this current by applying an appropriate voltage between sample and probe provides the *global* contact potential

difference [40–43].

In 1991 J. Weaver et al. [11] and M. Nonnenmacher and coworkers [12] combined the Kelvin method with AFM and introduced Kelvin probe force microscopy (KPFM): Instead of detecting an oscillating capacitive current, the force between the sample and the oscillating probe is used as signal.

The electrostatic potential landscape of the sample is mapped by minimizing the bias dependent tip-sample interaction. The bias voltage of minimal interaction provides a qualitative measure of the sample's work function. The basics of the experiment can be rationalized from a capacitor model: First, we need the bias-dependent electrostatic energy $E_{\mathrm{es},\,0}$ of the tip-sample capacitor. Charges in tip and probe scale linearly with the voltage V and there are no net charges in tip nor probe for $V = CPD$, which defines the situation for zero energy. Since $E_{\mathrm{es},\,0}$ scales with the product of charges and applied potential, the electrostatic energy is given by

$$E_{\mathrm{es},\,0} = \frac{1}{2} C_0 \left(V - CPD\right)^2 . \tag{2.8}$$

Referring to equation 2.7, the force F_{es} and the frequency shift signal $\Delta f_{\mathrm{es},\,0}$ due to the electrostatic interaction in FM-AFM are given by

$$\begin{aligned} \Delta f_{\mathrm{es},\,0} &\propto \frac{\partial^2}{\partial z^2} E_{\mathrm{es},\,0} \propto \frac{\partial}{\partial z} F_{\mathrm{es}} \\ &\propto \frac{\partial}{\partial z} \left\{ \frac{1}{2} \frac{\partial C_0}{\partial z} \left(V - CPD\right)^2 \right\} \\ &\propto \frac{1}{2} \frac{\partial^2 C_0}{\partial z^2} \left(V - CPD\right)^2 . \end{aligned} \tag{2.9}$$

Applying an appropriate bias voltage $V^\star = CPD$ such that the Δf_{es} signal reaches its extremum $\Delta f^\star$ provides the CPD value. This can be achieved by either using a lock-in scheme and record the CPD values as an additional channel while imaging [11, 12] — also referred

to as Kelvin probe force *microscopy* (KPFM) — or by keeping the tip at a fixed position while sweeping the bias voltage and record an entire $\Delta f(V)$ spectrum (Kelvin parabola) [44] — called Kelvin probe force *spectroscopy* (KPFS). The latter is typically more time consuming and requires larger stability of the microscope in terms of drift. However, recording the entire $\Delta f(V)$ data set provides the possibility to check whether the spectra are parabolic in shape and hence the voltage dependence of the signal being merely electrostatic in origin. Deviations from a parabolic shape are typically observed for charging processes [45–48] or for ionic polarization (see chapter 8).

In case of inhomogeneous sample surfaces the concept of work function needs to be extended to the local scale. For example, charged adsorbates [49, 50] or step edges [51] affect the sample's potential landscape locally. This gives rise to the introduction of the *local* contact potential difference ($LCPD$) [52]. Reducing the lateral size of the probe by introducing a sharp tip allows for the detection of the $LCPD$ [11, 12, 53].

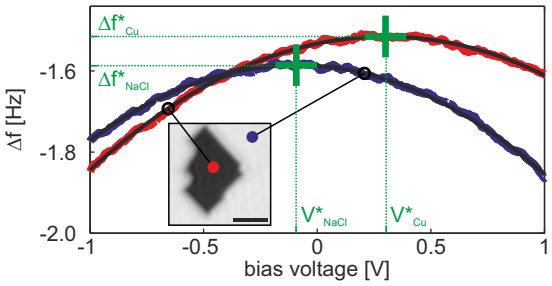

Figure 2.6: Example Kelvin parabolas on Cu(111) and bilayer NaCl/Cu(111): $\Delta f(V)$ spectra recorded on NaCl (blue) and on clean copper (red) in a void in a NaCl island. Parabolic fits to the experimental data are depicted in black. Green crosses indicate the maxima $\Delta f^\star$ of the two parabolas at positions of $V^\star$. Spectra where recorded at positions indicated in the STM topography image shown as inset. (Scale bar 50 Å)

Figure 2.6 shows an exemplary KPFS experiment: The sample was

a (111) surface of a copper single crystal. Submonolayer coverage of bilayer NaCl islands was deposited. The charge neutral NaCl adlayer is expected to reduce the work function of the sample due to the push back of electrons that penetrate into the vacuum in front of the metal surface [44, 54, 55]. The tip was once positioned over a NaCl island and the Δf signal was recorded while the bias voltage was swept in the range of $\pm 1\,\mathrm{V}$ (blue curve). A reference spectrum was recorded in a void in the NaCl island (red curve). Second order polynomial fits provide the positions $V^\star$ at which the $\Delta f(V)$ spectra reach their maxima $\Delta f^\star$.

The difference in $V^\star$ values is about $0.4\,\mathrm{V}$. This is in contradiction to the reported difference of $1.0\,\mathrm{V}$ in $LCPD$ values for the same system [44]. At this point it is important to realize, that KPFS is sensitive to electrostatic interactions that are more long range than forces responsible for e.g. atomic contrast in AFM imaging. Due to this longer-range electrostatic interaction [56], the observed $V^\star$ values are not only due to the area of the sample directly underneath the tip apex but they are heavily affected by an area of few or even tens of nanometers in diameter [57]. This long range sensitivity of KPFS can be rationalized by the impact of local charges or dipoles in two ways:

On the one hand, the intrinsic surface dipole of the sample is altered by localized charges. Hence the electrostatic energy $E_{\mathrm{es},\,1}$ is given by the contribution of the global contact potential difference everywhere on the clean sample and the ones from all sample areas affected by additional surface charges [58] — generated by e.g. adsorbates:

$$E_{\mathrm{es},\,1} = \frac{1}{2} C_0 \left(V - CPD\right)^2 + \frac{1}{2} \sum_i C_i \left(V - LCPD_i\right)^2 \qquad (2.10)$$

Here, C_0 represents the capacitance between the tip and the sample without adsorbates. In this area there are no localized charges and the CPD at this position serves as reference for comparison with areas affected by local charges. C_i is the capacitance between the entire tip

and the charge affected sample area i. The associated $\Delta f_{\mathrm{es},1}$ signal reads

$$\Delta f_{\mathrm{es},1} \propto \frac{1}{2}\frac{\partial^2 C_0}{\partial z^2}\left(V - CPD\right)^2 + \frac{1}{2}\sum_i \frac{\partial^2 C_i}{\partial z^2}\left(V - LCPD_i\right)^2 . \quad (2.11)$$

The bias value $V_1^\star$ at maximum $\Delta f_{\mathrm{es},1}$

$$V_1^\star = \frac{\frac{\partial^2 C_0}{\partial z^2} CPD + \sum_i \frac{\partial^2 C_i}{\partial z^2} LCPD_i}{\frac{\partial^2 C_0}{\partial z^2} + \sum_i \frac{\partial^2 C_i}{\partial z^2}} \quad (2.12)$$

consists of contributions of all sample areas weighted with the second derivative of all tip-sample capacitances. Note that the local charges depend on the bias voltage in this model.

On the other hand, the effect of a charge localized at the sample surface can be modeled by its effect on the electrostatic energy only. In this case, the localized charge is independent of the bias voltage. This is especially applicable for charged adsorbates on insulator surfaces [59, 60]. In this case, the entire electrostatic energy of tip and sample $E_{\mathrm{es},2}$ is given by two components: First, the energy due to the global CPD and the applied bias voltage (see eqn. 2.8) has to be considered. Second, the energy of all individual localized charges q_i in the electric potential $\phi(\vec{r_i})$ at positions $\vec{r_i}$ of the charges. All together $E_{\mathrm{es},2}$ reads:

$$E_{\mathrm{es},2} = \frac{1}{2} C_0 \left(V - CPD\right)^2 + \sum_i q_i \phi(\vec{r_i}). \quad (2.13)$$

The electrostatic potential ϕ scales with the applied bias voltage V and can be written as

$$\phi(\vec{r_i}) = \left(V - CPD\right) \cdot \tilde{\phi}(\vec{r_i}). \quad (2.14)$$

Here, $\tilde{\phi}(\vec{r_i})$ captures the dimensionless normalized potential shape between tip and sample. The electrostatic energy $E_{\mathrm{es},\,2}$ and the corresponding frequency shift signal $\Delta f_{\mathrm{es},\,2}$ read:

$$E_{\mathrm{es},\,2} = \frac{1}{2} C_0 \left(V - CPD\right)^2 + \sum_i q_i \left(V - CPD\right) \tilde{\phi}(\vec{r_i}) \tag{2.15}$$

$$\Delta f_{\mathrm{es},\,2} \propto \frac{1}{2} \frac{\partial^2 C_0}{\partial z^2} \left(V - CPD\right)^2 + \sum_i q_i \left(V_{\mathrm{b}} - CPD\right) \frac{\partial \tilde{\phi}(\vec{r_i})}{\partial z^2} \tag{2.16}$$

The voltage $V_2^\star$ at which the $\Delta f_{\mathrm{es},\,2}$ signal reaches its maximum is given by:

$$V_2^\star = CPD - \frac{\sum\limits_i q_i \frac{\partial \tilde{\phi}(\vec{r_i})}{\partial z^2}}{\frac{\partial^2 C_0}{\partial z^2}} \tag{2.17}$$

Again, the contribution of the individual charges q_i is weighted, but this time with the vertical derivative of the electrostatic potential between tip and sample.

The result 2.17 agrees qualitatively with 2.12 in the sense that positive (negative) charges at the sample surface reduce (increase) the experimentally observed $V^\star$ value. For a complete description of the second case, one has to take the effect of image charges into account. The image charges located in the sample do, however, not play a role. In a simplistic approximation, their contribution cancels out when calculating the frequency shift from the tip-sample potential using eqn. 2.7 since the image charges are not tip-height dependent [60]. However, any image charge induced in the tip may play an important role. In addition, the model of non-interacting charges does not take bias voltage induced localized charges into account. Therefore, we will use the qualitative first interpretation of KPFS $V_1^\star$ signals for our experiments.

Figure 2.7 provides an exemplary illustration of the long range contrast in KPFS: Panel a shows a side view of the model tip: It consists

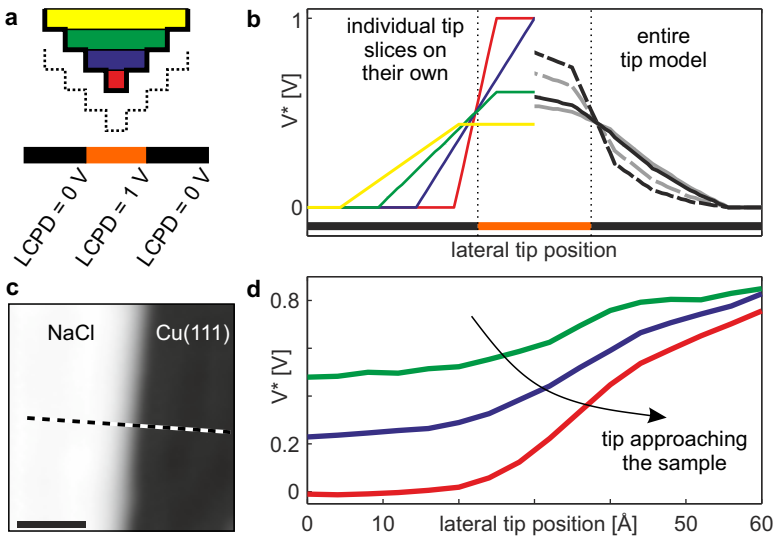

Figure 2.7: Comparing FM- and AM-KPFS for a basic plate capacitor model and experimentally FM-KPFS on a NaCl edge: **a** Schematics of a tip model consisting of metallic plates scanned across a sample, which has an exemplary $LCPD$ pattern. **b** Simulated V^* values for each slice of the tip on its own (thin colored lines in the left half) and for the entire tip model (right half) in the case of AM-KPFM (gray profiles) and FM-KPFM (black lines) . Solid and dashed black/gray profiles correspond to the entire tip model being far away from the sample or close to it. The thick line at the bottom of the graph indicates the $LCPD$ pattern. **c** STM topography image of bilayer NaCl island edge in copper surface with NaCl island on the left hand side and clean Cu(111) on the right hand side. Sets of KPFS spectra were recorded along the dashed line. (Scale bar 20 Å) **d** Experimental V^* signals for lines of KPFS spectra recorded in different constant heights across the NaCl edge. Data for the red curve was recorded with the smallest tip-sample spacing. For the blue and green curve the tip was retracted by 5 Å and 11 Å, respectively.

of a stack of only four parallel plate capacitors [56]. The sample is modeled to be flat and has zero $LCPD$ with respect to the tip except for one distinct area (depicted in orange) with a $LCPD$ of 1.0 V.

For simplicity, the contributions of the electric field from each part of the tip are assumed to be homogeneous without any contributions from the boundaries. This assumption is unrealistic in terms of a real experiment because the electric field lines do not run perpendicular to the sample surface within the entire volume between tip and sample. In addition, the work function of the tip is assumed to be homogeneous, which is not realistic since this assumption neglects the Smoluchowski effect [61]. However, the qualitative effects of the tip shape on the KPFS signal are apparent within this simple model. To simulate a KPFS experiment, this model tip is scanned across the artificial $LCPD$ structure. Thin colored lines in Fig 2.7b show simulated $V^\star$ values for each isolated slice of the tip on its own, i.e. without the other three slides being present in the simulation. Strikingly, only the red and the blue curves representing signals from the last two isolated tip slices show a correct $V^\star$ value for the central sample area. Yet, the blue curve reaches this value only at one single point indicating a pointlike $LCPD$ feature at the sample. For the third and fourth tip slice, the $V^\star$ values remain below the intended $LCPD$ value (see green and yellow curve). In this simple model this observation can be rationalized from an overlap argument: Since the isolated tip slice is larger than the size of the $LCPD$ patch on the sample only a fraction of the tip slice contributes the correct value. From this observations, one must conclude that sharp tips are essential to resolve $V^\star$ signals with highest lateral resolution [58].

To model the entire tip, the individual slices are combined and the $V^\star$ signal for the entire tip is plotted as solid black line in Fig. 2.7b for the case of frequency modulation KPFM (FM-KPFM). Since all slice areas directly facing the sample contribute to the signal, the maximum $V^\star$ value is about 0.6 V only. Please note that, this tip model consists of four slices only. A realistic tip is way larger and hence the influence of tip shaft will reduce the $V^\star$ value even more.

The solid gray line serves for comparison with amplitude modulation KPFM (AM-KPFM). In this case, the experiment is sensitive to

Method	sensitive to	signal proportional to
SCM [1]	current	C
Kelvin method	current	$\partial C/\partial z$
AM-KPFM	force	$\partial C/\partial z$
FM-KPFM	force gradient	$\partial^2 C/\partial z^2$

Table 2.1: Influence of tip-sample capacitance in different modes of Kelvin probe

forces that are of a more long range nature than the force gradients, FM-KPFM is sensitive to. Due to this increase of long range contributions, the maximum $V^\star$ value is reduced for AM-KPFM as compared to FM-KPFM [62–64]. This observation can be rationalized by the fact that electrostatic tip-sample forces scale with the first derivative of the entire tip-sample capacitance with respect to the tip height, whereas the Δf signal scales with the second derivative (see eqn. 2.9 and table 2.1). Similar to the arguments presented in section 2.2.2 the contribution of the last most tip component becomes more important when looking at derivatives of tip-sample interactions.

To understand the distance dependence of resolution and contrast in the simulation, the tip model was scanned a second time over the sample at a closer distance. Thereby, the relative weight of the last most tip slice is increased as compared to the rest of the tip. The result of this simulation is depicted as dashed lines in Fig. 2.7b. Both FM- and AM-KPFM resolution and contrast are enhanced [66, 67].

The effect of tip-sample spacing is also illustrated by experimental data depicted in Fig. 2.7c and d. The sample area consists of a NaCl bilayer island on Cu(111) and clean copper right next to the island. KPFS spectra where recorded along a line in different constant heights across the NaCl island edge (see panel c). The $V^\star$ values for three

[1] While scanning capacitance microscopy (SCM) utilizes an oscillating bias voltage to generate a capacitive current [65], the Kelvin method mechanically oscillates the probe electrode and is therefore sensitive to the capacitance gradient.

lines are depicted in panel d: The data set with smallest tip-sample spacing (red line) shows a $V^\star$ contrast of about 0.7 V, which is close to the reported value of 1.0 V [44]. When the tip is retracted by 5 Å and 11 Å, this contrast reduces to about 0.5 V and 0.3 V, respectively. Hence, the tip must be located as close as possible to the sample to get maximum contrast. However, when the tip is very close to the sample surface, problems may arise: First, due to the applied bias voltage, a huge tunneling current may flow, that can destroy the sample. In case of non-negligible sample resistivity, parasitic potential drops can heavily influence KPFS experiments [68, 69]. Second, for experiments with individual molecules it has been shown that the electron shell of the molecule might be penetrated when the tip is very close to the sample and hence unscreened atomic core charges are observed [14]. Finally, the large electric fields in the junction can affect the AFM signal via vertical relaxations of atoms on the sample and prohibit an interpretation of the Δf signal in terms of mere electrostatics (see chapter 8).

3 Experimental setup and methods

This chapter provides a brief introduction of the apparatus used for this thesis. The build-up and performance of the qPlus sensor are described. Details of tip functionalization — the final step for achieving atomic resolution of individual molecules — and the modes of data acquisition are provided.

3.1 LT-UHV combined STM/AFM apparatus

Experiments were performed using a homebuilt combined STM/AFM based on a qPlus sensor [7]. For the required cleanliness it is operated in ultra high vacuum ($p \approx 5 \cdot 10^{-11}$ mbar). For maximum stability and to prevent thermally activated diffusion of (molecular) adsorbates the scanner is cooled to ≈ 5 K. A photograph of the apparatus is given in Fig. 3.1: The vacuum chamber consists of three separable parts. The load-lock serves for quick sample and evaporator transfer from ambient. The preparation chamber is equipped with a sputter gun and salt evaporators. The scan head is mounted beneath a liquid helium bath cryostat to allow experiments to be performed at ≈ 5 K. Further details of the vacuum chamber and scanner design can be found elsewhere [71, 72].

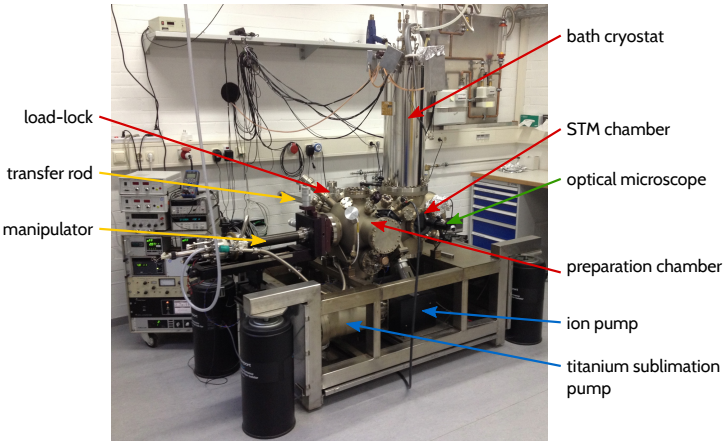

Figure 3.1: UHV-LT STM/AFM apparatus: The apparatus consists of three independent chambers (load-lock, preparation and STM chamber). Pumps are mounted beneath the preparation chamber. Samples and evaporators are inserted to the load-lock and transferred into the preparation chamber. Image kindly provided by N. Pavliček [70].

3.2 qPlus sensor

The key unit of the entire experimental apparatus is the force senor. It is based on the qPlus design [7]. A photograph of such a sensor is depicted in Fig. 3.2a. The evolution of the resonance frequency during build-up and in different environments will be described for a single exemplary sensor in the following:

The sensor is based on a commercially available quartz tuning fork oscillator. It is delivered in a metal housing, which we remove. The tuning fork is, then, glued onto a ceramic senor substrate. At this state the sensor is tested at ambient conditions [1] to ensure that no damage

[1] The sensor test stage was designed and build-up by Dominik Bauer in the framework of his Bachelor thesis: 'Aufbau einer Teststage zur Charakterisierung von qPlus-Sensoren für Rastersondenmikroskopie', Universität Regensburg, 2011

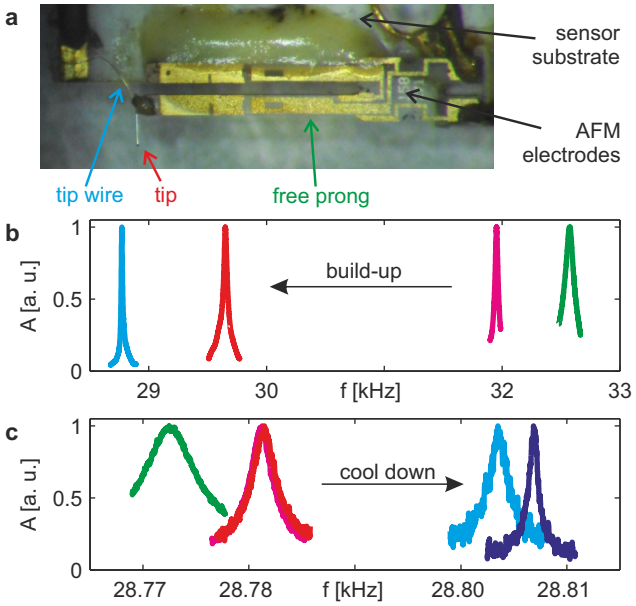

Figure 3.2: Build-up of a qPlus sensor: **a** Photograph of a qPlus sensor: The upper prong is glued to the sensor substrate that is mounted to the scanner. The tip — 20 μm thick PtIr wire — is attached to the free prong. An additional 10 μm thick gold wire electrically contacts the tip and thereby enables simultaneous STM experiments. **b** Resonance spectra of a qPlus sensor during build-up: The first spectrum was recorded after gluing the tuning fork onto the sensor substrate (green spectrum). The pink and red spectrum represent the resonance peak after attaching glue for tip insulation and the tip itself, respectively. The light blue curve was recorded after attaching the gold wire to the tip. **c** Resonance spectra of qPlus sensor inside the microscope: The green curve was recorded at ambient conditions before pumping the chamber. Pink and red were recorded before and after bake-out at room temperature in vacuum and are almost identical. Light and dark blue show the resonance at a temperature of 77 K and 5 K, respectively.

has occurred. The resonance frequency has slightly changed from its value as delivered (2^{15} Hz = 32.768 kHz) to 32.572 kHz (green curve in Fig. 3.2b). The next step was to attach some non-conductive glue to the end of the free prong to electrically decouple the tip from the AFM electrodes. Due to the additional mass of this glue, the resonance shifted by about 0.6 kHz (pink peak). Then, the tip is attached. It is made of a sharpened piece of 20 μm thick PtIr wire. This piece of metal is relatively heavy and reduces the resonance frequency by 2.3 kHz (red spectrum). Finally, a 10 μm thick gold wire is connected to the tip to allow simultaneous STM and AFM experiments (blue curve in Fig. 3.2b).

At that stage, the qPlus sensor was ready and got mounted to the STM/AFM scan head in the LT-UHV apparatus and the oscillation signal was recorded by the electronics of the STM/AFM. When the chamber was pumped from ambient pressure (see green curve in Fig. 3.2c) to high vacuum the resonance frequency increased by about 15 Hz and the quality factor Q [25] enhanced by roughly a factor of two to 8000 (pink spectrum). When cooling the scanner to 77 K and 5 K the resonance frequency was increased slightly and Q reached a value of about 18000 (light and dark blue curves).

To interpret the observed Δf signal in terms of a force acting between tip and sample the stiffness of the AFM cantilever is required 2.7. The stiffness of the cantilever is unknown in the first place and — on top — we do not know to which extend the cooling to 5 K changes its stiffness.

For a qPlus sensor, the mass of the oscillating cantilever beam can not be neglected for the calculation of the resonance frequency. To calculate the mass of the cantilever beam from its resonance frequency, the deflection profile along the cantilever is required. For a beam of constant cross section and mass density the deflection profile along the beam is given by [16]

$$h(x) \propto x^3 - 3Lx^2. \tag{3.1}$$

Here, x points along the beam, h is the deflection of the beam and L denotes the entire length of the cantilever.

During the oscillation of the cantilever, its energy is transferred between the elastic energy of the deflection and kinetic energy of the beam's motion [73]. The kinetic energy is maximal when the beam is passing its rest position. At this point, the elastic energy is zero. The total kinetic energy of the entire beam can be calculated by integrating it along the beam:

$$E_{\text{kin}} = \frac{1}{2} \int_0^L \frac{m_{\text{beam}}}{L} \left(v(x)\right)^2 dx \tag{3.2}$$

m_{beam} denotes the mass of the entire beam. Assuming a harmonic oscillation, the maximum velocity of each beam segment is given by its deflection:

$$v(x) = ch(x) \tag{3.3}$$

The constant c is derived from the boundary condition at the free end of the beam at position L from eqn. 3.1:

$$\begin{aligned} v(L) = ch(L) &= c\left(-2L^3\right) \\ \rightarrow c &= -\frac{v(L)}{2L^3} \end{aligned} \tag{3.4}$$

Combining equations 3.2 and 3.4 for the deflection profile 3.1, we get:

$$\begin{aligned} E_{\text{kin}} &= \frac{1}{2} \int_0^L \frac{m_{\text{beam}}}{L} \left(-\frac{v(L)}{2L^3}\left\{x^3 - 3Lx^2\right\}\right)^2 dx \\ &= \frac{1}{2} \frac{m_{\text{beam}} \left(v(L)\right)^2}{4L^7} \int_0^L \left\{x^3 - 3Lx^2\right\}^2 dx \\ &= \frac{1}{2} \underbrace{\frac{33}{140} m_{\text{beam}}}_{m_{\text{eff}}} \left(v(L)\right)^2 \end{aligned} \tag{3.5}$$

Hence, the motion at the free end is connected via the effective mass m_{eff} to the energy of the entire cantilever. For a harmonic oscillator of resonance frequency f_0, stiffness k and mass m are connected by:

$$f_0 = \frac{1}{2\pi}\sqrt{\frac{k}{m}}$$
$$\rightarrow k = 4\pi^2 f_0^2 m \tag{3.6}$$

For the calculation of the stiffness of the cantilever we have to take the effective mass m_{eff} instead of the entire mass: $m_{\text{eff}} = 33/140\, m_{\text{beam}} \cong 0.24\, m_{\text{beam}}$. The mass of 177 μg for the cantilever beam used in this experiment is defined by its dimensions 2.400 mm × 0.214 mm × 0.130 mm [74] and the mass density of quartz of 2.65 g/cm^3 [75]. Hence, we have to take m_{eff} =42 μg to calculate the stiffness of the cantilever from equation 3.6. The result of 1768 N/m is in excellent agreement with the value provided by the manufacturer of 1800 N/m.

Apart from the cantilever stiffness k and the effective mechanical mass m_{eff}, intrinsic damping can in general affect the resonance frequency of the oscillator [76]. However, the mechanical quality factors Q measured at all states of the sensor build-up and cooling down were never below 1000. Hence the damping-induced shift of the resonance frequency is always well below 1 Hz and can be neglected.

The decrease in resonance frequency after each step of the sensor build-up is explained by the masses added to the end of the free prong (see Fig. 3.2b). The gold wire for the tunneling current could affect the cantilever stiffness. However, the stiffness of the 10 μm thick gold wire is expected to be way smaller than that of the quartz tuning fork. Additionally, the gold wire is connected to the free prong and the sensor substrate in a way a rather large loop is formed to create a soft link.

During the cool down the mass of the cantilever is constant and the (slight) increase in resonance frequency can be attributed to a negligible increase of the mechanical stiffness of about 0.4 %.

3.3 Sample preparation

All experiments presented throughout this thesis were performed on a (111) surface of a copper single crystal surface. It was cleaned by several sputtering and annealing cycles in the preparation chamber. NaCl was evaporated thermally, while the sample temperature was kept between 280 K and 315 K, so that defect-free, (100)-terminated NaCl islands were formed [4, 44, 77, 78]. After NaCl deposition, the sample was transferred into the scanner.

A small amount of CO was dosed onto the surface for tip functionalization during AFM experiments [6, 13]. Individual molecules were sublimed onto the sample being located in the microscope at a temperature of $T < 10\,K$. For experiments presented in chapters 7 and 9 individual gold atoms where co-deposited with the sample also located in the microscope.

Bias voltages refer to the sample with respect to the tip.

3.4 Modes of data acquisition

The two signal channels for experiments in this thesis are the tunneling current I for the STM and the frequency shift signal Δf for the AFM. This section will introduce different modes of data acquisition used for different purposes:

Imaging In conventional SPM experiments there are two imaging modes: First, an active z-feedback loop keeps the current between tip and sample constant (constant-current mode). The recorded image shows the topography along which the tip was scanned across the surface. Second, the z-feedback is switched off (constant-height mode). Here, the tunneling current and the frequency shift are recorded with

the tip scanned across the surface in a predefined plane. Thereby, both channels can be recorded independently and no changes in tip-sample spacing due to an active z-feedback can affect the recorded data. However, for qualitative symmetry analysis or determination of adsorption sites the Δf signal recorded along the constant-current STM profile may at times be very useful [79, 80].

When recording Δf images at small tip-sample distances in constant-height mode to achieve highest lateral resolution, the bias voltage is commonly set to zero. Thereby, the effect of the tunneling current on the experiment is minimized: On the one hand, a huge current may move the molecule on the sample by inelastic excitations [81] or even destroy the molecule. On the other hand, the finite impedance of the sample can cause a potential drop within the sample and can heavily affect the observed AFM contrast [68, 69].

Spectroscopy The required information is often inaccessible from imaging the sample surface only. Therefore, different spectroscopy modes are available:

To deduce the distance dependence of the tip-sample interaction the Δf signal is recorded while the tip height is ramped — called $\Delta f(z)$ spectroscopy. We identify the geometric structure of a non-planar molecule with $\Delta f(z)$ spectroscopy performed on a dense grid (see next paragraph and chapter 5).

Scanning tunneling spectroscopy (STS) is applied to probe the electronic structure in terms of the density of states of the sample (see section 2.1.2). In chapter 7 we use this technique not only to deduce the energetic position of molecular electronic states but to also perform dI/dV imaging: The tip is scanned in constant-height mode across the sample while the dI/dV signal is recorded. These dI/dV images provide the spatial distribution of individual molecular orbitals.

KPFS was utilized to investigate electrostatic forces: Kelvin parabolas (see Fig. 2.6) were recorded and the position of the maximum Δf value provides qualitative information of the electrostatic potential/charge density of the sample surface. To achieve optimal contrast and resolution, these spectra should be recorded with the tip being positioned as close as possible to the sample (see section 2.3). For very small tip-sample spacings KPFS turned out to be insufficient and we had to introduce a new spectroscopy scheme. Figure 3.3b illustrates this new mode schematically: While in conventional KPFS the bias voltage is swept at constant tip height (from time I to II and III to IV) we additionally record the Δf signal during tip-height modulation for different bias voltages (II to III and IV to V).

In addition to tunneling current and Δf, the oscillation amplitude and the excitation signal were recorded to exclude artifacts due to variations in the amplitude.

Spectra on grid To get insight into the local variation of spectroscopy derived information we performed spectroscopy on dense grids in constant-height mode. Figure 3.3a sketches the automated acquisition procedure. The data acquisition time to record one set of spectra on a grid ranges between 10 and 45 hours. To compensate for drift and creep, after each line of spectra, the tip was positioned on clean copper (or NaCl/Cu(111)) next to the molecule and the z-feedback was switched on for a few seconds to readjust the tip-sample distance. Additionally, an image was recorded to determine the lateral drift. A cross-correlation of these images yielded the lateral drift that is corrected for by one of the two ways as follows: Either this error is corrected for by shifting the pixels in the resulting maps after recording the entire data set or by adjusting the position of the subsequent line of spectra while recording the data set. The latter provides the advantage of the lateral data grid being rectangular.

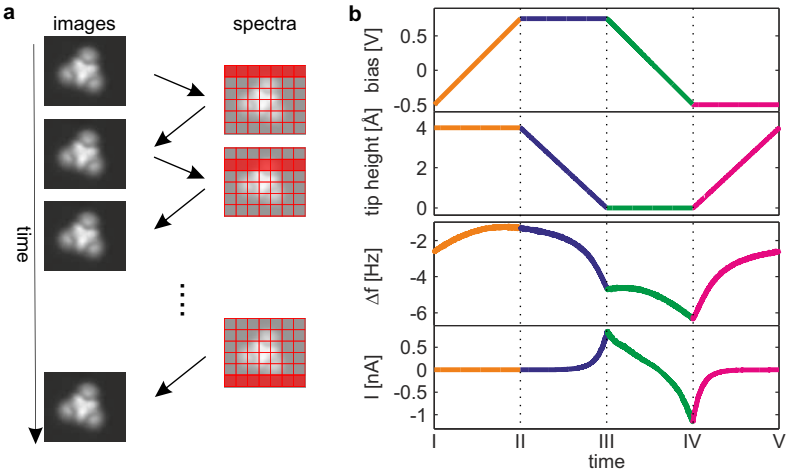

Figure 3.3: Data acquisition scheme for grid data: **a** To record spectra on a dense grid over molecules, images where recorded after each line of spectra for cross correlation and site adjustment of the individual grid points. **b** Spectra of combined tip height ramps and bias sweeps were acquired. The Δf signal and the tunneling current were recorded simultaneously.

3.5 Tip functionalization

To achieve high lateral resolution in SPM the tip has to be sharpened to expose one or very view single atoms at the very end. An additional adsorbate at the tip apex may increase the resolution. In the past, xenon atoms [82] and carbon monoxide (CO) molecules [83–86] were transferred to the tip from the sample in STM experiments. In the case of CO, the symmetry of the tip orbital contributing to the tunneling current is different as compared to a metallic tip [16, 85, 86].

In 2009, L. Gross and coworkers introduced CO tip functionalization for investigating individual molecules with AFM [6]. Due to the increase in stability and the boost in lateral resolution, it became possible to image the molecular structure of individual adsorbates down to

single atoms in real space. Since then, this technique is widely applied for the imaging of molecules by means of AFM (for overviews see [87, 88] and more recent works [47, 89–98]). Beside CO, other molecules and atoms e.g. bromine, chlorine, krypton, oxygen [99] and nitric oxide (NO) [100] were transferred to the tip for various experiments.

In addition to imaging, tip functionalization was also applied for spectroscopy experiments like KPFS using CO [13, 14], chlorine or xenon [59, 101].

CO is most commonly used for tip functionalization mainly due to the unpretentious experimental procedure in combination with the large increase in resolution. A small amount of CO is dosed onto the sample surface and individual CO molecules can be picked up to the tip apex by approaching the tip towards the sample. Although the pickup of a CO from a clean copper surface has been shown to work [6, 83], it is easier when the CO is adsorbed on NaCl islands on-top of a metallic substrate.

To resolve the atomic structure of molecular adsorbates the tip has to be very close to the sample surface. In this distance regime, Pauli repulsion is responsible for the short-range image contrast [6, 102, 103]. Apart from Pauli repulsion between the apex atom of the tip and the sample, also lateral relaxations of the entire CO molecule at the tip are essential to explain the observed contrast in detail [104–109]. The CO at the tip is very stable in the sense of not coming off the tip apex but it is very flexible in terms of lateral stiffness. Any lateral modulation of the potential at the sample causes a deflection of the CO molecule at the tip. This bending effect can even cause misleading Δf contrast. Lines of bright contrast — typically observed at positions of covalent intramolecular bonds — may appear at locations without any bond [80, 107, 110–112]. Due to the little lateral stiffness of the CO molecule at the tip, lateral electrostatic force contributions need to be considered for a fully quantitative interpretation of Δf contrast [113, 114]. For qualitative structure analysis of a planar organic molecule

AFM images with CO functionalized tips without further demanding simulations are sufficient.

For high resolution FM-AFM imaging on individual molecules, tip functionalization is essential. In addition, the oscillation amplitude of the cantilever needs to be properly adjusted. For ultimate resolution sub-Ångstrom oscillation amplitudes are required [115]. Unless otherwise specified, the oscillation amplitude for data presented in this thesis is 0.5 Å.

3.6 Tip height conventions

An essential parameter in SPM experiments is the tip-sample spacing (see Fig. 4.2). In most cases an absolute value is not required. It is in general sufficient to compare relative changes in tip height. The reference used in most cases throughout this thesis is the setpoint of the STM. For data acquisition in constant-height mode the tip is either retracted (positive z-offset) or approached towards the sample (negative z-offset) from the height at a given STM setpoint. For identical STM setpoints at the same lateral position, the changes in z-offset provide the relative changes in tip height.

If an absolute tip-sample spacing is required, it can be roughly extracted from extrapolation of $I(z)$ data to the point of contact where the resistance of the tip-sample junction corresponds to one conductance quantum [16]. However, this method is only applicable for metallic tips and metal samples. For e.g. CO functionalized tips the tunneling current deviates from the one observed for a metallic tip and cannot directly be related to the size of the CO molecule (see Fig. 4.1).

For data analysis in chapter 9 we require the absolute tip-sample spacing for CO functionalized tips. For details on how the tip height was estimated in this case, see section 8.2.

4 Preliminary experiments on tip functionalization

Most of the data presented throughout this theses was recorded with functionalized tips. This chapter will present preliminary results to provide some insight into the experimental procedure of tip functionalization. An exemplary data set demonstrates the contrast evolution in AFM imaging of individual molecules. Spectroscopy data recorded on grids illustrate the effect of a tip change on KPFS results.

4.1 Characterization of CO functionalized tip

Figures 4.1a—f illustrate an exemplary image sequence for the preparation of a CO functionalized tip. Prior to the pick-up, an area with two CO molecules on-top of bilayer NaCl/Cu(111) is scanned with a sharp metallic tip in constant-current mode (see panel b). Counterintuitively, the CO molecules adsorbed on-top of the NaCl layer appear as depressions in the STM image. In the simultaneously recorded Δf image, the CO molecules appear as uniform attractive disks (panel c). After picking up the right CO molecule to the tip, the same sample area is scanned with the CO tip. Panel e shows the STM topography channel that indicates an increase in the lateral extent of the remaining CO along with a reduced apparent depth. The simultaneously recorded frequency shift signal — depicted in panel f — shows a drastic change in the AFM contrast upon CO pick-up: The background is more attractive, the lateral size of the feature is much larger and

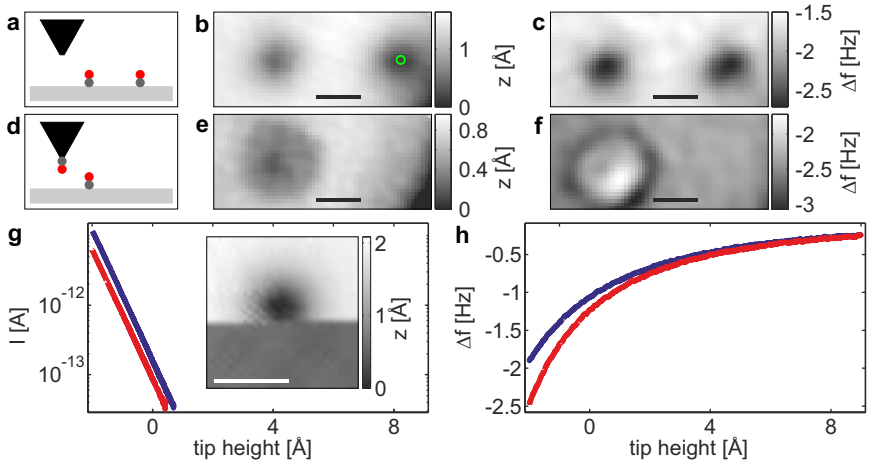

Figure 4.1: Functionalizing the tip by pick-up of a CO molecule: **a** Schematic side view of metal tip scanning across two CO molecules on the surface. **b** Constant-current STM image of two CO molecules adsorbed on bilayer NaCl/Cu(111) recorded with a metal tip. CO molecules appear as depressions. The green marker indicates the position of the tip approach for the CO pick-up. **c** Δf signal recorded simultaneously with STM image shown in panel a. **d** Schematic side view of CO tip scanning across a CO molecule on the surface. **e** Constant-current STM image of the same area after picking up the CO molecule on the right hand side. **f** Δf signal recorded simultaneously with STM image shown in panel e. Data for panels b, c, e and f was recorded with a constant current of 1 pA at 0.1 V bias. **g** $I(z)$ spectra recorded on clean copper with a metal tip (blue) and a CO functionalized tip (red). **h** $\Delta f(z)$ curves recorded simultaneously with data depicted in g. Spectra were recorded at a bias voltage of 0.015 V. Zero at the tip-height axis corresponds to a STM setpoint of 1 pA at 0.1 V with a metal tip on copper. All the spectroscopy shown in panels g and h including the CO pick up in between was performed without z-feedback. The inset in panel **g** shows an STM topography image recorded at a constant current of 2 pA and a bias voltage of 0.025 V. The CO jumped from the sample (bilayer NaCl/Cu(111)) to the tip during scanning (slow scan direction: top to bottom). (Scale bars 5 Å)

the center of the CO appears repulsive surrounded by an attractive ring. This effects may be explained by the fact that the CO at the tip reduces its conductance as compared to the metallic tip. Hence, the active z-feedback brings the tip closer to the surface after the pick-up. The inset in Fig. 4.1g shows an STM topography image where the CO jumped to the tip while scanning. The apparent height of the lower part of the image recorded with the CO tip appears reduced with respect to the upper area scanned with the metal tip.

The reduction in conductance is also observed in tunneling current spectroscopy. Spectra in Fig. 4.1g show $I(z)$ curves on copper recorded with a metallic tip (blue) and with the same tip after picking up a CO molecule (red). While recording this data including the tip functionalization in between, there was no z-feedback. Therefore, the difference in the $I(z)$ spectra is solely due to attaching the CO to the tip. Apparently the CO reduces the tunneling current even though it geometrically elongates the tip. Fig. 4.1h presents simultaneously recorded Δf data: The CO at the tip increases the attractive interaction between tip and sample. This is in line with a decrease in geometric tip-sample distance upon tip functionalization.

4.2 Contrast evolution on molecules with CO tip

Beside tip functionalization and appropriate oscillation amplitude the tip height is crucial to achieve atomic resolution on single molecules. Figure 4.2 shows the contrast evolution as a function of tip-sample spacing. Panel a shows models of the two organo-metallic molecules as observed on a Cu(111) surface. A constant-height tunneling current image recorded with a CO tip is depicted in panel b. Due to the sensitivity of STM to electronic states close to the Fermi level [16, 22] the lateral resolution is limited. In contrast, AFM is sensitive to all occupied electronic states [103]. Figs. 4.2c—f illustrate the contrast evolution for decreasing tip-sample spacing. At large distances

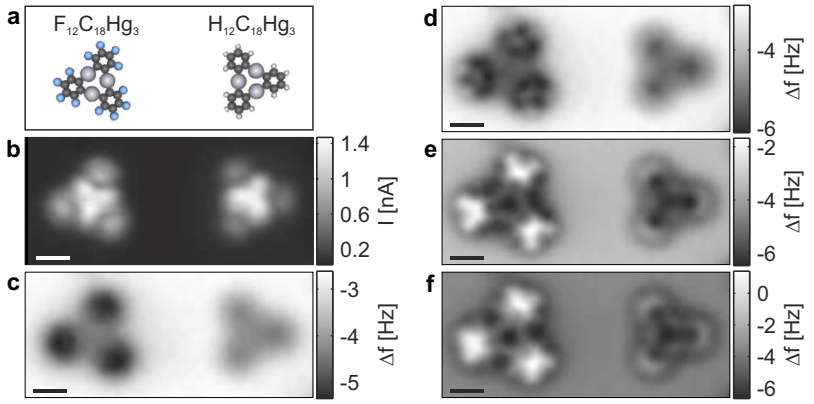

Figure 4.2: AFM contrast evolution on individual molecules with CO functionalized tip: **a** Ball models of molecules oriented like in the experiment. **b** Constant-height current image recorded at 0.2 V bias with the tip being retracted by 1.0 Å from an STM setpoint of 0.5 nA and 0.1 V. **c**—**f** Set of constant-height Δf images of the same sample area recorded with the tip being retracted by 2.0 Å, 1.6 Å, 1.2 Å and 1.0 Å from the STM setpoint of 0.5 nA and 0.1 V. (All scale bars 5 Å)

(panel c), the molecules appear as attractive areas with little internal corrugation. Long-range attractive interactions like van-der-Waals forces and electrostatics are responsible for the diffuse dark attractive contrast in this distance regime [6]. When the tip is approached toward the sample, the Δf signal starts to vary within each molecule. Bright, less attractive features appear first at molecular positions that protrude furthest from the sample surface (see outermost atoms of left molecule in panel d). Approach of the tip even further (panel e) resolves the structure of both molecules entirely. At the point of closest approach, the molecular structure starts to appear distorted (see outermost region of left molecule in panel f). The repulsive features in AFM images (bright contrast) in close tip-sample distance are due to Pauli repulsion [6, 102, 103]. When the front-most tip atom is very close to the molecule at the sample the tip-sample interaction is domi-

nated by repulsion between the entire electron density of the molecule at the position of the tip and the tip itself. The integrated electron density of the molecule corresponds to its geometric structure [103].

4.3 Tip-change induced artifacts in KPFS results

For imaging, that relies on short range interactions only, the CO tip can be characterized pretty reliably due to the drastic contrast changes when going from a metallic tip to a CO tip (see Fig. 4.1). However, more than the last one or two atoms are not accessible for tip characterization with single atom precision. This is of particular importance when long-range electrostatic interactions become dominant for the observed signals — which is the case in KPFS experiments [57].

Figure 4.3 demonstrates how a tip change, that is very faintly observable in imaging, can heavily affect KPFS results. Panel a depicts a $V^\star$ map of the molecules introduced in Fig. 4.2. The observed contrast is symmetric around each center of the two molecules. This allows the conclusion that the tip is fairly symmetric as illustrated in panel b. After finishing the data acquisition for the $V^\star$ map, an additional adsorbate appeared right next to the right molecule (see panels c and d). This adsorbate might be a noble gas atom. It was removed from the molecule by voltage pulses. After the removal, this adsorbate was not observed nearby the molecules anymore. Images recorded with the settings being the same as that of panels c and d are shown in panels e and f to exclude tip changes. Apart from the left molecule being rotated, the STM topography images show identical contrast. Even though the absolute Δf values have changed slightly, the contrast in the simultaneously recorded Δf images is almost identical. However, the subsequently recorded $V^\star$ map of the same sample area has lost its symmetry entirely (see panel g). The centers of the two molecules appear shifted and there is no resemblance of any symmetry around the centers of the molecules. Since the short range interaction did

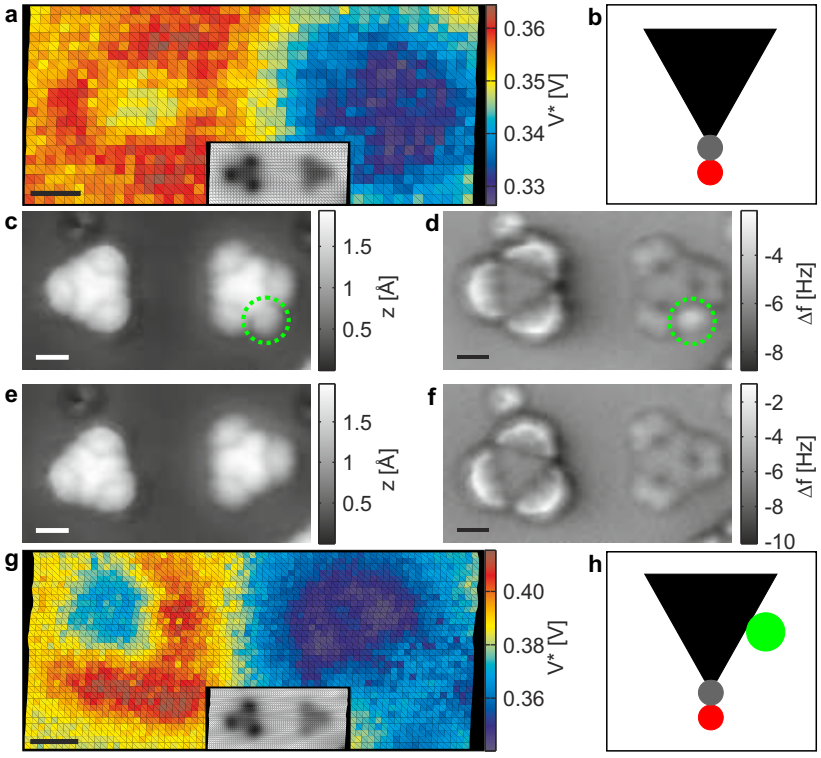

Figure 4.3: Effect of tip change on KPFS results: **a** $V^{\star}$-map of two molecules introduced in Fig. 4.2. The inset shows the map of $\Delta f^{\star}$ values of this grid data set. **b** Schematic side view onto CO functionalized tip model. **c** Constant-current STM topography image of the same two molecules after the appearance of an adatom right next to the right molecule (highlighted by the green dashed ring). **d** Frequency shift signal recorded simultaneously with the topography image in panel c. **e** and **f** Topography and Δf image after removing the adatom. **g** $V^{\star}$ map of the same area as the one shown in panel a after adatom removal. This map was recorded at a slightly reduced tip height. The inset shows again the map of $\Delta f^{\star}$ values. **h** Side view of an associated CO functionalized tip model with an additional atom at the tip shaft. ($V^{\star}$-maps were recorded in constant height. Data for panels c—f was recorded with at constant current of 0.5 nA at a bias voltage of 0.1 V. All scale bars 5 Å)

not change as shown by imaging before and after adsorbate removal (panels c—f and insets in panels a and g) something at the tip shaft must have changed. Most likely the adsorbate was transferred from the sample to the tip shaft as depicted schematically in panel h. This shows that care must be taken when preparing and characterizing a tip for KPFS experiments especially for recording individual spectra at single positions on the sample only.

5 Characterization of a surface reaction by means of AFM

Most of the work presented in this chapter has been published in the Journal of the American Chemical Society[1]*. Parts of the text are identical to the publication.*

AFM with functionalized tips allows achieving atomic resolution of individual adsorbates on a surface (see reference [6] and section 4.2). In combination with on-surface chemical reactions the high resolution of AFM offers the prospect of a detailed characterization of chemical reactions.

5.1 AFM in on-surface chemistry

Inspired by the unprecedented resolution of AFM with CO tips [6] this technique has been applied to identify the structure of an unknown molecule [79], to resolve the structure of reaction products in single molecule chemistry [9, 94] as well as in thermally induced on-surface chemical reactions [10, 89]. To avoid additional complexity in these demanding experiments, mostly planar molecules were studied, so that the structure determination could be achieved in the basic imaging mode, in which the tip is scanned in constant height over the sample.

[1] F. Albrecht, N. Pavliček, C. Herranz-Lancho, M. Ruben, and J. Repp. 'Characterization of a Surface Reaction by Means of Atomic Force Microscopy'. In: *J. Am. Chem. Soc.* 137 (2015), 7424.

For select cases of non-planar structures, the molecule was still flat enough to resolve its geometry [14, 80, 110, 116]. To quantify slight deviations from a flat configuration, as e.g. an overall small tilt of the molecular plane with respect to the surface it is adsorbed on, FM-AFM spectroscopy was employed more recently [117].

Most chemical reactions, however, involve three-dimensional (3D) molecular structures. In addition, the reaction pathway is critical for the reaction product. Although many catalytically activated reactions involve the presence of surfaces, on-surface chemistry and its reaction pathways are still poorly understood. In particular, the presence of a surface will strongly affect the possible reaction pathways, at least by restricting the molecular geometry.

5.2 Methods

Individual diphenanthro[9,10-b:9',10'-d]thiophene (DPAT) molecules were sublimed onto a Cu(111) sample being located in the microscope at a temperature of T $\cong$ 5 K. All AFM data was obtained with a CO-terminated tip. Density functional theory (DFT) calculations[2] of the free monomers were performed to obtain the molecular geometry. To confirm the structural assignment from AFM, matrix-assisted laser desorption and ionization – time of flight (MALDI-TOF) based mass spectrometry, nuclear magnetic resonance (NMR) spectroscopy, and elemental analysis were performed [118].

[2]CPMD V3.15 Copyright IBM Corp 1990-2011. Copyright MPI für Festkörperforschung Stuttgart 1997-2001

5.3 Structure identification of the reactant

DPAT molecules were synthesized from a solid-state reaction under CO_2 atmosphere between phenanthrene and elemental sulfur [118, 119] by our collaboration partners in the Karlsruhe Institute of Technology. The molecule in the gas phase is non-planar because of steric hindrance. The two phenanthrene moieties are bent out-of-plane at the side opposing the sulfur atom, thus giving rise to a helical shape of the molecule. Its structure as calculated from DFT is displayed in Fig. 5.1a. Provided that DPAT remains intact, adsorption onto the Cu(111) surface will break the symmetry between the two phenanthrene moieties since only one of them can directly face the surface. Interestingly, this asymmetry is not apparent in the topography of a constant-current STM image, as depicted in Fig. 5.1b. However, the simultaneously recorded frequency shift channel (Fig. 5.1c) shows a clear asymmetry between the two phenanthrene moieties[3]. Figures 5.1d—g show several constant-height AFM images of the molecule at decreasing tip-sample distances. Note that in Fig. 5.1g the two CO molecules adsorbed next to the DPAT molecule stabilized the molecule against lateral displacement. Similar imaging attempts without CO next to DPAT resulted in lateral displacement of the molecule in such a way that it could not be stably imaged (Fig. 5.1f). At the upper left part of Fig. 5.1d, the repulsive interaction sets in at considerably larger tip height than over the rest of the molecule. Hence, this part of the molecule has to protrude towards the tip. Otherwise, the image acquired at closest tip-sample distance carries most of the information: four of the benzene rings are readily identified and seem to be oriented roughly parallel to the sample surface — all at a comparable adsorption height. This can be deduced from the intramolecular contrast being relatively homogeneous over these four benzene rings.

[3] In constant-current imaging mode, the Δf-signal is influenced by the z-feedback. However, the Δf-image shows much more asymmetry between the two phenanthrene units than the topography.

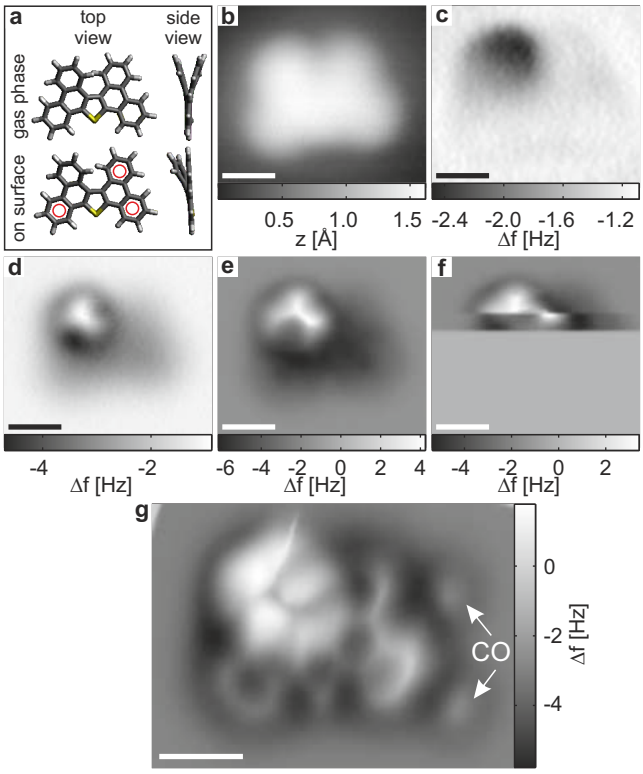

Figure 5.1: Characterization of DPAT molecules by means of scanning probe microscopy in conventional modes of operation: **a** Stick models of the molecule's geometry as calculated for the free molecule after full relaxation (top) and with three benzene rings (marked in red) forced to one plane (bottom) to mimic the on-surface geometry, respectively. Carbon, hydrogen and sulfur atoms are represented in black, white, and yellow, respectively. **b** and **c** Simultaneously recorded topography (b) and frequency shift (c) acquired with active current feedback (constant-current mode, $I = 2\,\mathrm{pA}$, $V = 0.05\,\mathrm{V}$) **d—f** Set of Δf-images of a single DPAT molecule on clean copper. ($\Delta z = -0.3\,\mathrm{Å}$, $-0.5\,\mathrm{Å}$, and $-0.7\,\mathrm{Å}$ with respect to the STM setpoint of $I = 2\,\mathrm{pA}$ and $V = 0.1\,\mathrm{V}$) **g** Δf-image of a DPAT molecule pinned to two CO molecules. ($\Delta z = -2.0\,\mathrm{Å}$ from the STM setpoint of $I = 1\,\mathrm{pA}$ at $V = 0.1\,\mathrm{V}$) The non-planar structure of DPAT is apparent in all AFM images. (Scale bars 5 Å.)

This suggests that the phenanthrene moiety facing the surface (to the right in Fig. 5.1g) is flattened out upon adsorption, whereas the other one bends even further due to steric hindrance. There is one atom exhibiting a bond angle slightly smaller than 90°, whereas all other atoms show approximately the 120° bond angles expected for sp^2-hybridized carbon atoms. This suggests that the atom with the smaller bond angle is sulfur. Whereas one can guess from the image that the sulfur atom is part of a five-membered ring structure, the part of the molecule that sticks out of the surface plane cannot be identified, and it only leads to the strongly distorted part of the AFM image.

To also resolve the structure for this part of the molecule, we acquired a three-dimensional (3D) data set of frequency shift Δf as a function of all coordinates x, y and z, by recording Δf versus distance z on a dense grid in the surface plane x, y (for details of grid data acquisition see section 3.4). To avoid too strong tip-sample interaction at close distances z, each of the $\Delta f(z)$ spectra was aborted upon reaching a predefined Δf value as proposed and described by F. Mohn et al. [120]. With this data set, we can extract and display Δf values for any arbitrary plane within the 3D data set. The analysis of such 3D imaging is shown in Fig. 5.2. By a variation of the orientation of such planes and looking at the resulting images, one can unambiguously resolve the remaining structure of the molecule. Furthermore, as the orientations of the imaging planes are set, this technique allows us to extract the out-of-plane distortion angles of the molecule within a few degrees uncertainty. Based on this analysis, we can identify the molecular structure itself as well as its 3D geometry after adsorption, despite the out-of-plane rotation of one of the benzene rings being as large as $\simeq 23°$. This possibility to resolve the 3D geometry of molecules is not at all self-evident, because at some even larger tilt angle one may expect that the CO bending at the tip apex [102] prevents a structural analysis.

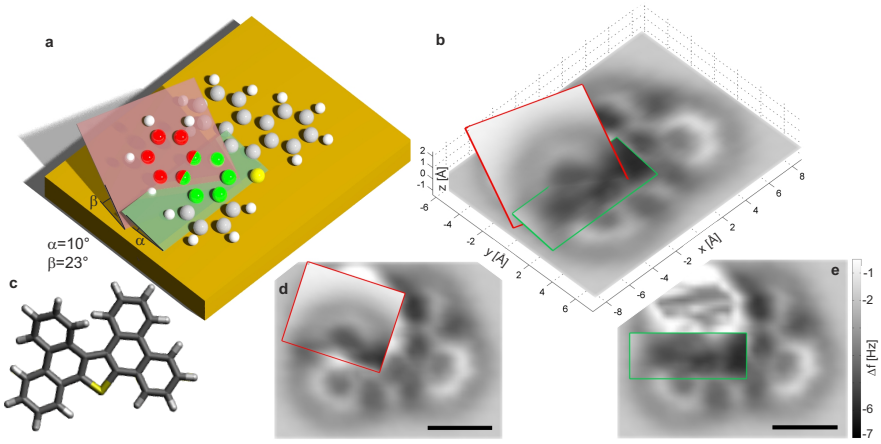

Figure 5.2: Molecular structure identification from a 3D data set: To resolve the molecular structure from Δf imaging, the 3D data set is displayed along three different planar cross sections. While one of them is parallel to the surface, the other two are aligned with respect to the two carbon rings that are tilted with respect to the surface (green and red). **a** 3D representation of molecular structure including the cross-sections, along which the experimental data is displayed in **b**. **c** Top view of the structure model for reference. **d** and **e** Top views of 3D data with only one of the tilted cross sections in each panel. (Scale bars 5 Å.)

To verify our structural assignment, we performed MALDI-TOF and NMR [118] measurements of the molecules. Both mass and NMR spectra fully support our structural analysis. Note that, without expecting the reaction product that was identified from AFM, the NMR spectrum is not easily converted into a structural model. To further analyze the geometry of the molecule, we mimicked the flattening of one phenanthrene moiety upon adsorption in the geometry calculations by forcing three of the carbon rings to be planar, and by letting the rest of the molecule relax. The resulting geometry fits very well to the geometry deduced from AFM data, as shown in Fig. 5.2, including the out-of-surface tilt angles of $\simeq 10°$ and $\simeq 23°$, respectively.

5.4 Molecular species after thermally activated on-surface reaction

The molecular structure and the strong out-of-plane distortion suggest that the molecule can be planarized by annealing. In analogy to other on-surface reactions [121, 122] one might expect a ring closure by a C–C bond formation at the position of steric hindrance resulting in a C_{2v}-symmetric molecule [119] (having C_S-symmetry when adsorbed).

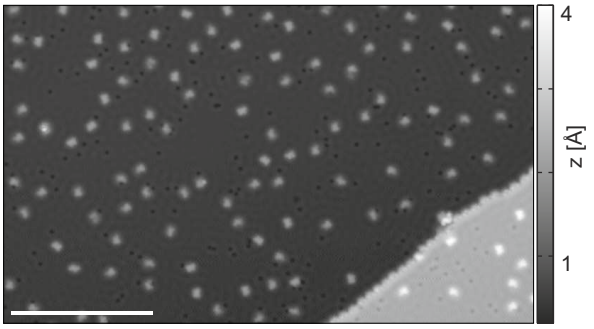

Figure 5.3: Overview image of copper terraces after annealing: The STM topography image shows individual molecules on copper terraces. The copper step edge at the lower right is decorated with molecules. Point-shaped depressions are due to CO. The image was recorded with a constant current of 1 pA at 0.1 V bias voltage. (Scale bar 200 Å.)

To activate such an on-surface-reaction, we annealed the sample to 200 °C. Figure 5.3 shows an STM overview image of the sample after annealing: Copper terraces are covered with individual molecular adsorbates. The step edge on the lower right part of the image is decorated with molecules. We analyzed 32 individual molecules adsorbed on a copper terrace from atomically resolved AFM images. Further molecules were identified to be of the same species as some of the atomically resolved ones from their appearance in STM images. Via the atomically resolved AFM images we found four different species,

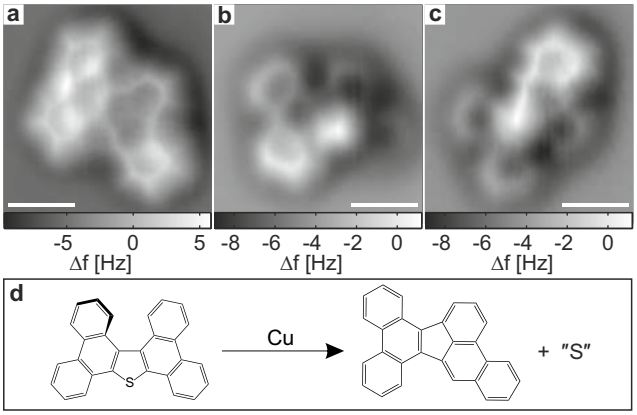

Figure 5.4: Reaction products after annealing on copper terraces: **a—c** Constant-height Δf-images of different reaction products. All products are planar (a) or almost planar (b and c), so that the two phenanthrene moieties can be clearly identified. The latter are attached to each other in a non-symmetric way and are clearly *not* aligned (anti-)parallel. Imaging parameters: $\Delta z = -3.2\,\text{Å}$, $\Delta z = -2.55\,\text{Å}$, and $\Delta z = -2.75\,\text{Å}$ with respect to the STM setpoint ($I = 1\,\text{pA}$, $V = 0.1\,\text{V}$) (Scale bars 5 Å.) **d** Reaction scheme for planar product.

which together account for 30 out of the 32 individual molecules. The remaining two individual molecules must have formed from more than just a single reactant and are disregarded here. One of the four species is the non-reacted DPAT molecule. This observation confirms that the anneal temperature is just at the verge of initiating the reaction. Using the Arrhenius equation [123] we can estimate the activation energy of the planarization reaction: The annealing time of two minutes, the temperature of 200 °C and the observation that 25 out of 30 molecules have reacted provides an energy barrier of $\approx 1.4\,\text{eV}$. The constant-height AFM images of the three remaining species are shown in Figs. 5.4a–c. One of the latter is completely planar, so that its structure can be readily identified from the AFM image (see

Figs. 5.4a and d) as phenanthro(9,10-*e*)acephenanthrylene[4]. None of the bond angles is particularly small, which may indicate that the sulfur was eliminated from the molecule. The molecule does not have an out-of-plane mirror symmetry that would be expected for the simple reaction pathway for planarization discussed above [119]. Instead, the two phenanthrene moieties are now connected to each other at the center of the molecule with different orientations.

Apart from the planar reaction product shown in Fig. 5.4a, there are two more species, displayed in Figs. 5.4b and c, that are not completely planar. While the entire structure is not directly apparent from their AFM images, these do allow for an identification of the orientation of the two phenanthrene moieties. In both cases, the orientation agrees with the one of the planar reaction product. As the central part of the molecule cannot be imaged so clearly, it is at first glance unclear whether a five-membered ring has formed at their center in analogy to the planar reaction product. However, the five-membered ring enforces an orientation of the two phenanthrene moieties in an angle of 150°, whereas a single bond between the two would result in an angle of 180° (see Figs. 5.5b and c). As the observed angle in the AFM images agrees with the former, we conclude that the five-membered ring has to be present. Most probably, the sulfur atom is still present in these molecular structures, giving rise to the additional feature at the center of the target molecule.

Hence, from the AFM images one can assign the backbone of all three products as phenanthro(9,10-*e*)acephenanthrylene – a molecule that has been synthesized from phenanthrene, using wet chemistry [124].

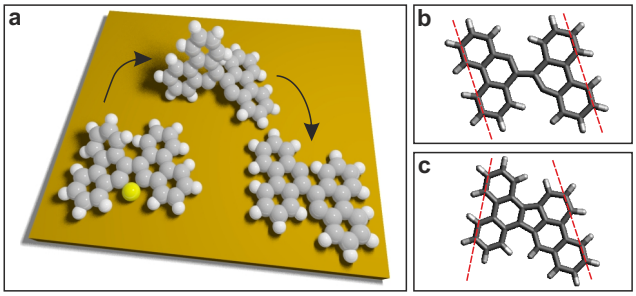

Figure 5.5: A potential reaction pathway: **a** 3D representation of the proposed reaction pathway starting with DPAT on the left hand side. The experimentally observed nonsymmetric arrangement of the two phenanthrene moieties can be explained by a reaction pathway involving an out-of-plane rotation of one of the phenanthrene moieties as depicted by the models from left to right. **b** and **c** stick models of planar reaction products without (b) and with (c) pentagonal ring closure, respectively. The dashed red lines highlight the different alignment of the phenanthrene moieties in both cases. In comparison, all the experimentally observed structures indicate a ring closure in their center. Molecular models in panels b and c were structurally optimized using Avogadro[5].

5.5 Discussion of the reaction pathway

We now turn to the discussion of a potential pathway of the observed reaction. By comparing the reactant and the product (see Fig. 5.4d) and their respective symmetries, one realizes that the two phenanthrene moieties are interconnected quite differently. As illustrated in Fig. 5.5a, a reaction pathway involving the sulfur atom elimination, an (almost) 180° out-of-plane rotation of one phenanthrene unit, and, finally, a ring closure yield the observed molecular structure. Note that, after a bond cleavage at the sulfur atom, the two phenanthrene moieties are connected by a single σ-bond only, facilitating the rotation. Without such an out-of-plane rotation, a reorganization of both

[4]We cannot exclude partial dehydrogenation of the reaction product on the surface.

bonds that connect the two phenanthrene moieties would be required. Such a pathway would not be easily reconciled with the observation of almost all reaction products still consisting of two phenanthrenes – though we cannot exclude such bond reorganization from our data. We therefore propose C–S bond cleavage, the out-of-plane rotation of one phenanthrene moiety, and a ring closure as the reaction pathway. As has been observed previously [8, 125], the surface can coordinate atoms with open bonds that occur from e.g. the sulfur elimination and thereby stabilize intermediate structures, such as the one displayed in Fig. 5.5b. It may well be that the hydrogen that is released upon pentagonal ring closure will saturate the open bond in the final product as shown in Fig. 5.5c. While the planar structure of the reaction product may indicate the saturation of all bonds by hydrogen atoms, we cannot exclude that instead the respective atoms are coordinated to the substrate.

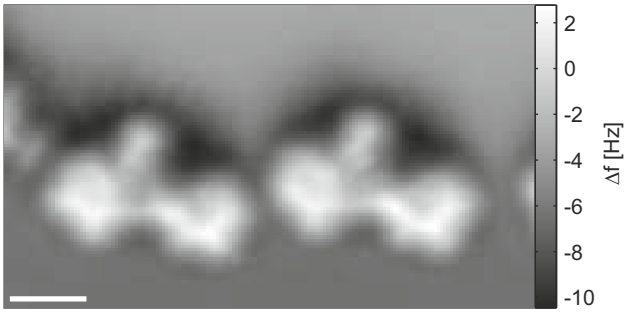

Figure 5.6: Reaction products at a substrate step edge: AFM image of phenanthrene units attached to a copper step edge after sample annealing. The higher reactivity at step edges apparently facilitates dissociation of molecules. Imaging parameters: $\Delta z = -1.55\,\text{Å}$ with respect to the STM setpoint ($I = 1\,\text{pA}$, $V = 0.1\,\text{V}$) at the lower laying terrace in the top part of the image. (Scale bar 5 Å.)

[5] Avogadro — an open-source molecular builder and visualization tool. Version 1.1.0 http://avogadro.openmolecules.net/.

In contrast to our observation, in an earlier work [119] the symmetric reaction product dibenzo[2,3:10,11]perylo[1,12-*bcd*]thiophene was obtained from DPAT molecules in the presence of copper particles serving as a catalytic surface. It is well-known that at step edges the reactivity of the substrate is enhanced [8, 126, 127] which possibly enables alternative reaction pathways. Bearing this in mind, we imaged substrate defect step edges, to which molecules are attached, after annealing. Interestingly, in a corresponding AFM image displayed in Fig. 5.6, we find planar molecules that can be readily identified as containing one of the two phenanthrene moieties only. Hence, step edges obviously facilitate the dissociation of the molecules separating the two phenanthrene moieties. This observation resolves the apparent contradiction of different reactions, as one might speculate that at even higher anneal temperatures the two phenanthrene groups can reunite to form a symmetric reaction product.

5.6 Conclusion

We analyzed the non-planar adsorption geometry of DPAT molecules adsorbed on Cu(111) from atomically resolved AFM data displayed along different planes through a 3D data set. Inside the molecule, the sulfur atom was identified from its characteristic bond angle. Upon annealing the sample, the molecules undergo an on-surface planarization reaction. The reaction pathway is proposed to involve (i) C–S bond cleavage, (ii) an (almost) 180° out-of-plane rotation of one phenanthrene moiety, and (iii) aromatization by dehydrogenation. Finally, the higher reactivity at step edges leads to a dissociation of the molecule separating the two phenanthrene moieties.

6 Determining conformational details of strongly deformed molecules

Most of the work presented in this chapter has been submitted in Nano Letters[1]. Parts of the text are identical to the submitted manuscript.

The last chapter presented a way of determining the structure of 3D molecules. Its geometry was non-planar but still uncomplicated enough to deduce it along three individual planes. In addition, the geometry was rigid and its structural flexibility was limited to the out-of-plane tilt angle of one part of the molecule. In this chapter, the scope of AFM is widened by investigating subtle conformational differences occurring in the well-studied reference systems free-base tetraphenylporphyrin (2H-TPP) and copper-metalated tetraphenylporphyrin (Cu-TPP) on Cu(111).

[1] F. Albrecht, F. Bischoff, W. Auwärter, J. Barth, and J. Repp. 'Direct identification and determination of conformational response in adsorbed individual non-planar molecular species using non-contact atomic force microscopy'. Submitted to *Nano Letters*

6.1 Tetraphenylporphyrin molecules in surface science

Porphyrins and phthalocyanines provide a potpourri of functionalities in, e.g., catalysis [128], molecular electronics [129] or spintronics [130]. Hence they serve as extremely versatile building blocks for 2D-architectures [131–133]. In addition, their properties can be tuned by modifications within their macrocycle [129, 134], by modifying the molecular periphery [135] or through electronic or structural modifications caused by the underlying support [136–138]. Porphyrins with meso-substituents such as tetraphenylporphyrin (TPP) typically exhibit a saddle-shape conformation of their macrocycle upon adsorption onto coinage metal surfaces [134, 138–144]. This saddle-shape adaptation leads to distinct molecular properties such as unusual ligation schemes of adducts [145] or molecular self-assembly [134]. For the understanding of these properties conformational characterizations are essential.

The experimental techniques for porphyrin-based surface science employed so far are mainly STM, STS, X-ray photoelectron spectroscopy (XPS) and near-edge-X-ray absorption fine structure (NEXAFS) [131, 133, 146]. While XPS yields ensemble information about the chemical state of the macrocycle, for example, with STM, topographic and structural investigations of porphyrin arrays as well as single molecules can be carried out in real space. The high lateral resolution of low temperature STM allows gathering local information at the single-molecule level, like the electronic coupling in a metal-organic complex (see chapter 7). The contrast mechanism of STM, however, prohibits a direct interpretation in terms of the sample's geometric shape of STM data, being a convolution of topography and electronic structure of the sample (see e.g. Fig. 5.1). Information on molecular conformation could so far be obtained by synchrotron-based NEXAFS measurements [144] — with the drawback of averaging over countless

molecules and all molecular moieties — or by comparison of STM data with calculated images [139, 147, 148]. As introduced in sections 3.5 and 4.2, small amplitude FM-AFM with CO functionalized tips is capable of structure determination of individual molecules in real space [6, 79, 80, 116, 149, 150]. So far, FM-AFM investigations have mainly been applied to (nearly) planar species adsorbing (almost) parallel to the surface. Few non-planar molecules were investigated in constant height [80, 110, 117, 151]. Chapter 5 presented the investigation of the helical structure of a molecule by analyzing a time-consuming full 3D data set.

6.2 Details of the setup

Individual 2H-TPP and Cu-TPP molecules were sublimed onto a cold Cu(111) surface located within the scanner. The sample was partially covered with bilayer of NaCl to facilitate the pick-up of CO molecules to the tip. All data was recorded using CO functionalized tips [6] and away from NaCl islands.

Additional data was recorded by our collaboration partners in Munich using a separate apparatus (CreaTec LT-STM/AFM). They investigated 2H-TPP molecules sublimed onto a Cu(111) surface held at room temperature. This data is shown in Fig. 6.4e.

6.3 Conventional imaging

The geometries of 2H-TPP and Cu-TPP on Cu(111) are shown in Fig. 6.1a. Both the molecules are well studied in surface science and their structures have been investigated with different experimental approaches [131, 133]. In a simplified view, the conformation of TPP on a surface is determined by steric hindrance of different molecular

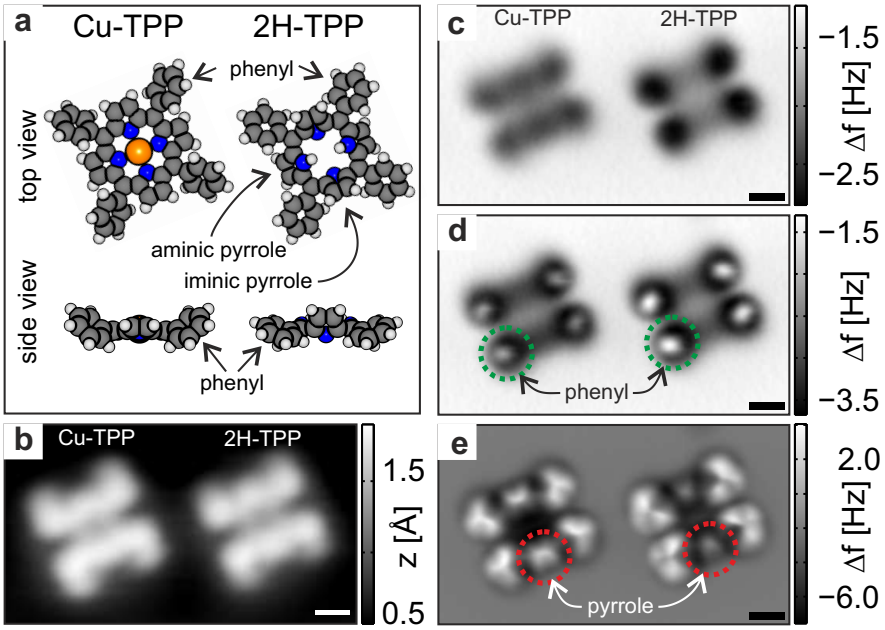

Figure 6.1: Conventional imaging of Cu-TPP and 2H-TPP right next to each other: **a** Top and side view of ball models of Cu-TPP and 2H-TPP. Conformations of adsorbed species are taken from [144]. While 2H-TPP exhibits a pronounced saddle-shape, Cu-TPP is only slightly saddle-shaped with an almost flat macrocycle. **b** Constant-current STM image ($I = 2\,\mathrm{pA}$, $V = 0.1\,\mathrm{V}$) of Cu-TPP (left) and 2H-TPP (right) in the same adsorption orientation on Cu(111). **c**—**e** Constant-height Δf images approaching the surface from $\Delta z = +1.0\,\text{Å}$, to $\Delta z = +0.4\,\text{Å}$, to $\Delta z = -0.8\,\text{Å}$ from the STM setpoint of $I = 2\,\mathrm{pA}$ at $V = 0.1\,\mathrm{V}$. The contrast evolution indicates that — in agreement with previous work — flatter phenyl legs (highlighted by green markers in panel d) are accompanied with a stronger deformation of the macrocycle that can be seen in the tilt of the pyrrole rings (see red markers in panel e). However, the observed flatness of Cu-TPP in comparison to 2H-TPP is not only in quantitative but even qualitative contradiction to the molecular models reported in the literature and depicted in panel a. (Scale bars 5 Å.)

moieties. A rotation of the phenyl legs is linked to the tilting of the pyrrole units of the macrocycle. Flatter phenyl legs, i.e., small angles between the planes spanned by each phenyl ring and the surface plane, thus cause a stronger deformation of the macrocycle. Vice versa, a flattening of the macrocycle will lead to more upright legs. Upon adsorption onto metal substrates, many porphyrin derivatives adapt a saddle-shape conformation [134, 138–145]. The saddle-shape involves a tilting of the pyrrole moieties out of the macrocyclic plane. On Cu(111), the two iminic nitrogens point towards the surface, whereas the pyrrolic/aminic nitrogens point away from it (see Fig. 6.1a). For 2H-TPP on Cu(111) space-averaging NEXAFS measurements of a monolayer coverage of 2H-TPP on Cu(111) give out-of-plane tilt angels of about 50° and 20° for the macrocycle moieties and the phenyl legs, respectively. Upon self metalation the macrocycle of Cu-TPP flattens and the tilt angels of macrocycle and phenyl legs roughly interchange [144]. Hence, TPP molecules do not comprise any hydrocarbon rings parallel or nearly parallel to the surface in contrast to most molecular systems described so far in FM-AFM studies. For molecules with a pronounced 3D deformation — as in the case of TPPs — the chemical structure cannot be directly deduced from conventional imaging. Nevertheless, constant-height imaging can give useful information about the molecular conformation. The parts of the molecule that are higher above the surface interact repulsively with the tip at larger distance (see section 4.2 and references [110, 117]). Therefore, conclusions about relative height differences within a single molecule and for molecules right next to each other can be drawn.

Figure 6.1 shows constant-current STM and constant-height AFM images of a Cu-TPP (left) and side-by-side a 2H-TPP (right) in the same adsorption orientation for direct comparison. For information on how the molecules were identified in the first place, please see further below. In contrast to previous reports [142], Cu-TPP and 2H-TPP show only very subtle differences in STM images (Fig. 6.1b). In line with the

alike STM appearance, the two species only exhibit faint differences in contrast evolution of constant-height Δf images for decreasing tip-sample spacing (see Figs. 6.1c—e).

Mapping Δf at constant height results in the evolution of the contrast from dark areas above the molecule (attractive background) for large tip heights to sub-molecular resolution of the molecular structure at small distances, owing to laterally confined repulsive interactions at the molecular bonds with a bright contrast (see section 4.2 and reference [102]). The protruding parts of 3D-molecules were shown to exhibit bright Δf contrast first (see chapter 5 and references [110, 117]). In the Δf image recorded with the largest tip-sample spacing, the dark attractive regions indicate the outline of each molecule (Fig. 6.1c). With decreasing tip heights, the phenyls interact repulsively (see green markers in Fig. 6.1d) and then, the two opposite pyrroles at the macrocycle follow (red rings in Fig. 6.1e). Although the 3D structure of the molecules prohibits direct imaging of the entire molecular structure, the evolution of repulsively interacting molecular parts fits very well the saddle-shape conformation and reproduces the dependence of the rotation of phenyl rings on the tilt of the pyrrole units qualitatively. The molecule, the phenyl legs of which appear bright at greater distances (Fig. 6.1d), has to be approached closer to detect the pyrroles (Fig. 6.1e). Equivalently, in the picture of the saddle-shape, more upright phenyls correspond to a flatter macrocycle. This means that the macrocycle of 2H-TPP seems to be more flat than that of Cu-TPP, which is inconsistent with the previous NEXAFS result [144]. As will be discussed later, this discrepancy is caused by the different sample temperatures used while depositing molecules in this and the former [144] study.

The differences in the relative heights of distinct molecular moieties as described above allow distinguishing the two species. However, due to the subtle differences between Cu-TPP and 2H-TPP in conventional constant-height imaging, a comparison of individual molecules from different preparations, with different tips or even experimental setups

is not reliable. Instead, this can only be done when directly comparing the two species side-by-side (in the same image, that is, the same tip, the same setpoint, and the same orientation of the molecules). For an unambiguous identification of the molecular species and a reliable comparison of data recorded on different sample preparations and with different tips we applied a different data acquisition scheme, called vertical imaging.

6.4 A new method: Vertical imaging

To acquire vertical images, sets of frequency shift versus distance curves ($\Delta f(z)$) are recorded — see exemplary spectrum in Fig. 6.2b. We subtracted a $\Delta f(z)$ curve recorded on clean copper away from the molecule from each $\Delta f(z)$ spectrum recorded on the molecules to remove background interactions due to the substrate. To record the vertical images in a sufficiently close but safe distance regime, we performed the data acquisition with a threshold criterion as introduced by F. Mohn et al. [120]. The background subtracted $\Delta f(z)$ curves are color coded and displayed as tip height z versus lateral position to generate images in planes perpendicular to the sample surface. The imaging planes were set to coincide with one of the vertical molecular mirror planes according to the molecular C_{2v} symmetry as indicated by the red and green lines in the insets in Figs. 6.2c and d, respectively. Note that the chosen acquisition planes run across the macrocycle only and disregard the meso-substituents. For each frequency shift distance curve, the minimum in $\Delta f(z)$ is determined after background subtraction and its vertical position z_{min} is highlighted by a gray cross in the 2D plots in Figs. 6.2c and d.

Both molecules show two peaks along the profiles of minimum positions that can be assigned to the two opposing pyrroles of the macrocycle. The profiles nicely reproduce the constant-height data, confirming that Cu-TPP exhibits higher pyrrole moieties (see thin dotted

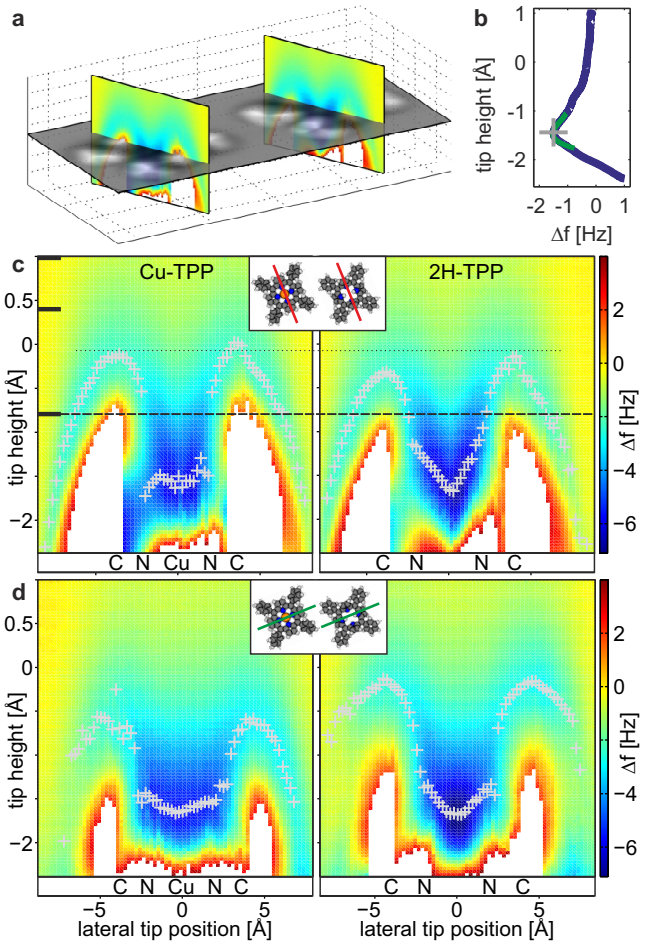

Figure 6.2: Vertical imaging of Cu-TPP and 2H-TPP: **a** 3D representation of vertical images recorded in a mirror plane of each molecule. **b** Example background subtracted $\Delta f(z)$ curve. The gray cross marks the minimum. **c** and **d** Vertical images in the first (c) and second (d) mirror plane. The insets in c and d indicate the mirror planes in which the images were recorded. The thin dotted line in panel c serves as guide to the eye for relative height comparison of the highest molecular parts. The large ticks in c indicate the tip height at which the constant-height images depicted in Fig. 6.1c—e were recorded[2].

line in Fig. 6.2c). While the z_{min} values at the position of the pyrole rings appear smaller for the 2H-TPP molecule as compared to the Cu-TPP (Fig. 6.2c), this trend is inverted in the second mirror plane (Fig. 6.2d). This may be due to the (out of plane) rotation of the phenyl rings, that dominate the contrast in the vertical image in the second mirror plane (for comparison, see Fig. 6.1e).

Importantly, the contours of the minima in vertical images reveal differences between the molecules at the respective macrocycle regions, i.e. between the pyrrole peaks. For Cu-TPP it is flat while for 2H-TPP a pronounced V-shape can be identified (compare Figs. 6.2c and d). To be able to assign these distinct features to a molecular species, reference data was acquired on sample preparations with only one molecular species present at a time. These results were reproducible for several different tips, all adsorption orientations and four different sample preparations and therefore represent general fingerprints of each molecular species. With the help of the fingerprints in the vertical images, unambiguous molecular identification is feasible. From these experiments we, thus, conclusively assign the left molecule in Fig. 6.1 to a Cu-TPP and the right one to 2H-TPP.

The decisive features to discriminate the molecules are located $\approx 1\,\text{Å}$ closer to the sample than the constant-height image at smallest tip-sample spacing (see dashed line in Fig. 6.2c). Recording conventional constant-height images at a reduced tip height is impossible, as the large tip molecule interactions would result in undesired lateral displacement or pick up of the molecule. Moreover, data acquisition for a vertical image is much faster and simpler than recording an entire 3D data set (see chapter 5).

[2] In white areas, a safety Δf limit is exceeded and the measurement is aborted, such that there are no data points available [120]. Positions of the atoms along the mirror plane are indicated beneath the maps. Zero at the tip-height scale corresponds to the STM setpoint height at $I = 2\,\text{pA}$ and $V = 0.1\,\text{V}$. All vertical images were recorded with the same tip and from the same setpoint.

6.5 Reversible conformational switching of Cu-TPP

Cu-TPP can be reversibly switched between two conformational states by the STM/AFM tip, adding a new observation to porphyrin switches [152, 153]. These two states exhibit a clearly discernible current distribution across the molecule (Figs. 6.3a and c) and Δf signal (Figs. 6.3b and d) in conventional constant-height images as well as different vertical images (Figs. 6.3e—g). We henceforth refer to these states as state 1 and 2, whereby the former is the one of the molecules directly after deposition. It is reasonable to assume, that a smaller difference Δh in z_{min} values between the pyrroles and the central metal ion corresponds to a flatter macrocycle (see Figs. 6.3e and f). Hence state 2 appears to be more flat ($\Delta h_{\mathrm{s1}} = 1.5\,\text{Å} > \Delta h_{\mathrm{s2}} = 1.2\,\text{Å}$). This is especially articulated in the vertical images in the second mirror plane (Fig. 6.3g). This vertical image also allows the distinction between 2H-TPP and the switched Cu-TPP molecule (compare Figs. 6.2d and 6.3g). Due to steric hindrance, a flattened macrocycle results in more upright legs and therefore elevates the central metal ion by $\Delta h_{\mathrm{Cu}} = 0.5\,\text{Å}$ (compare thin dotted lines in Figs. 6.3e and f).

Figs. 6.3h and i show high-resolution constant-height Δf images of a Cu-TPP molecule in the two different conformational states. While the overall contrast is rather similar for both molecules, a detailed inspection of the phenyl legs (see red markers) reveals a larger area of homogeneous bright contrast for state 1 as compared to state 2. In line with the interpretation of more upright phenyls in state 2 the contrast

[3] Settings for panels a—d: $\Delta z = +1.0\,\text{Å}$ from the setpoint of 2 pA and 0.1 V on clean copper. Images were recorded at a bias voltage of 0.1 V. The tunneling current images depicted in panels a and c are plotted with the very same gray scale contrast. The same holds true for the Δf data depicted in panels b and d. Zero tip height in panels e—g corresponds to the tip height at the setpoint (2 pA, 0.1 V on clean copper). Settings for panels h and i: $\Delta z = -1.0\,\text{Å}$ from the setpoint of 2 pA and 0.1 V on clean copper.

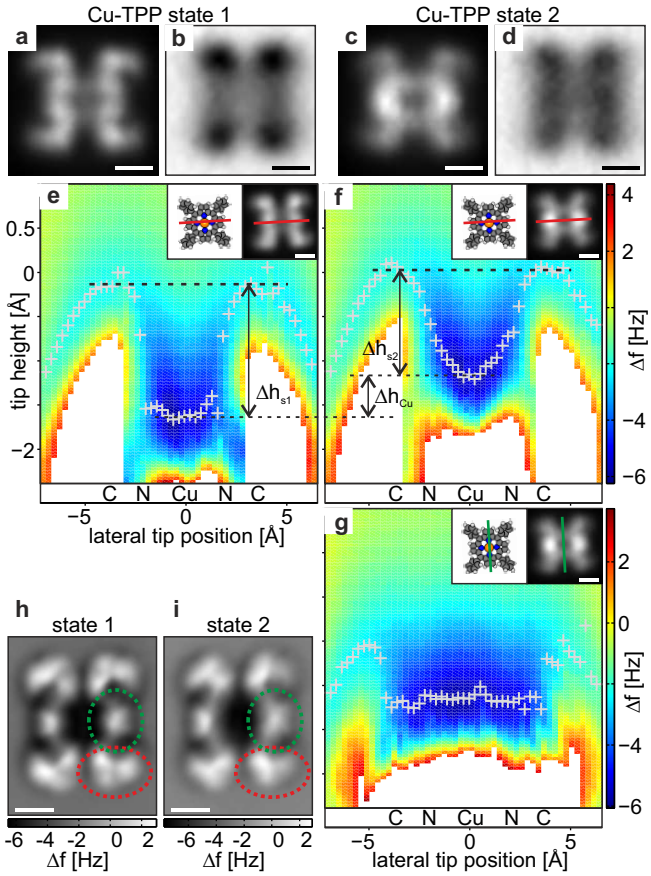

Figure 6.3: Reversible conformational switching of individual Cu-TPP: **a—d** Constant-height current (a, c) and Δf images (b, d) of Cu-TPP in state 1 and 2, respectively. **e** and **f** Vertical images of Cu-TPP for state 1 and 2 in the first mirror plane. State 2 exhibits less height difference between the rim and the center of the macrocycle and is therefore assumed to be more flat than state 1 (compare bold dashed lines in e, f). Additionally, the height of the central Cu ion is increased for state 2 (thin dashed lines in e, f). **g** Vertical image in the second mirror plane for state 2. **h** and **i** Constant-height Δf images of Cu-TPP in both conformational states recorded at small tip-sample spacing. Red and green markers indicate the positions of phenyls and pyrroles. (Scale bars 5 Å.)[3]

at the position of the pyrroles is more corrugated in state 1 (see green markers in Figs. 6.3h and i), indicating more upright pyrroles in state 1. Hence, the conventional AFM images support the assignment of a more flat macrocycle of Cu-TPP in state 2 but are not capable of directly resolving the vertical movement of the central copper ion.

Interestingly, the current channel shows more contribution above two pyrroles for state 2 compared to state 1 and would therefore at first glance — when interpreted as being directly related to geometry — wrongly suggest a stronger macrocycle deformation. Intriguingly, the vertical displacement of the central copper atom does not affect the tunneling current at the center of the molecule. This underlines the difficulty of assigning conformations from STM data alone, which may yield misleading vertical information.

The massive discrepancy of the previously reported conformations and the findings described above lies in the different sample-preparation conditions. On the one hand, in the previous reports TPP was sublimed onto a substrate held at room temperature, while here molecules were evaporated onto a sample held below 10 K. Apparently molecules cannot overcome an energy barrier for adapting their energetically most favorable conformation upon adsorption onto a cold surface but seem to be trapped in a local conformational minimum. On the other hand, an increased molecular coverage deposited at room temperature may enable island formation. This introduces inter-molecular interactions that might affect the conformation of individual molecules through, e.g., T-type interaction [138, 142, 154, 155] and thereby Cu-TPP might switch into the herein described state 2. Apart from preventing inter-molecular interactions the low temperature deposition also eliminates the influence of mobile substrate atoms present at room temperature [156–158].

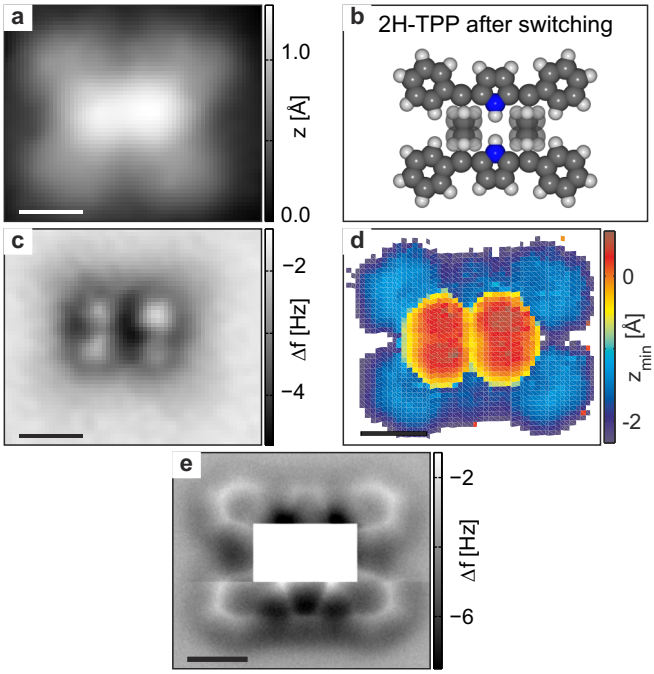

Figure 6.4: Irreversibly switched 2H-TPP: **a** Constant-current STM topograph ($I = 2\,\text{pA}$, $V = 0.1\,\text{V}$). **b** Molecular model of 2H-TPP after switching as deduced from our experimental observations: The molecule is (almost) flat except for the two iminic pyrroles. The exact tilt angle of the upright iminic pyrroles could not be deduced from our experiments, which are therefore depicted with blurriness. **c** Constant-height Δf image recorded at relatively large tip-sample spacing ($\Delta z = 0.0\,\text{Å}$ from 2 pA at 0.1 V). Only four point-like spots at the center of the molecule interact repulsively with the tip indicating the four hydrogen atoms of the two iminic pyrrole rings sticking out furthest from the sample. **d** Map of $z_{\min}$ values recorded over a switched 2H-TPP molecule. At the center of the molecule the $z_{\min}$ values are $\approx 2\,\text{Å}$ larger than on the phenyl legs. A $z_{\min}$ value of zero corresponds to the height of the STM setpoint (2 pA, 0.1 V on clean copper). **e** Composed constant-height Δf image from four scans of a molecule deposited onto a sample held at room temperature ($\Delta z = +0.8\,\text{Å}$ from the STM setpoint of 50 pA at 0.005 V). All molecular parts shown in this image appear flat and (almost) parallel to the sample surface. (Scale bars 5 Å.)

6.6 Conformational conversion of 2H-TPP

Conformational changes can also be induced for 2H-TPP when scanning at elevated bias voltage (2V), however in irreversible manner. In a cross check experiment where molecule were deposited onto a Cu(111) surface held at room-temperature 2H-TPP molecules appear identical to the low-temperature deposited ones after conformation conversion. In STM, these molecules exhibit a central, elongated protrusion that appears higher than the remaining parts (Fig. 6.4a). In constant-height FM-AFM data approaching the surface, moieties interact repulsively first at the macrocycle where one would expect strongly tilted iminic pyrroles. Four repulsive spots at the center of the molecule indicate the hydrogen atoms of the iminic pyrroles sticking out furthest from the sample surface (see Fig. 6.4c). The rest of the molecule only contributes as an attractive background.

Imaging the entire molecule at closer tip-sample spacing to also resolve the phenyl legs is not possible due to the upright orientation of the iminic pyrroles. However, when omitting the molecular center and imaging only the periphery in constant height, the phenyl legs appear ring-shaped showing contrast well know from flat-lying hydrocarbon rings (Fig. 6.4e). Interestingly, at the long edges of the molecule a three-segment bridge between two phenyls can be discriminated. The contrast fits what one would expect for nearly planar pyrroles of the macrocycle. This allows for the suggestion that the macrocycle is strongly deformed with the iminic pyrroles very upright and the aminic pyrroles nearly flat, whereas the phenyl legs are rotated almost coplanar to the surface. Furthermore, to avoid steric hindrance with the nearly flat aminic pyrroles, the legs tilt parallel to the surface as evidenced by the rectangular outline of the molecules.

This model structure is supported by mapping the minima of $\Delta f(z)$ curves on a dense grid across the entire molecule [117] (see Fig. 6.4d). This map shows two features: At the center, the iminic pyrroles stick

out and the $\Delta f(z)$ minima appear at a height of about 0.5 Å. At positions of phenyl legs, the minimum values are ≈ 2 Å closer to the sample and the contrast is very homogenous. We note that a quantitative comparison of z_{min} values at the positions of phenyl legs and iminic pyrroles is not possible due to the different chemical species at different positions of the molecule interacting with the tip. The minor contrast at the phenyl rings implies these rings to be planar on the surface. In addition, the contrast at positions of the aminic pyrroles is flat and shows very similar values as for the phenyl legs. The findings of very upright iminic pyrroles and planar legs are consistent with NEXAFS data on 2H-TPP/Cu(111) [144]. The nearly flat orientation of the aminic pyrroles however has not been addressed so far.

A tip-induced chemical reaction can be ruled out as a cause of the changes as STM data of flattened TPP species that underwent cyclodehydrogenation appear clearly different [134]. It has been shown before that the same TPP species can adapt two different conformations upon adsorption onto metal substrates [151, 159–161]. However, the structural assignment was based on STM data and required theory calculations for data interpretation since STM convolutes topography and electronic structure. Theoretical support is also essential for space averaging NEXAFS measurements to disentangle the contributions from different molecular moieties if the individual resonances overlap [144]. In contrast, high-resolution FM-AFM can provide direct access to the adsorption conformation and the orientation of molecular moieties in real space and is therefore an ideal tool for the investigation of strongly deformed molecules with many degrees of freedom. Utilizing tip induced conformational switching, FM-AFM even allows for a real space structure analysis of different conformations of one individual molecule.

6.7 Conclusion

We presented subtle differences in the adsorption geometry of individual 2H-TPP and Cu-TPP when deposited onto a substrate kept at low temperature. The macrocycle of 2H-TPP appears to be more flat than the one of Cu-TPP, which is different from NEXAFS results deduced from monolayer molecular coverages at room temperature. Furthermore, tip-induced reversible conformational switching of Cu-TPP reveals bistability along with a vertical movement of the Cu center. The study is complemented by the observation of structural adaptations of 2H-TPP exhibiting an extremely deformed macrocycle along with nearly flat phenyl legs. By comparing to data of molecules deposited at room-temperature, the adapted conformation could be identified as the energetically favored one. As novel technique to discriminate and identify conformationally similar species, vertical images mapping $\Delta f(z)$ minima in planes perpendicular to the sample surface were introduced. The applied experimental techniques refine the understanding of the molecular systems and provide information that are neither directly accessible with STM nor from space averaging NEXAFS experiments.

7 Interplay of electronic and geometric structure upon an on-surface reaction

Most of the work presented in this chapter has been published in the Journal of the American Chemical Society[1]*. Parts of the text are identical to the publication. Some of the results are also discussed in [162].*

Chapter 5 presented an example of a thermally activated on-surface reaction. The capability of STM to laterally manipulate single adsorbates [2] may allow adsorbates to be brought into close proximity to finally initiate a chemical reaction [8]. The atomic scale characterization of reactant and product enables comprehensive insight into the details of such a chemical reaction.

7.1 SPM in single molecular chemistry

Whereas most chemical reactions are studied in solution, the gas phase, or their interfaces, some applications demand the development of dry on-surface chemistry. For example, if molecular electronics

[1] F. Albrecht, M. Neu, C. Quest, I. Swart, and J. Repp. 'Formation and Characterization of a Molecule–Metal–Molecule Bridge in Real Space'. In: *J. Am. Chem. Soc.* 135 (2013), 9200.

in the future is to comprise any circuitry, molecules with a delocalized electronic π-system need to be electronically coupled together. Whereas on metal surfaces quite a few examples for such a coupling exist [8, 121, 163–167], a useful molecular electronic device would require being built up on the surface of an insulator [168, 169].

The tremendous progress in recent years of various SPM-based techniques offers the prospect to obtain a complete quantum chemical picture of such dry on-surface chemical reactions, when combined in a single experiment. Single-molecule chemistry by means of SPM enables characterization of chemical bonding in real space and in an atomically well-defined environment (see references [8, 84, 170, 171] and chapter 5). The use of ultra thin insulating films in such experiments made it possible to decouple molecular structures from a conductive support and thereby enable the visualization of the frontier orbitals of constituents and product [9, 172, 173]. FM-AFM imaging has been used to resolve the chemical structure of molecules (see section 3.5). The combination of these techniques offers the prospect of unraveling chemical reaction mechanisms on surfaces and thereby providing an understanding of the interplay of geometry and electronic coupling in metal-organic complexes.

7.2 Experimental and simulation methods

To characterize the formation of metal-organic complexes, phenazine molecules and individual gold atoms were deposited onto the sample at a temperature of T $\cong$ 5 K, with the sample located in the microscope. All experiments were carried out on a bilayer of NaCl on Cu(111). A small amount of CO was dosed onto the surface for tip functionalization during AFM experiments [6].

DFT calculations of the free phenazine monomer and the complex were performed using the ADF2012 program package [174]. The cal-

culations employed the PBE0 exchange-correlation functional, in combination with all-electron basis sets of TZ2P quality for all atoms (ZORA/TZ2P for gold).

7.3 Complex formation and geometric structure

Figures 7.1a and b show the synthesis of the complex from two individual phenazine molecules and a gold atom induced by means of STM manipulation [9, 81, 170, 172, 173]. Prior to the reaction two phenazine molecules are adsorbed close to a negatively charged gold atom (Fig. 7.1a). The synthesis was induced by positioning the tip above one of the molecules (cf. cross in Fig. 7.1a) and ramping down the bias voltage to -2.5 V. A subsequently recorded STM image reveals that a symmetric phenazine-gold-phenazine structure has formed as is displayed in Fig. 7.1b. Identical structures have been formed eight times. In the example shown here, the structure formed in a single excitation step, whereas in other occasions an intermediate step, in which only one phenazine seemed to be bonded to the gold atom, was also observed.

Although the bond motif was chosen such that a bond between the metal atom and the aromatic nitrogen in the molecules was expected, carbon-carbon bonds may have been formed in this reaction [121, 175]. To unambiguously identify which atoms are involved in bond formation, constant-height Δf images were acquired at small oscillation amplitudes with CO-terminated tips as proposed by L. Gross et al. [6]. Figure 7.1d shows such an image of the phenazine–gold–phenazine complex. It clearly reveals that bonds have formed between the metal atom and the aromatic nitrogen atoms. No additional C-C bonds are observed. For comparison, Fig. 7.1e shows a constant-height Δf image of two non-bonded phenazine molecules that are as close to each other as the ones in the complex. The geometry of the complex as deduced from AFM imaging is shown in Fig. 7.1c. Complex formation

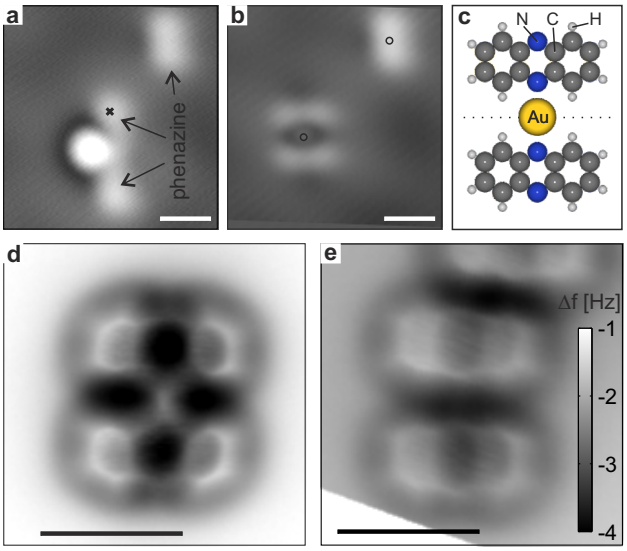

Figure 7.1: Complex formation and analysis of geometric bond structure: **a** Prior to the complex formation two phenazine molecules are adsorbed close to a gold anion. To initiate bond formation, the tip was positioned at the location indicated by the cross and the bias voltage was ramped down to -2.5 V. **b** In a single step a symmetric phenazine-gold-phenazine complex has formed. (Constant-current settings for a, b: $I = 1.0\,\text{pA}$, $V = 0.05\,\text{V}$; images were recorded with a metal tip.) **c** Sphere model of the phenazine-gold-phenazine complex in the geometry as deduced from AFM imaging. **d** Constant-height Δf image of a phenazine-gold-phenazine complex. The only bonds that formed are between the gold atom and the adjacent aromatic nitrogen atoms (CO tip, oscillation amplitude $A = 0.35\,\text{Å}$, $\Delta z = -0.1\,\text{Å}$ with respect to the STM setpoint of $I = 1.0\,\text{pA}$, $V = 0.4\,\text{V}$ on NaCl). **e** Constant-height Δf image of two non-bonded phenazine molecules, for comparison (CO tip, $A = 0.5\,\text{Å}$, $\Delta z = -0.3\,\text{Å}$ from $I = 1.0\,\text{pA}$, $V = 0.4\,\text{V}$ on NaCl; Scale bars 10 Å.)

was found to be reversible. After breaking one of the nitrogen-gold bonds, the separated phenazine molecule showed identical features in STM images as prior to the complex formation.

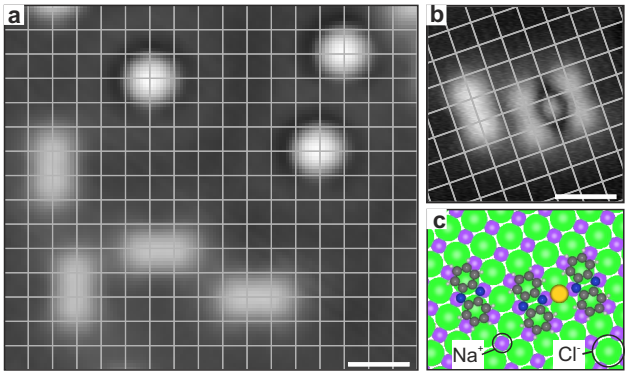

Figure 7.2: Adsorption site determination of phenazine monomer and phenazine–gold–phenazine complex from STM images: **a** Individual gold anions indicate position of Cl ions in the salt lattice [176]. Phenazine monomers adsorb with their centers at Cl bridge sites ($I = 3.5\,\text{pA}$, $V = 0.4\,\text{V}$). **b** Using a monomer as marker, the adsorption site of a phenazine–gold–phenazine complex is determined ($I = 1.0\,\text{pA}$, $V = 0.4\,\text{V}$). The grids in panels a and b indicate the positions of Cl ions. **c** Schematic drawing of the adsorption site of monomer and complex (oriented like in panel b). Only the top-most layer of NaCl is shown. (Scale bars 10Å.)

The determination of the adsorption site of phenazine monomers and phenazine–gold–phenazine complexes is presented in Fig. 7.2: Using individual gold anions as markers [176], phenazine molecules are found to be oriented along the polar direction of the NaCl film and their centers are located at chlorine bridge sites (see panel a). The adsorption site of the phenazine monomer does not change upon complex formation (Fig. 7.2b). The center to center distance of the phenazine molecules within the complex equals two times the spacing of polar rows in NaCl (8 Å).

7.4 Electronic structure of a monomer and a complex

The electronic structure of individual phenazine molecules, as well as that of the complex, were studied using differential conductance (dI/dV) spectra and images (Fig. 7.3). In the experimentally accessible region, the monomer exhibits a single peak centered at 1.7 V corresponding to the negative ion resonance (see dashed red spectrum in Fig. 7.3c). The constant-current image (panel a) acquired at the peak position shows a three lobe structure corresponding to the lowest unoccupied molecular orbital (LUMO) density, as seen in comparison to the DFT-calculated orbital contour (Fig. 7.3b). Note that, the molecular orbital is probed at a very low density in our STM experiments [177].

In contrast, the complex exhibits several features in the dI/dV spectrum, one peak at negative bias[2], and a trapezoidal-shaped feature at positive bias (see solid black spectrum in Fig. 7.3c). The shape of the latter suggests that it consists of two close-lying peaks. The corresponding dI/dV images show three different orbitals, confirming that there are indeed two close-lying peaks at positive bias in the dI/dV spectrum belonging to different molecular orbitals. The fact that the differential conductance spectra of the complex and individual phenazine molecules are qualitatively different directly establishes that chemical bonding has occurred [173], in agreement with the AFM images.

At this point it needs to be emphasized that the dI/dV images of the highest occupied molecular orbital (HOMO) of the complex at negative bias shows a depression at the position of the gold atom (see Fig. 7.3d). As the HOMO is usually assumed to be a bonding orbital, this observation at first glance suggests that no bonding takes place at

[2]The first feature at the negative bias side does not look like an isolated peak since it is influenced by the peak at more negative bias values.

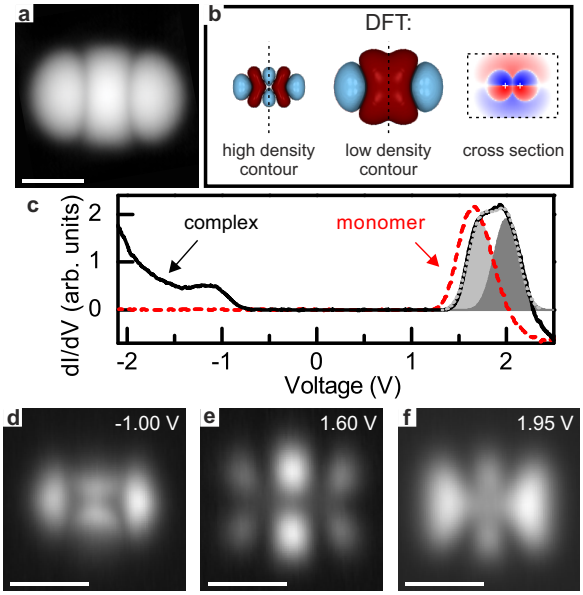

Figure 7.3: STS and dI/dV images of an individual phenazine molecule and a phenazine–gold–phenazine complex. **a** Constant-current STM image of the LUMO of an individual phenazine molecule ($I = 2.5\,\text{pA}$, $V = 1.65\,\text{V}$). **b** Contour of the DFT-calculated phenazine LUMO at high and low orbital density. The shape of the latter agrees well with the STM image in panel a. Low and high density contours show different signs of the orbital structure at the center. The sign change can also be seen in the corresponding orbital density cross section (along dashed lines) through the center of the molecule. White crosses indicate the positions of the nitrogen atoms. The density scale is logarithmic. **c** dI/dV spectra of a phenazine monomer (dashed red curve) and a phenazine–gold–phenazine complex (solid black curve). Spectra were acquired at the center of monomer and complex as indicated by black circles in Fig. 7.1b. The phenazine monomer exhibits only one resonance at 1.7 V. In contrast, the complex shows one peak at negative bias and two close-lying peaks at positive bias voltage. Gray and light gray filled areas indicate two Gaussians that result in a good fit of the spectrum at positive bias (the dotted gray line shows the sum of the two Gaussian peaks). Data points are averaged over 28 mV. **d—f**, Constant-height dI/dV images of a complex acquired at bias voltages as indicated. The complex is oriented as depicted in Fig. 7.1c. (Scale bars 10 Å.)

the gold atom. This highlights the importance of the complementary characterization by means of atomically resolved AFM imaging. This apparent contradiction will be resolved further below.

The charge state of individual phenazine molecules was identified by their effect on the interface state scattering [176, 178, 179]. Individual phenazine molecules do not scatter the interface state electrons, hence they are neutral. Note that gold atoms are known to have two stable charge states on this surface [176]. The complex is found to scatter the interface state electrons, indicating that it is negatively charged. A negatively charged complex has an even number of electrons, which is in line with the observation of different orbital structures at positive and negative bias voltage polarity [172]. It is also consistent with the lower apparent height of the phenazine part of the complex as compared to individual phenazine molecules in low bias STM images (see Figs. 7.1b and 7.2b and reference [179]).

Next, we turn to the discussion of the orbital structure of the complex. When comparing the nodal plane structure of the dI/dV images of the individual phenazine molecules with that of the complex, one realizes that all three orbitals of the complex (Figs. 7.3d—f) show nodal planes at the positions where two close lying non-bonded phenazine molecules would also have nodal planes. The only differences lie in the nodal plane structure along the symmetry plane separating the two phenazine constituents (cf. dotted line in Fig. 7.1c). Hence, all orbitals appear to be composed of the LUMOs of the individual phenazine molecules but with varying phases. As discussed above, only one state (LUMO) is observed in the differential conductance spectrum of an individual phenazine molecule. DFT calculations showed that the LUMO of the phenazine monomer is nondegenerate and separated by 4 eV and 1.8 eV from the HOMO and the LUMO+1, respectively. For the gold atoms, also only one state is expected to be close to the Fermi level, namely the 6s state [176].

7.5 Electronic coupling model

We will now apply a basic quantum chemical model to rationalize the electronic structure of the complex: the linear combination of orbitals method [180–183]. To apply the model, we combine the two phenazine LUMOs and the gold 6s orbital while making use of the above mentioned symmetry plane to form three complex orbitals. All orbitals of the complex must be either symmetric or antisymmetric with respect to the corresponding mirror operation. The two LUMOs of the two phenazine molecules thus form a symmetric and an antisymmetric combination. The gold 6s orbital can only contribute to the symmetric combination of the two LUMOs because of its s-character. Since the numbers of resulting orbitals must correspond to the number of linearly combined orbitals, this leaves us with one antisymmetric orbital without a contribution from the gold and two symmetric orbitals, in which the gold 6s orbital contributes with opposite sign. The above reasoning is sketched in Fig. 7.4. Different colors indicate different signs of the wave function. Note the good agreement of the nodal plane structure predicted by this basic quantum chemical model and the experimental dI/dV images.

Key to understanding the shape of the HOMO is the realization that the phenazine LUMOs have a nodal plane in the molecule plane (see orbital density cross section in Fig. 7.3b). If the gold atom is closer to the surface than the two phenazine molecules, it couples to the lower part of the wave function that has opposite sign from its value probed by the STM tip from above. Hence, for an in-phase coupling below the molecular plane, the STM senses two nodal planes from the top giving rise to the depression in the HOMO image at the position of the gold atom. The appearance of the LUMO+1 can be rationalized by similar arguments. DFT-calculated contours of the complex' orbitals support this reasoning and are shown in Fig. 7.5.

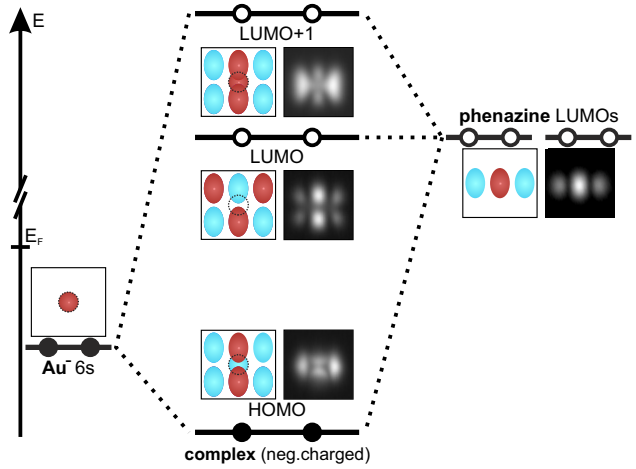

Figure 7.4: Schematic level diagram and basic orbital model: Light blue and dark red indicate different signs of the wave function — depicted in top view. The three constituents' orbitals being combined are the Au^- 6s state (left) and two unoccupied phenazine LUMOs (right). Due to the complex' symmetry, only the phenazine LUMOs couple to the complex' LUMO. The Au 6s contributes to the complex' HOMO and LUMO+1. For DFT calculated orbital contours see Fig. 7.5.

DFT calculations of the complexes were done fixing the geometry of both phenazine molecules in the same plane. The relaxed structure of the monomer was taken as input for the two molecules in the complex. We varied both the molecule-molecule distance (from 14 Å to 8 Å center-to-center) and the vertical offset of the Au atom with respect to the plane of the molecules (from 0 Å to 1.3 Å). In all cases we found that the HOMO, LUMO, and LUMO+1 of the complex are derived from the LUMO of the phenazine molecules and the gold 6s state. For example, these orbitals of the complex with a molecule-molecule spacing of 9 Å and a vertical offset of the gold atom of 1.1 Å are shown in the second row in Fig. 7.5. The cross sections through the DFT-calculated orbitals confirm the picture that the depression

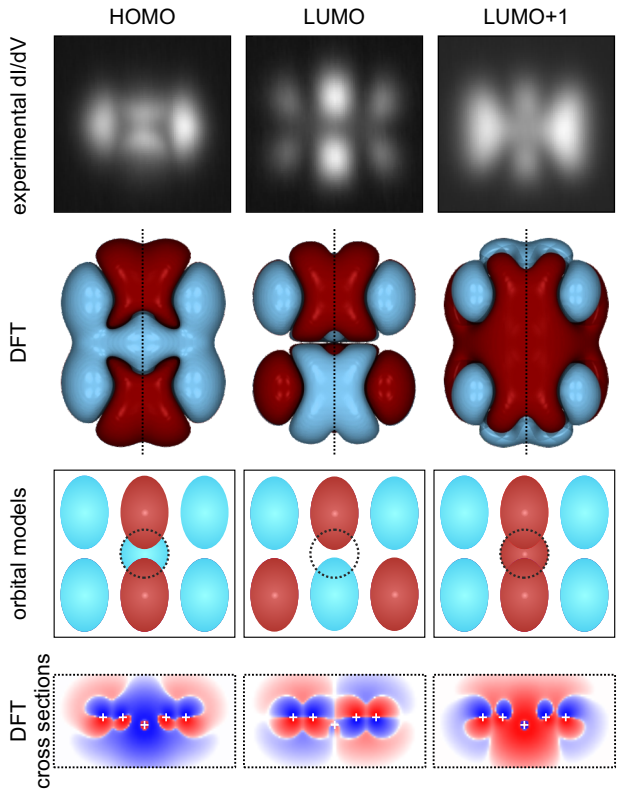

Figure 7.5: Comparison of experimental orbital images, DFT-calculated orbital contours, and cross sections through the DFT-calculated orbitals of the phenazine–gold–phenazine complex: **Top row** Experimental constant-height dI/dV images of HOMO, LUMO and LUMO+1. **Second row** Low-density contours of DFT-calculated orbitals. **Third row** Top view of corresponding orbital schemes as derived from our basic model. **Bottom row** Cross sections through the DFT-calculated orbital densities in the plane spanned by the gold and nitrogen atoms (indicated by dotted lines in the second row). White crosses indicate the positions of the gold and nitrogen atoms. The nodal plane directly at the gold atom in the case of HOMO and LUMO+1 is due to the outermost change of sign of the gold 6s orbital. The density scale is logarithmic.

in the HOMO image at the position of the gold atom arises from two close lying nodal planes, even though the gold 6s state couples in-phase to the phenazine's LUMOs. As discussed above, this is a result of the gold atom being closer to the surface than the two phenazine molecules, where it couples to the lower part of their orbitals.

A quantitative agreement with the experiment cannot be expected since the substrate was not taken into account for the calculations. We find best agreement between the experimental images and calculated orbital contours for a molecule-molecule spacing of 9 Å, whereas the experimentally determined distance was 8 Å. We attribute this disagreement to neglecting the substrate in the calculations. Most importantly, the DFT calculations support the applicability of our basic model, which in turn provides insight into the electronic coupling inside the complex.

Our DFT calculations also showed that the order of complex orbitals depends on the center-to-center distance between the phenazine molecules. This is rationalized from the sign change in the cross section of the phenazine monomer's LUMO (see orbital density cross section in Fig. 7.3b and schematics in Fig. 7.6). For large distances between the phenazine molecules within the complex an in-phase coupling of a gold atom below the molecular plane corresponds to the phase of the gold 6s orbital being represented by blue color (in the color code of the top left sketch in Fig. 7.6). The fraction of the complex' wave function having a phase corresponding to the blue color is enhanced in the center of the complex. When the two phenazine molecules are closer to each other the fraction of the gold 6s orbital overlapping with the inner phenazine LUMO lobe (depicted in red) increases (see top right model in Fig. 7.6). At a small phenazine-phenazine spacing this overlap becomes dominant and an in-phase coupling between the phenazine LUMO and the gold 6s orbital corresponds to the gold orbital having red phase — which is the opposite phase as in the case of a large spacing between the phenazine molecules. In case of out-of-phase coupling the situation is similar:

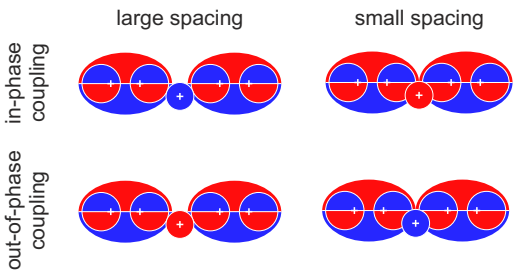

Figure 7.6: Distance dependent order of complex' orbitals: Cross sections of complex' orbital models for large (left column) and small phenazine-phenazine spacing (right column). Red and blue represent different signs of the wave function. **Top row** shows orbital models for in-phase coupling of the gold 6s orbital and the phenazine LUMOs — these orbitals correspond to the complex' HOMO. **Bottom row** illustrates orbital cross sections for out-of-phase coupling — representing the complex' LUMO+1. White crosses illustrate the positions of the gold and nitrogen atoms.

The phase of the gold 6s orbital changes when going from small to large phenazine-phenazine spacing (see bottom row in Fig. 7.6).

Apparently the order of the two corresponding orbitals — the complex' HOMO and LUMO+1 — inverts with increasing the spacing between the two phenazine molecules. Since the complex' LUMO stems from phenazine LUMOs only it is not affected by the coupling to the gold 6s orbital. The experimentally observed phenazine-phenazine distance seems to be heavily affected by the NaCl layer underneath (see adsorption site determination in Fig. 7.2). Hence exchanging the gold atom by a metal with a significantly different atomic radius might invert the experimentally observed orbital order. Although these considerations show the influence of the geometric arrangement of the complex' constituents, this does not affect the basic picture of the proposed electronic coupling scheme.

Finally, we turn to the discussion of the energies of the resonances. The gold 6s state contributes one electron to the frontier orbitals of

the complex. Because of the overall negative charge of the complex, there is one additional electron. Since only unoccupied non-degenerate states of the phenazine molecules contribute to the orbitals of the complex, one of the three orbitals of the complex is doubly occupied and the other two states remain empty. As the HOMO and the LUMO resonances correspond to the temporary removal and addition of an electron, respectively, their peak separation in the experimental dI/dV spectrum is partially due to the Coulomb charging energy [4]. However, as the peaks corresponding to LUMO and LUMO+1 both involve the temporary addition of one electron to an orbital with similar spatial extension, their peak separation can be interpreted to be the energy difference between the two electronic states [184]. Fitting these peaks in the dI/dV spectrum of the complex at the positive bias side with two Gaussians of the same width yields a peak spacing of (0.30 ± 0.03) eV (Fig. 7.3c). The good agreement of the experimental LUMO and LUMO+1 images with symmetric and antisymmetric combinations of the phenazine's LUMOs may allow for a quantitative interpretation of their energy separation in analytical models. We would like to emphasize, that, whereas DFT-calculated orbital images of the complex qualitatively agree with the experimental observations (see first and second row in Fig. 7.5), the interpretation in terms of an electronic coupling is not straightforward from DFT simulations but can be provided by analytical models.

7.6 Conclusion

We described a model on-surface synthesis reaction on an ultra-thin insulating layer on the single molecule level. Using combined STM and AFM, the electronic and geometric structure of reactants and products was characterized. Both the energetic positions, as well as the nodal plane structure of the orbitals of the metal-ligand complex can be explained by the linear combination of orbitals method. Hence, we

demonstrate that the combination of STM and AFM enables a direct quantification of the interplay of geometry and electronic coupling in metal-organic complexes in real space.

8 Visualizing the polarity of an individual chemical bond

Most of the work presented in this chapter has been published in Physical Review Letters[1]. Parts of the text are identical to the publication.

After demonstrating the capabilities of SPM in the framework of electronic and geometric structure determination of an individual molecule we will now turn to the investigation of static electric charges within single molecules adsorbed on surfaces. In this chapter we utilize AFM to deduce intramolecular charge distributions.

8.1 Charge sensing in AFM

The use of a well-defined functionalization of a scanning probe tip with one CO molecule has enabled submolecular resolution in FM-AFM resolving the chemical structure of individual molecules [6]. Since then, this technique has been widely applied [47, 87–98]. Referring to the introduction section 2.3, AFM-based KPFS [11, 12] provides the $LCPD$ between tip and sample [44, 185, 186]. As surface charges and dipoles affect the local work function, $LCPD$ is intimately linked to the charge distribution at surfaces [45, 60] such that KPFS has been used to determine the charge state of individual adatoms [66, 187] and

[1] F. Albrecht, J. Repp, M. Fleischmann, M. Scheer, M. Ondráček, and P. Jelínek. 'Probing Charges on the Atomic Scale by Means of Atomic Force Microscopy'. In: *Phys. Rev. Lett.* 115 (2015), 076101.

molecules [188, 189], for example. Hence, the use of tip functionalization in KPFS promises the mapping of charge distributions at ultimate resolution and inside molecules, which is key to the understanding of basic processes in many fields, e. g., organic photovoltaics. Mapping of the quadrupole moment in a molecular switch [13] and of the dipole moment in donor-acceptor molecules [14] has been achieved with CO-terminated AFM tips recently. However, to attain charge resolution at the level of individual bonds, the probe has to be brought so close to the sample that other force contributions also become important. In this regime KPFS maps have shown a contrast inversion, which hints that they may not reflect the charge distribution anymore [14].

8.2 Methods

We study trimeric perfluoro-ortho-phenylene mercury ($F_{12}C_{18}Hg_3$) and its hydrogen-terminated counterpart $H_{12}C_{18}Hg_3$, exhibiting bonds of different polarities and intramolecular charge distributions at the atomic scale. In addition, we performed experiments with perylene-3,4,9,10-tetracarboxylic dianhydride (PTCDA) and 10-chloro-anthracene-9-carbonitrile (ClAnCN). Due to charge transfer with the substrate, the former is expected to show a charge distribution rather delocalized over the entire molecule. The different side groups of ClAnCN provide a model system for an in-plane dipole.

The compounds $F_{12}C_{18}Hg_3$ [190] and $H_{12}C_{18}Hg_3$ [191] were synthesized by our collaboration partners in the chemistry department of the University of Regensburg. The assignment of the species was achieved by experiments, in which only one species was deposited onto the sample at a time. All investigations of $F_{12}C_{18}Hg_3$, $H_{12}C_{18}Hg_3$, and PTCDA were performed on the molecules directly adsorbed on Cu(111), whereas ClAnCN was studied on a double layer of NaCl on Cu(111). Unless otherwise specified, the tip was functionalized with a

CO molecule. All spectroscopy data was acquired in constant-height mode.

Calculations of $F_{12}C_{18}Hg_3$ and $H_{12}C_{18}Hg_3$ on Cu(111) are based on total-energy density-functional theory (DFT) [192] (for details, see section A.4).

For the data analysis in this chapter we required the absolute tip-sample distance. For tips functionalized with a CO molecule, the tip heights were deduced as follows. First, we estimated the absolute tip-sample spacing from the fitting of the frequency shift acquired above the clean copper substrate. From the KPFS data at different tip heights, we extracted the frequency shift $\Delta f^\star$ at the maximum position of Kelvin parabolas $\Delta f^\star = \Delta f(V^\star)$. Fitting those $\Delta f^\star$ values to a Lennard-Jones potential yields an estimation for the absolute tip-sample distance z. According to this method of calibration, an STM setpoint of 0.5 nA at a bias of 0.1 V corresponds to a spacing of 8 Å between the oxygen atom of the CO tip and the topmost layer of the copper sample (center-to-center distance).

Another way to determine the absolute tip-sample spacing has been proposed by L. Gross et al. [6]. The minimum of a $\Delta f(z)$ curve above the center of a benzene ring is expected to occur at a distance, for which the center of the oxygen atom of the tip is about 4 Å above the plane of carbon atoms. According to our DFT calculations, the (tilted) carbon rings of $F_{12}C_{18}Hg_3$ are about 3.2 Å above the copper substrate. According to this calibration method, the STM setpoint (0.5 nA; 0.1 V) corresponds to a tip-sample spacing of $\approx$ 6.5 Å (oxygen to copper). This value is slightly smaller than the 8 Å deduced from the first calibration scheme. In the experiments presented here the electric field between tip and sample is required and at the atomic scale it is not obvious, which absolute distance is to be used for the $1/z$-dependence of the electric field in the junction. Therefore, we assume that it is not the oxygen-to-copper center-to-center distance,

but slightly larger than that. We, therefore, assumed our setpoint corresponding to an effective absolute distance of $z = 8\,\text{Å}$.

8.3 Intramolecular charge distribution deduced from KPFS maps

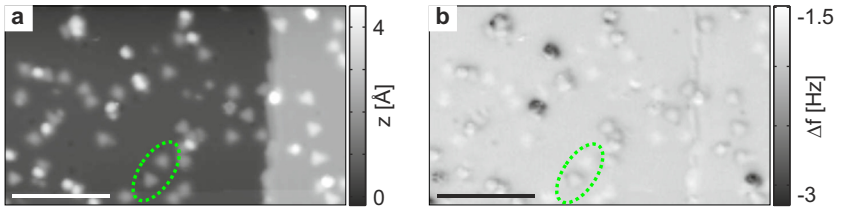

Figure 8.1: Identifying $F_{12}C_{18}Hg_3$ and $H_{12}C_{18}Hg_3$ molecules in an overview image: **a** Constant-current topography image of two adjacent copper terraces covered with $F_{12}C_{18}Hg_3$ and $H_{12}C_{18}Hg_3$ molecules and some additional adsorbates. In this topograph the two molecular species are indistinguishable. **b** Simultaneously recorded Δf channel: Here, $F_{12}C_{18}Hg_3$ and $H_{12}C_{18}Hg_3$ appear differently and allow the identification of a $F_{12}C_{18}Hg_3$ next to an $H_{12}C_{18}Hg_3$ molecule (see green markers). Images were recorded with a metal tip at a constant current of 1 pA at 0.25 V bias voltage. (Scale bars 100 Å.)

To unambiguously relate the experimental data to the polar nature of bonds, we compared $F_{12}C_{18}Hg_3$ and $H_{12}C_{18}Hg_3$ molecules adsorbed next to each other in the same data set, acquired with the same tip apex. Figure 8.1 shows how a pair of $F_{12}C_{18}Hg_3$ and $H_{12}C_{18}Hg_3$ molecules was identified on the sample surface. While the two molecules appear very similar in the constant-current STM topography (panel a), the two species are distinguishable in the simultaneously recorded Δf channel (see panel b): The two molecules highlighted with green ellipses are the ones investigated in the following.

Figures 8.2a and c show a model of the chemical structure and a Δf image of both molecules, respectively. To map out the local contact

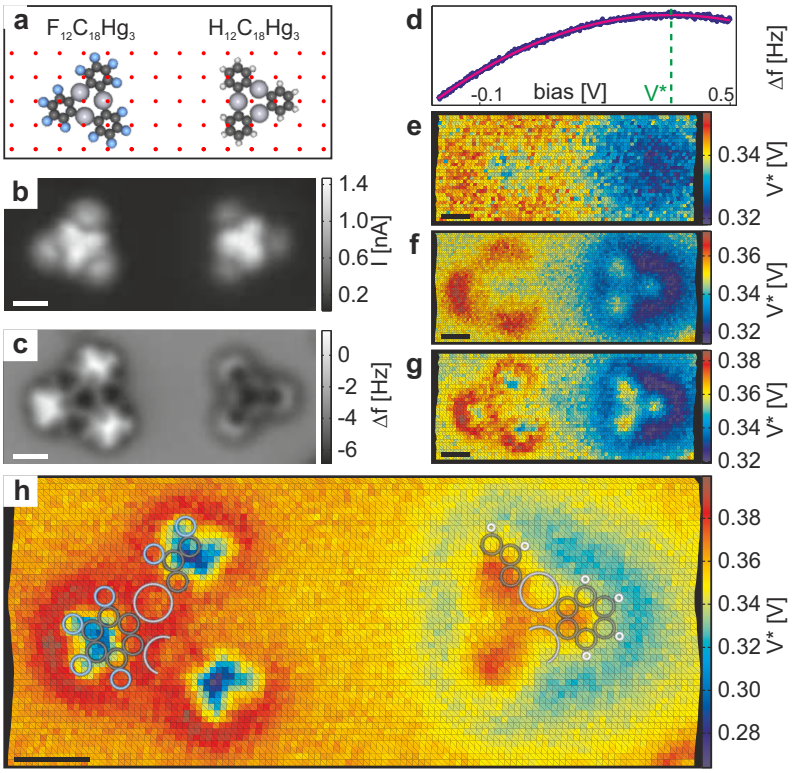

Figure 8.2: KPFS on grids on individual $F_{12}C_{18}Hg_3$ and $H_{12}C_{18}Hg_3$ molecules. **a** Ball models of $F_{12}C_{18}Hg_3$ (left-hand side) and $H_{12}C_{18}Hg_3$ (right-hand side) shown in the same orientation as the molecules under investigation. Carbon, mercury, hydrogen, and fluorine atoms are represented in black, gray, white, and blue, respectively. At each point of a dense grid over the molecules (schematically indicated by red dots) individual spectra are acquired. **b** Constant-height current image of the two molecules ($z = 9.6$ Å, $V = 0.2$ V). **c** Constant-height Δf image ($z = 9.0$ Å). **d** Exemplary KPFS spectrum (blue) of one grid point with parabolic fit (pink) from which $V^\star$ is extracted (green). **e**—**h** $V^\star$ maps acquired at $z = 12.0$ Å, 10.1 Å, 9.8 Å and 9.6 Å. The experimental data in panel h is partially overlaid with models to indicate the position of individual atoms. (Scale bars 5 Å.)

potential difference between the CO-functionalized tip and the sample, KPFS spectra [12] have been acquired on a dense grid of sample points over the molecules (for the details of this particular mode of data acquisition, see section 3.4). Each KPFS spectrum $\Delta f(V)$ shows a parabolic shape, see Fig. 8.2d, and from a fit to a parabola, the voltage $V^\star$, at which $\Delta f(V)$ has its maximum, is extracted. Figures 8.2e—h show maps of $V^\star$ values with decreasing tip-sample distance. For a relatively large distance of 12.0 Å (Fig. 8.2e), the $V^\star$ map shows a contrast that is expected from an interface dipole formation [60]. For the remainder, it is important to realize that any charge at the surface of the metal substrate will be screened efficiently (the image-charge effect) leading to a dipole rather than an isolated point charge [193]. Because of this and the superposition principle, any distribution of charges at a metal surface can equally be described by a set of dipoles, each perpendicular to the surface, see the inset in Fig. 8.4a. Each of these dipoles will change the $LCPD$. This highlights the direct link between charges inside the adsorbate, the resulting surface dipoles and $LCPD$. Upon approaching the surface slightly, Fig. 8.2f, the $V^\star$ contrast increases and shows higher lateral resolution. The largest shifts of the $V^\star$ signal are observed at the circumference of the molecule. In agreement with this observation our DFT simulations reveal that the interface dipoles at the two molecules of −1.16 D and +3.87 D, respectively, are mainly due to vertical relaxations of the polar peripheral bonds of opposite polarity ($C^{\delta+}$–$F^{\delta-}$ vs. $C^{\delta-}$–$H^{\delta+}$), (see Fig. 8.6b). At the closest distance in the experiment, Fig. 8.2h, mercury atoms within $F_{12}C_{18}Hg_3$ become apparent. In addition, the contrast inverses at the outer part of the phenylene groups, where it shows sharp red to blue transitions. Although this intramolecular contrast is remarkable, such a contrast inversion is incompatible with the simple interpretation in terms of $LCPD$ [14].

One possible contribution to the KPFS signal at close distances is the so-called phantom force [68] resulting from the tunneling current. However, a strong influence of phantom force can be excluded here,

because (i) the tunneling current image (Fig. 8.2b) bears no resemblance to the features of the contrast inversion, and (ii) the current is similar for both molecules, whereas $V^\star$ is strikingly different.

Instead, it has been speculated that the contrast inversion stems from the probe penetrating the molecule's electron shell so that the unscreened core charges contribute to the KPFS signal [14]. Electrostatic force contributions give rise to the parabolic dependence of $\Delta f(V)$ (see references [12, 60] and section 2.3). From the above reasoning, no deviation from a parabolic shape is expected. Therefore, we analyzed the residuals of the parabolic fit to the KPFS spectra for different distances, as is shown in Fig. 8.4b. Whereas, at large distances, the residuum is a random noise signal it shows structure not compatible with noise at close distances. This systematic deviation from a parabolic shape points toward a contribution to the signal involving not only electrostatics.

The large electric fields in the junction on the order of $10^9\,\mathrm{V/m}$ that occur upon acquisition of a KPFS parabola will lead to a relaxation of the positions of atoms that carry net charge (ionic polarization), and a Stark effect of the electron shell (electronic polarization). Both effects will affect the overlap of the electron shells of tip and sample, contributing to the Pauli repulsion and hence to Δf in the close-distance regime [103]. As the Pauli repulsion is very short range in nature, even tiny relaxations lead to an appreciable signal. The above considerations provide a good reason why KPFS fails to reproduce $LCPD$ in this regime. Upon sweeping the bias voltage, the sample and tip will undergo relaxations affecting the Pauli repulsion and hence the frequency shift. Since this involves nonelectrostatic interactions, a deviation from a parabolic shape of $\Delta f(V)$ can be expected. Even if this deviation is not immediately apparent from looking at the data, the fit of $V^\star$ might be heavily affected. To analyze this, we evaluated the goodness of the parabolic fit to the experimental $\Delta f(V)$ spectrum for each pixel of the KPFS data on $F_{12}C_{18}Hg_3$ and $H_{12}C_{18}Hg_3$ molecules.

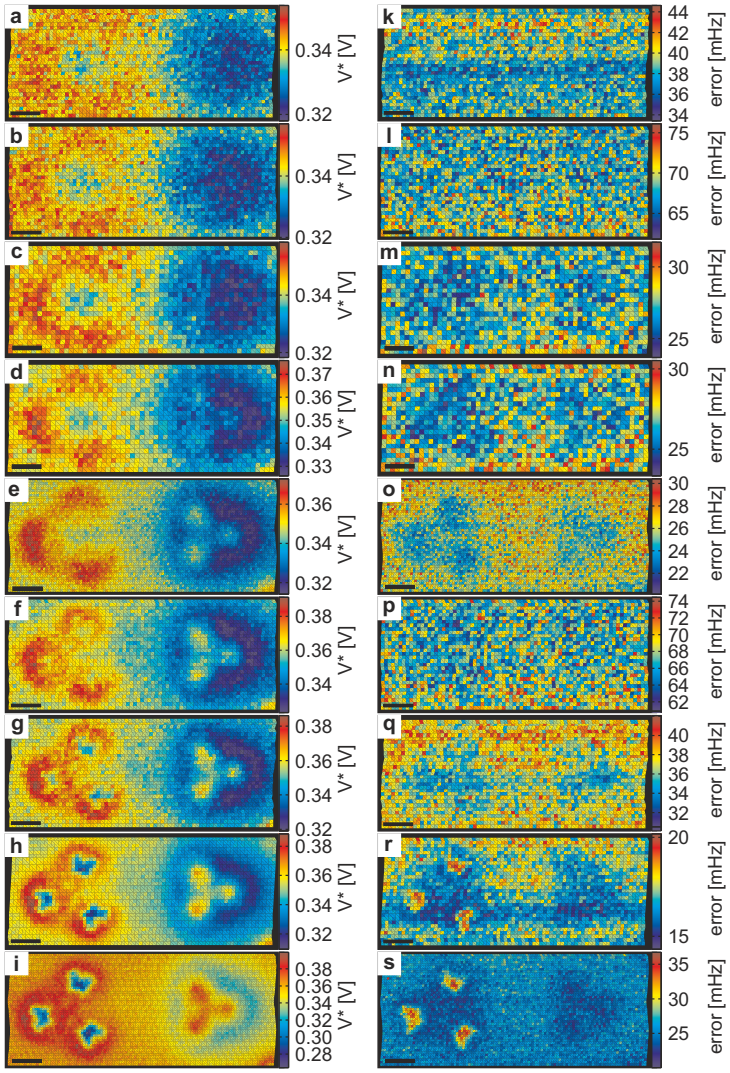

Figure 8.3: Full set of $V^\star$ maps (left column) and RMS errors of parabolic fits (right column) of $F_{12}C_{18}Hg_3$ (left molecule) and $H_{12}C_{18}Hg_3$ (right molecule): Data sets were acquired at tip-sample spacings of (top to bottom) 12.0 Å, 11.5 Å, 11.0 Å, 10.5 Å, 10.1 Å, 9.9 Å, 9.8 Å, 9.7 Å, and 9.6 Å. (Scale bars 5 Å.)

The left column of Fig. 8.3 shows the full set of $V^\star$ maps. The right column of Fig. 8.3 shows the errors of the parabolic fits to experimental data. Each pixel of these maps corresponds to the average RMS fit residual of one entire KPFS curve and provides a measure of the goodness of the parabolic fit. At positions of highest contrast in $V^\star$ maps (cf. Figs. 8.3h—i), the error of the parabolic fits becomes larger (cf. Figs. 8.3r—s). Note that the absolute scale of these error maps depends on experimental parameters like the voltage range or the acquisition time for each parabola, and hence, cannot be compared between different data sets. However, systematic errors in the fits can be identified at spots, at which the error maps do not just show random noise but distinct features. This holds true for the features at the positions of the C-F bonds of $F_{12}C_{18}Hg_3$ at the two closest data sets.

8.4 Concept of deducing dipoles from $\Delta f(z)$ spectroscopy

Whereas the above considerations hint toward a fundamental limitation of KPFS to reproduce $LCPD$ at very close distances, they offer a route to overcome the limitations of KPFS in charge detection, as follows. The basic idea of the novel scheme is to better disentangle electrostatic from nonelectrostatic contributions of Δf from their different distance dependence [26]. In addition to KPFS spectra $\Delta f(V)$ (at a given tip height), we acquired $\Delta f(z)$ data for two distinctly different bias voltages V_i, see the 3D schematic in Fig. 8.4a. Both of these $\Delta f(z)$ curves are expected to display the distance dependence of the forces (or—more precisely—the tip-sample stiffness $\partial F_z/\partial z$) between tip and sample molecule. The interactions other than electrostatic in origin can be modeled by a Lennard-Jones potential; we therefore refer to the part of the $\Delta f(z)$ signal resulting from these contributions as $\Delta f_{\mathrm{LJ}}(z)$. A vertical relaxation δz resulting from the drastic change of

bias voltage will—in good approximation—simply shift the two $\Delta f(z)$ curves with respect to the vertical position z, so that

$$\Delta f_{\mathrm{LJ}}(z, V_2) \simeq \Delta f_{\mathrm{LJ}}(z + \delta z, V_1).$$

As these relaxations are expected to be small, a Taylor expansion yields that the difference

$$\begin{aligned} \Delta f_{\mathrm{LJ}}(z, V_2) - \Delta f_{\mathrm{LJ}}(z, V_1) &\simeq \Delta f_{\mathrm{LJ}}(z + \delta z, V_1) - \Delta f_{\mathrm{LJ}}(z, V_1) \\ &\simeq \delta z \cdot \Delta f'_{\mathrm{LJ}}(z, V_1) \end{aligned}$$

equals the product of δz times the derivative

$$\Delta f'_{\mathrm{LJ}}(z, V_1) = \partial \Delta f_{\mathrm{LJ}}(z, V_1)/\partial z.$$

Hence, the extraction of the difference signal may directly provide information about the ionic polarization of molecules on surfaces.

Moreover, the two $\Delta f(z)$ spectra will also contain several electrostatic contributions that can be classified [59, 194] in the ones that stem from the overall electrostatic tip-substrate interaction and those from local charges in the junction. The former can be eliminated by subtracting the $\Delta f(z)$ signal acquired away from the molecule on the bare substrate from each of the spectra at the given voltage. Henceforth, $\Delta f(z)$ refers to the background subtracted signal. Note that this background subtraction will not affect the considerations discussed in the previous paragraph. What remains are the contributions from local charges inside the junction. We make use of the fact that in the presence of the metal they can be described by a set of vertical dipoles (see above and Fig. 8.4a). Each of these dipoles interacts with a local electric field in the junction. Even though the shape of the electric field is not straightforward in the presence of the tip, we approximate it for simplicity as $(V - LCPD)/z$, where V denotes the applied bias voltage and z is the tip-substrate distance[2].

[2]Note that the dipole under consideration is in direct proximity to the sample, where this approximation is justified. For an estimate of the vertical tip-sample distance, see section 8.2.

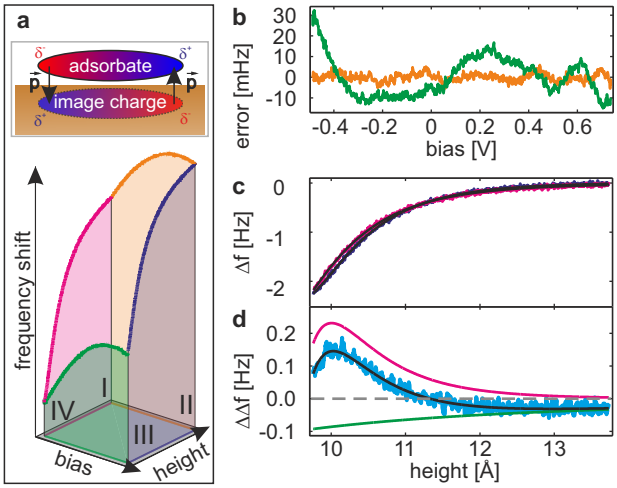

Figure 8.4: Deducing intramolecular charge distribution from $\Delta f(z)$ spectroscopy. **a** Schematic illustration of the data acquisition procedure: For each lateral grid position two KPFS parabolas at different distances (I→II and III→IV) and two Δf(z) curves at different voltages (II→III and IV→I) are recorded (see also Fig. 3.3 in section 3.4). **b** Residuals of the parabolic fit to KPFS data show just random noise for a large tip-sample spacing (orange) but systematic deviations for a short one (green). (Data points are smoothed over 75 mV.) **c** Background subtracted $\Delta f(z, V_i)$ curves along with their Lennard-Jones fits. **d** The difference spectrum $\Delta\Delta f(z, \Delta V)$ (blue) is fitted by contributions from electrostatics (green) and vertical relaxation (pink), the sum of which is shown in black (the dashed gray line indicates zero).

As the surface dipole p and the electric field right beneath the functionalized tip are both oriented perpendicular to the surface, their interaction potential equals $p\,(V - LCPD)/z$. Differentiating this expression twice yields a corresponding $\Delta f(z)$ contribution, which is proportional to $p\,(V - LCPD)/z^3$. Hence, the difference spectrum

$$\Delta\Delta f(z, \Delta V) \;=\; \Delta f(z, V_2) \;-\; \Delta f(z, V_1)$$

is expected to show two contributions: one being proportional to

$\delta z\, \Delta f'(z, V_1)$ (due to vertical relaxation δz, the pink curve in Fig. 8.4d) and a second one proportional to $p\, \Delta V / z^3$ (the green curve) indicating the presence of surface dipoles p in the junction. For details of the fitting procedure, see section A.2. Note that the functional dependencies on z of these two contributions are qualitatively different from each other and therefore allow one to discriminate between the two in a fitting procedure[3].

8.5 Simplifications and assumptions made for the determination of dipoles

The above proposed novel method and fitting procedure involve quite some simplifications and approximations.

Only a vertical relaxation in the junction has been accounted for. As the CO molecule at the tip apex is known to bend laterally under the influence of van-der-Waals attraction [103, 105, 106], it is likely that the lateral bending of the CO molecule will also depend on the electric field in the junction [113, 195] and change with bias voltage.

In our fitting procedure, we assume the vertical relaxations δz in the junction to depend on the voltage V but to be constant over the distance interval of each $\Delta f(z)$ spectrum. Obviously, as the electric field is assumed to change with distance also the vertical relaxations should. However, in the spectra the tip-sample distance is varied by 10-20 % of its average value only, while the two voltages V_i, at which the two $\Delta f(z, V_i)$ spectra are acquired, are typically above and below $V^\star$ and hence associated with fields of opposite polarity. Therefore,

[3] Changing the exponents of the Lennard-Jones fit from a (12-6)-potential to a (12-4)-potential did not affect the fit result for the dipole maps qualitatively. In addition, the dipole maps do not change much when using a Morse potential instead of a Lennard-Jones type interaction model (see section A.3).

the distance dependence of the vertical relaxation should result in a minor contribution to our fitting parameters.

In the fitting procedure polarization of the sample in the changing electric field is only taken into account in the short-range contribution of the force. For the electrostatic interaction the sample dipoles have been assumed to be static. While there will be a polarization response also in the electrostatic contribution, we again argue that this gives higher order corrections to the leading order terms. In addition, our DFT calculations of the surface with an applied electric field of $10^9\,\mathrm{V/m}$ reveal, that both molecules on the surface are polarized almost homogeneously. Thus the static polarization of the surface induced by external field will not contribute to the experimentally observed contrast.

We also did not consider charge polarization of molecules due to presence of the functionalized tip [186]. The presence of CO molecule on the tip apex significantly reduces its chemical reactivity. Therefore, the formation of a chemical bond between the tip and the inspected molecules is very unlikely [196]. Indeed, this observation is also supported by our DFT simulations when a fixed CO-tip model was approached over different sites of molecules reaching the repulsive regime. The induced charges were site independent and negligible comparing to the static polarization induced by deposition of the molecules on the Cu(111) surface. Thus we think that the charge polarization induced by the proximity of the tip does not play a significant role to the experimentally observed contrast.

Considering the above, clearly also the vertical and lateral relaxation of the CO molecule at the tip will modify the electric field at the sample surface, which also has been neglected.

Although we believe that extracting the bias-dependent vertical relaxation δz from these fits, may turn out to be useful in the future, in the current experiment we attribute any such relaxations mainly to the CO at the tip [103, 105, 106] rather than to the molecule on the

surface. We therefore disregard the relaxation δz and concentrate on the dipole maps only. We, however, would like to mention that the experimentally determined values for vertical relaxations are found to be up to 0.2 Å for the opposing fields at the two different bias voltages. We performed DFT calculations including an external electric field of approximately 10^9 V/m, which resulted in vertical relaxations of up to 0.1 Å. These calculations support that the fitted values are reasonable.

8.6 Results of the new dipole detection method

Figure 8.4 displays the experiments following the new scheme for dipole determination described above. For each point on a dense grid we recorded the frequency shift as a function of the tip-sample spacing at two different bias voltages, as is exemplary displayed for one individual grid point in a 3D representation in Fig. 8.4a. The two spectra $\Delta f(z, V_1)$ and $\Delta f(z, V_2)$ are depicted in Fig. 8.4c. Despite their similarity, the difference signal $\Delta\Delta f(z, \Delta V)$ displayed in Fig. 8.4d still shows distinct features. A comparison to the derivative $\Delta f'(z, V_1)$ (pink) shows striking agreement in the overall shape, which we view as a confirmation of the relaxation effect as described above. The offset between the experimental data and $\Delta f'(z, V_1)$ indicates clearly that another contribution is missing. An additional contribution proportional to $-\Delta V/z^3$ (green) results in a sum (black) that excellently fits the data. From this fitting procedure the surface dipole p is extracted for each grid point, rendering maps, which are henceforth called dipole maps.

To test the novel method, we compared such dipole maps to KPFS-deduced maps of $V^\star$ at distances at which KPFS works reliably. The resulting maps are displayed in Figs. 8.5a—h for PTCDA on copper, ClAnCN on NaCl bilayer on copper, along with a model of their chemical structure and a Δf image. Figures 8.5i—l show the comparison

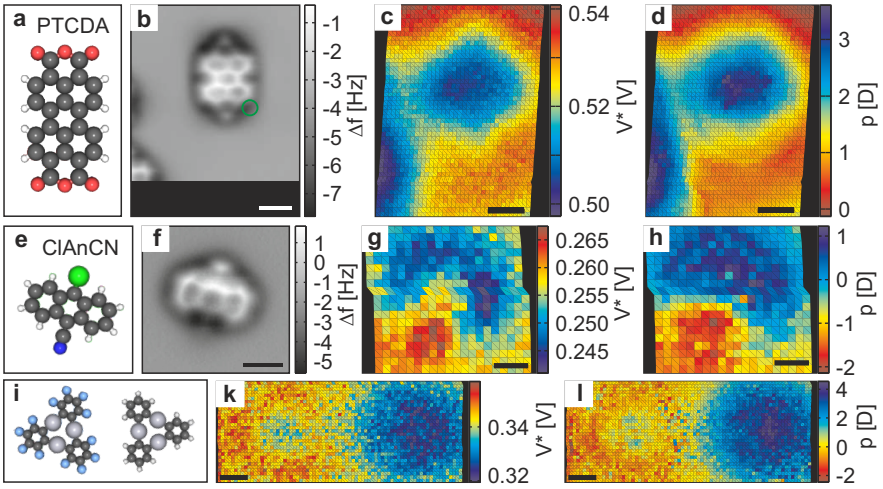

Figure 8.5: Comparison of dipole distribution maps extracted from $\Delta f(z, V_i)$ spectra (d, h, l) and conventional KPFS maps (c, g, k) at relatively large distances for PTCDA (a—d; tip heights: Δf image 9.0 Å, $V^\star$ map 12.6 Å, dipole map from 9.6 Å $\leq z \leq$ 12.6 Å and V_i = -0.4 V and 0.75 V), ClAnCN (e—h; tip heights: Δf image at 15.4 Å, $V^\star$ map at 18.2 Å, dipole map from 16.2 Å $\leq z \leq$ 18.2 Å and V_i = -0.5 V and 0.5 V), and $F_{12}C_{18}Hg_3$ and $H_{12}C_{18}Hg_3$ (i—l; tip heights: $V^\star$ map at 11.0 Å, dipole map from 9.9 Å $\leq z \leq$ 11.5 Å and V_i = -0.2 V and 0.35 V). The green marker in panel b indicates the lateral position of the spectra shown in Fig. 8.4a—d. The very good agreement between dipole and $V^\star$ maps shows that the new method is capable of reproducing KPFS results at tip-sample spacings at which KPFS works reliably.

between KPFS and the new method for $F_{12}C_{18}Hg_3$ and $H_{12}C_{18}Hg_3$ on clean copper. In the case of ClAnCN the NaCl bilayer was introduced to benchmark the method also for a distinctly different electronic coupling and current regime. In all cases the dipole maps (Figs. 8.5d, h, and l) closely resemble the $V^\star$ maps (cf. Figs. 8.5c, g, and k). In turn, in this regime $V^\star$ maps are assumed to reflect the local charge distribution [13, 14, 60].

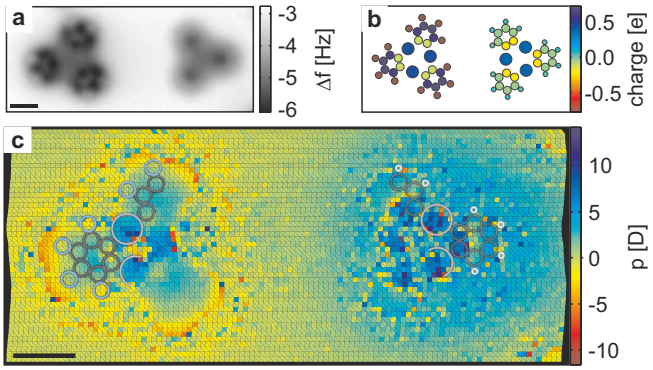

Figure 8.6: Highly resolved dipole distribution map. **a** Δf image recorded at $z = 9.6$ Å. **b** Calculated charge distribution deduced from Bader analysis. (For details, see Tab. A.1.) **c** Dipole distribution map extracted from $\Delta f(z, V_i)$ spectra for $F_{12}C_{18}Hg_3$ and $H_{12}C_{18}Hg_3$ (9.6 Å $\leq z \leq$ 10.1 Å; V_i = -0.2 V and 0.5 V). The experimental data in panel c is partially overlaid with models to indicate the position of individual atoms.

Lateral resolution and contrast increase drastically when the tip-sample spacing is reduced. A corresponding dipole map for $F_{12}C_{18}Hg_3$ and $H_{12}C_{18}Hg_3$ on copper is displayed in Fig. 8.6, along with a Δf image and the DFT calculated charge distribution for comparison. Note that the dipole maps are expected to be a convolution of the local dipoles with the lateral profile of the electric field beneath the tip [197], smearing out the apparent dipole distribution. Remarkably, this map still shows pronounced intramolecular contrast without suffering from similar artifacts as the KPFS-derived map shown in Fig. 8.2h. Interestingly, at the positions of the mercury atoms, the contrast in this map is much stronger than in the Δf images (cf. Figs. 8.2c and 8.6a).

The charge distribution map shows a contrast that is in agreement with the calculated charge distribution (see Fig. 8.6b and Tab. A.1). The contrast observed at the circumference of the molecules fits to the overall surface dipole as discussed above. Directly along the

C-F bonds a strong contrast change from green to red indicates the electrons being pulled toward the fluorine ($C^{\delta+}$–$F^{\delta-}$). The C-H bonds show much less of a polar nature, with a tendency toward $C^{\delta-}$–$H^{\delta+}$ in accordance with the Bader charge analysis (see Fig. 8.6b). The map also reveals that the mercury atoms on both molecules apparently carry net positive charge, in good agreement with DFT. The signal on benzene rings shows relatively weak contrast with respect to Hg atoms, in fair agreement with the calculations.

To get insight into the robustness of our new method against changing the interaction potential for the fitting procedure, we also used a Morse potential to deduce dipole distribution maps. It turned out that the resulting maps of intramolecular dipoles do not strongly depend on the interaction potential (for details and a comparison of results for the two different potentials, see section A.3 in the appendix.)

It needs to be emphasized that the dipole maps—even though provided in units of Debye—may not be taken as being quantitative. Experimental uncertainties in determining the absolute tip-sample distance, averaging effects, the bending of the CO molecule at the tip apex, the approximations made in the fitting procedure, and tip-induced surface dipoles may influence the quantitative interpretation. Nonetheless, we are convinced that this novel technique presents a route to better disentangle electrostatic from nonelectrostatic contributions to overcome the limitations of KPFS at closest distances and highest resolution. It may even be a first step toward a quantitative determination of surface dipoles.

8.7 Conclusion

The experiments presented here provide insight as to why KPFS systematically fails to reproduce the $LPCD$ at very close tip-sample distances. We identify bias-dependent short range interactions between

the tip and a molecule adsorbed on a surface as one reason for the failure of KPFS at very small tip-sample spacings. We introduce and benchmark a new AFM-based spectroscopy method that allows for resolving intramolecular charge distributions with unprecedented resolution, showing contrast at the atomic scale.

9 Local tunneling decay length and KPFS

Most of the work presented in this chapter has been published in Physical Review B[1]. Parts of the text are identical to the publication.

The last chapter presented a new AFM-based method for the determination of intramolecular charge distributions. Since the tunneling current is sensitive to the potential barrier between tip and sample, STM is, in principle, also capable of deducing the sample's work function qualitatively. The new spectroscopy scheme introduced in the last chapter also allows for a direct comparison of AFM- and STM-derived surface potential. Hence, we can directly compare the results deduced from the two different methods.

9.1 STM-based charge determination

Since the early days of scanning tunneling microscopy, current-distance ($I(z)$) spectroscopy has been applied to determine variations of the work function at surfaces [15, 17]. In the one-dimensional description of quantum tunneling through a rectangular barrier, the transmission probability decays exponentially with the barrier's thickness, with the decay length being inversely proportional to the root of the

[1] F. Albrecht, M. Fleischmann, M. Scheer, L. Gross, and J. Repp. 'Local tunneling decay length and Kelvin probe force spectroscopy'. In: *Phys. Rev. B* 92 (2015), 235443.

barrier height [16]. Consequently, one expects that from the decay length determined from current-distance spectra the barrier height can be extracted, which—in simplest approximation—is the mean of the work function of the tip and the sample. It has been early realized that several corrections are needed, because of the tunneling junction being three-dimensional in nature [198–200], the applied bias voltage [201–203] or image charge effects [204] altering the barrier's shape, for example. In this context, a so-called effective barrier height has been introduced, to still make use of the simple description. But despite such corrections, one still may expect a well-defined and monotonic relationship between the inverse of the decay length and the local work function of the sample for a given tip.

For extended, homogeneous samples, the above described relationship seems to hold and the decay length is assumed to provide at least some qualitative trends of the surface contact potential [199, 205, 206]. However, for strongly corrugated samples, from very basic arguments one can show that the geometry will affect $I(z)$ spectra [199, 207, 208] even if the work function is assumed to be constant over the sample, as will be discussed further below. In the past, maps of the current-distance decay constant on molecular and sub-molecular length scales have been extracted and interpreted in various aspects [159, 209–213]. However, it has never been rigorously tested, as to whether the current-distance decay length carries reliable information of local surface dipoles or variations of the contact potential on the very local scale.

Another STM-derived technique, which can be used to detect variations of the contact potential difference, is based on measuring field emission resonances [214, 215]. However, this is not expected to work at a (sub)-nanometer length scale, since the lateral confinement would affect the energies of the resonances [214].

Apart from the above-mentioned possible geometry-related artifacts, there are quite a few other problems associated with extracting effec-

tive barrier heights from $I(z)$ spectra. At the technical side, a finite impedance of the bias voltage supply or the current preamplifier input may affect the apparent decay length [216], for example. As rather fundamental issues we would like to mention mechanical deformations of the tip-sample junctions close to the contact point [216–218] and band bending effects in a semiconductor sample, the latter resulting in a complete failure of this technique [219]. These issues are, however, not subject of our study.

9.2 Experimental methods

We benchmark maps of tunneling decay length derived from $I(z)$ spectra against KPFS-derived $V^\star$ maps for test cases that show tunneling current variations on the very local scale. As long as the tip is far enough from the sample and not entering the regime of Pauli repulsion (see reference [14] and chapter 8), KPFS [12] is an established technique to reliably extract variations of the contact potential on the very local scale [13, 59, 66, 186–188, 220–222]. As our new spectroscopy scheme combines $I(z)$ with KPFS in one single spectrum (see Fig. 3.3b), the benchmarking can be done under identical conditions of the tip-sample junction.

We investigated $F_{12}C_{18}Hg_3$ [190], $H_{12}C_{18}Hg_3$ [191], and PTCDA with the molecules directly adsorbed on Cu(111), whereas we studied ClAnCN on a double layer of NaCl on Cu(111). All these molecules and Au atoms were deposited onto the cold sample ($T < 15\,\mathrm{K}$) with the sample being located inside the STM/AFM. Except for the data on the Au adatoms on NaCl, the tip was functionalized with a CO molecule [6, 13]. All KPFS data were obtained at a 0.5 Å oscillation amplitude. During the acquisition of an entire data set providing a map of $V^\star$ and current decay length, the feedback loop was switched off. Specifically, also while moving the tip from one to another of the

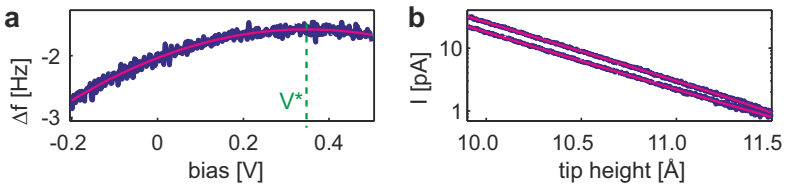

Figure 9.1: Exemplary curves of KPFS and $I(z)$ measurements. **a** KPFS parabola: raw data (blue) along with parabolic fit (red). The maximum position of the parabola gives the $V^\star$ value (green). **b** Logarithmic plot of $I(z)$ curves at different bias voltages: raw data (blue) along with exponential fits (red).

grid points, the feedback loop was never switched on. This is important to ensure that local variations of the tunneling current cannot influence the spectra indirectly via vertical displacements of the tip. The tip-sample spacing for experiments with metallic tips refers to the distance of the tip being at point-contact with the sample. For experiments with CO functionalized tips the tip-sample spacing is deduced from characteristic AFM contrast (see section 8.2).

We acquired KPFS maps of $V^\star$ along with maps of the inverse current decay length κ. To this end, for each lateral position on a dense grid a KPFS parabola $\Delta f(V)$ at a safe distance to avoid artifacts (see chapter 8) and two $I(z)$ curves at different voltages are recorded immediately one after another. Figure 9.1 shows exemplarily a set of these curves. Each of the $\Delta f(V)$ and $I(z)$ spectra is fitted to a parabola $\Delta f(V) = \Delta f^\star + a(V - V^\star)^2$ and an exponential decay $I(z) = I_0 \cdot \exp(-2\kappa z)$, respectively. Out of the fitting parameters $\Delta f^\star, a, V^\star, I_0$, and κ, relevant in the present context are the voltage of compensated local contact potential difference $V^\star$ and the inverse of the current decay length 2κ.

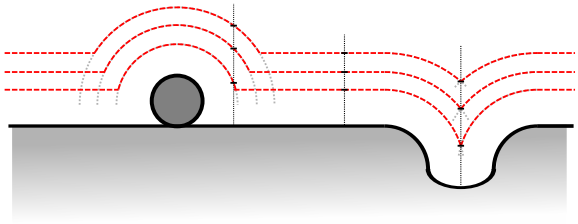

Figure 9.2: Illustration how the local topography can influence the apparent tunneling current decay length. If one assumes that profiles of constant current (dashed lines) follow the topography at different distances, beside protrusions and in trenches the line contours will become more sparse as compared to the flat terraces (see vertical dotted lines).

9.3 Effect of sample topography on decay length

In the following we will discuss, how a strong corrugation of a sample topography with a homogeneous contact potential may affect the decay length in $I(z)$ spectra. To exemplify that, we assume to have a fictitious local corrugation of the sample that should have a completely homogeneous contact potential, that is, for this thought experiment we disregard the Smoluchowski effect [61]. The larger the average tip-sample distance, the more any local corrugation of the sample will become laterally washed out in STM images for simple geometric reasons. Figure. 9.2 schematically depicts this situation by showing line profiles of constant current for different setpoint values as a cross section through the sample. In a very simple picture, one may assume that the constant-current isosurfaces around an adatom are concentric spheres around it. Hence, with decreasing current setpoint, the radius of the respective sphere increases and thus also the lateral extent of the protrusion in the image.

From this simple geometric effect described above it follows that the line contours will become more sparse just next to a local corrugation of the sample, resulting in an apparent increase of the current decay

length [199, 207, 208], even though in this thought experiment the contact potential was homogeneous. Analogous arguments apply for step edges and sharp trenches.

9.4 Choice of Systems

After considering the above, one wants to benchmark κ mapping for cases, in which the constant-current profiles show local corrugation and the local contact potential is expected to vary over the sample. Here we chose several distinctly different test cases, which are briefly introduced in the following. As almost point-like surface dipoles altering the local contact potential we investigated individual Au adatoms on top of a bilayer of NaCl on Cu(111). These are associated with a protrusion in constant-current topography images with a large apparent height. They can be deliberately charged negatively [176], giving rise to a change in the KPFS signal [66].

Further, we used several molecular systems for benchmarking, the KPFS data of which are presented in chapter 8. One of these molecular systems is PTCDA adsorbed on Cu(111), which is known to reduce the work function of Cu(111) [223, 224]. Due to the charge transfer inside the molecule [225] as well as between the substrate and the molecule, this molecule represents an overall surface dipole rather delocalized over the entire molecule. A different situation arises for ClAnCN molecules, in which the chlorine and the carbonitirile moieties carry different partial charge giving rise to an in-plane dipole of the molecule. This molecule was studied on top of a NaCl bilayer to also test a distinctly different current regime. Finally, we investigated $F_{12}C_{18}Hg_3$ and its hydrogen-terminated counterpart $H_{12}C_{18}Hg_3$. This direct comparison of molecules with fluorine versus hydrogen termination enables having different surface dipoles and local contact potentials while keeping an almost identical geometry. On top, these molecules exhibit pronounced and rather sharp trenches in their

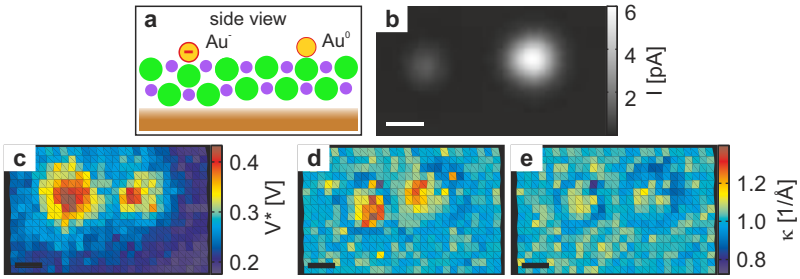

Figure 9.3: Individual neutral and negatively charged Au adatoms on bilayer NaCl/Cu(111) examined with a metal tip. **a** Schematic side view of the adsorption geometry and charge distribution **b** Current image of gold-anion (left hand side) and neutral gold adatom (right hand side) ($z = 12.5\,\text{Å}$, $V = 0.1\,\text{V}$). **c** $V^\star$ map recorded at a height of $12.5\,\text{Å}$. **d** and **e** κ maps deduced from $I(z)$ curves for $12.5\,\text{Å} \leq z \leq 15.5\,\text{Å}$ at $V = -0.5\,\text{V}$ and $V = 0.5\,\text{V}$ for panels d and e, respectively. The color scale is the same for both maps. (Scale bars 5 Å.)

constant-current profile directly inside the molecule. This renders this an appropriate test case for artifacts arising from sharp features in constant-current profiles as they are discussed in the previous section.

9.5 Experimental results of κ mapping and KPFS

We start with the discussion of deliberately charged individual Au adatoms on a bilayer of NaCl on a Cu(111) surface [176]. The corresponding data were recorded with a metal tip. To examine the effect of a localized charge we investigated two adatoms next to each other, where one of them was prepared in the anionic state [176], as depicted in a cross sectional drawing in Fig 9.3a. The appearance of the two species in STM images (Fig 9.3b) is different in accordance with previous results [66, 176]. The $V^\star$ map (Fig 9.3c) shows a significant increase of $V^\star$ above the anion as is expected and reported before [66].

Interestingly, the $V^\star$ values are also increased above the neutral Au atom, which we ascribe to a weak but slightly polar bond between the Au adatom and the Cl ion below or to polarization effects. However, the feature of increased $V^\star$ is distinctly smaller in the lateral direction in the case of the neutral Au atom as compared to the anion. In κ maps, see Figs. 9.3d and e, the two species are indistinguishable from each other within the noise floor of the experiment. The κ maps acquired at negative and positive bias voltages of 0.5 V show a clear difference with respect to each other and with respect to the $V^\star$ map. In particular the κ map acquired at positive bias voltage, displayed in Fig. 9.3e, exhibits rings of decreased κ around the adsorbates as primary features. These features are exactly what can be expected from simple geometry considerations as artifacts; see above (Fig. 9.2). Also the diameters of these rings in the κ map correspond to the lateral sizes of gold adatoms in the tunneling current image (Fig. 9.3b), supporting the assignment as topographic artifacts.

Next we turn to PTCDA on clean Cu(111) and ClAnCN on bilayer NaCl on Cu(111), the data sets of which were recorded with CO functionalized tips. The structures of those molecules are depicted in Figs. 9.4a and 9.5a, respectively. For the assignment of the different side groups in ClAnCN from AFM data, see section A.1. Figs. 9.4b and 9.5b show constant-height STM images of PTCDA and ClAnCN, respectively. As is discussed above, for PTCDA on copper, one expects an overall surface dipole distributed over the entire molecule, arising from the interaction between the molecule and the substrate [223, 224]. The dipole is expected to reduce the $V^\star$ above the position of the molecule. Figure 9.4c showing the $V^\star$ map is in very good agreement to that. In contrast, the κ map recorded at negative bias (Fig. 9.4d) shows even an increase of κ values above the molecule, which would indicate an increase of the work function. The κ map recorded at positive bias also shows increased values above the molecule, although much less pronounced. Here, a halo of κ-values decreased with respect to the substrate around the molecule becomes apparent — as

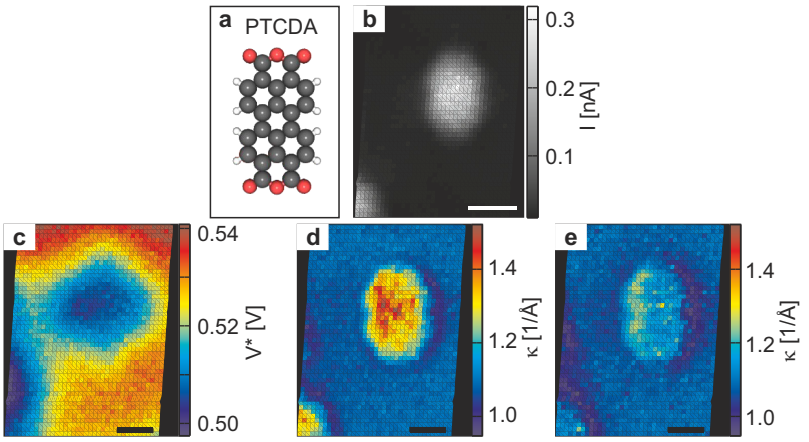

Figure 9.4: PTCDA on clean Cu(111) investigated with CO functionalized tip. **a** Structure model of PTCDA. **b** Constant-height image of tunneling current extracted from grid data at a tip height of $9.6\,\text{Å}$ and $0.1\,\text{V}$ bias voltage. **c** $V^\star$ map recorded at $12.6\,\text{Å}$. **d** and **e** κ maps extracted from $I(z)$ curves for $9.6\,\text{Å} \leq z \leq 12.6\,\text{Å}$ at $V = -0.4\,\text{V}$ and $V = 0.75\,\text{V}$ for panels d and e, respectively. (Scale bars 5 Å.)

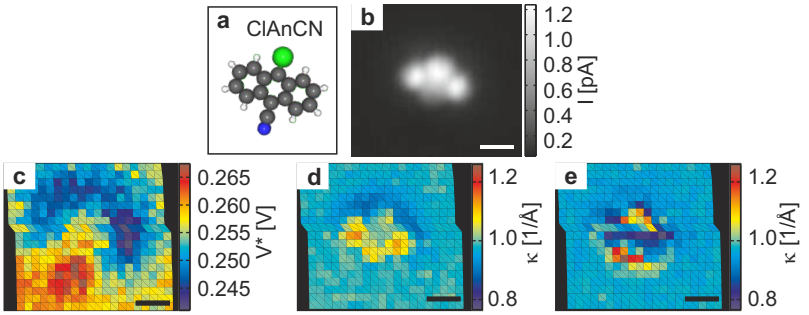

Figure 9.5: ClAnCN on bilayer NaCl/Cu(111) investigated with CO functionalized tip. **a** Structure model of ClAnCN. **b** Constant-height image of tunneling current recorded at a tip height of $15.8\,\text{Å}$ and $0.1\,\text{V}$ bias voltage. **c** $V^\star$ map recorded at $18.2\,\text{Å}$. **d** and **e** κ maps extracted from $I(z)$ curves for $16.2\,\text{Å} \leq z \leq 18.2\,\text{Å}$ at $V = -0.5\,\text{V}$ and $V = 0.5\,\text{V}$ for panels d and e, respectively. (Scale bars 5 Å.)

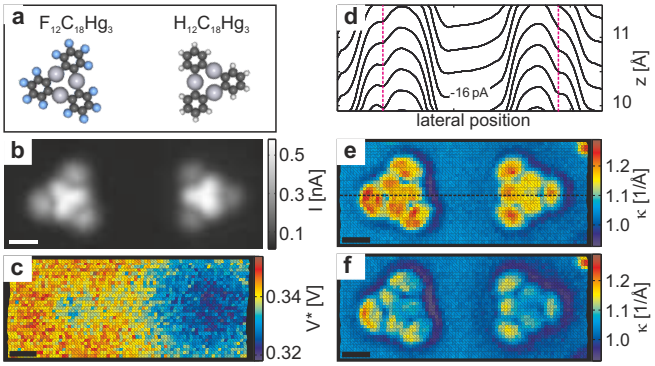

Figure 9.6: $F_{12}C_{18}Hg_3$ and $H_{12}C_{18}Hg_3$ on clean Cu(111) examined with a CO functionalized tip. **a** Structure models of $F_{12}C_{18}Hg_3$ (left hand side) and $H_{12}C_{18}Hg_3$ (right hand side) shown in the same orientation as the molecules under investigation. **b** Constant-height image of tunneling current of the two molecules ($z = 9.6\,\text{Å}$, $V = 0.1\,\text{V}$). **c** $V^\star$ map recorded at $z = 12.0\,\text{Å}$. **d** Side view onto constant-current line profiles across $F_{12}C_{18}Hg_3$ and $H_{12}C_{18}Hg_3$ molecules. The profiles were acquired along the line indicated in panel e at $V = -0.2\,\text{V}$. When going from one constant-current profile to the adjacent one, the current changes by a factor of 2. The two dashed red lines highlight positions of trenches in the corresponding constant-height image. **e** and **f** κ maps extracted from $I(z)$ curves for $9.9\,\text{Å} \leq z \leq 11.5\,\text{Å}$ at $V = -0.2\,\text{V}$ and $V = 0.35\,\text{V}$ for panels e and f, respectively. (Scale bars 5 Å.)

in the case of gold adatoms. For the ClAnCN molecule the $V^\star$ map (Fig. 9.5c) shows a reduction in the work function above the position of the chlorine atom and an increase above the carbonitrile group. The κ map recorded at negative bias voltage (Fig. 9.5d) shows contrast in rough agreement with the $V^\star$ map; however, yet again the κ maps acquired at negative and positive (Fig. 9.5e) bias voltages are quite different.

Finally, the results obtained on the two organometallic molecules $F_{12}C_{18}Hg_3$ and $H_{12}C_{18}Hg_3$ are presented in Fig. 9.6, starting with their structure shown in panel a. Figure 9.6b shows the constant-

height STM image of the two molecules investigated right next to each other in the same data set with the same tip. Important for the discussion of the κ maps is the observation that the STM images are very similar for the two cases and that the STM images of both molecules exhibit distinct trenches. The $V^\star$ map (Fig. 9.6c) shows the expected effects arising from the polar bonds in those molecules (see chapter 8). As for all other cases discussed here, the κ maps acquired at negative (Fig. 9.6e) and positive (Fig. 9.6f) bias voltages are quite different. Note that the bias voltages of $V = -0.2\,\mathrm{V}$ and $V = 0.35\,\mathrm{V}$ are still moderate and that no pronounced molecular resonances occur between those two values. Similar to the case of gold adatoms, the two different species cannot be assigned from their κ maps and the differences of one molecule between different bias voltages are more significant than the differences of the two different species at a particular bias voltage. A more detailed inspection of the κ maps reveals that they carry a large resemblance to the STM image. At the position of the trenches in the STM image, lines of reduced κ occur, exactly as the artifacts expected from simple geometry considerations; see above. To illustrate that, Fig. 9.6d shows experimental line profiles of constant current across the two molecules (along the dashed line in Fig. 9.6e). One can clearly see, how the dip in these line profiles becomes more and more washed out for profiles of smaller currents. This directly shows the effect discussed in section 9.3.

9.6 Quantitative failure of κ mapping

In all cases shown, κ maps do not match KPFS results even qualitatively. One may speculate that a comparison with theory that takes all details into account could still render a quantitative comparison possible. In the following discussion, we therefore comment on the quantitative aspects exemplified for the data along the dashed line in Fig. 9.6e: Calculating the apparent barrier height ϕ_b from κ after [16]

$\kappa = \sqrt{2m_e\phi_b}/\hbar$ — with m_e being the electron mass and $\hbar$ the reduced Planck constant — results in a variation of the apparent mean barrier height of 2.5 eV. Under the assumption that the mean barrier height is similarly affected by the tip and sample work functions, this would correspond to a variation of about 5 eV of the work function at the sample surface. This value is comparable to the work function of the Cu(111) surface itself and hence out of range. One may expect the applied bias voltage to affect the mean barrier height globally, that is, everywhere on the sample. However, the experimentally observed bias dependency of κ values does not follow this reasoning: Whereas κ values are (almost) bias independent on the substrate, they strongly depend on the applied bias voltage at the positions of molecules and adatoms. Interestingly, the change in apparent barrier height at positions of $F_{12}C_{18}Hg_3$ and $H_{12}C_{18}Hg_3$ (≈ 0.7 eV) roughly equals the change in the applied bias voltage (0.55 V). We observe a similar trend for the PTCDA molecule. The simple interpretation of κ values in terms of the work function would imply that the applied bias voltage strongly affects the work functions of the sample, which is not straightforward. We note that a quantitative comparison of experimental κ values with theory calculations may be very difficult since theory would have to quantitatively reproduce artifacts in the 5 eV range to reveal physical changes that are expected in the sub-eV range.

We further note, that the ranges of applicability of κ mapping and KPFS are also quite different: KPFS runs into problems at very close tip-sample spacings (see reference [14] and chapter 8), but it was shown to reproduces the electric field of the sample at distances from typical STM imaging setpoints on [13]. For larger distances, the resolution may be limited, but there is no fundamental limit of applicability towards larger distances. On the contrary, the κ maps presented in this work did not reproduce KPFS results even in a regime of typical STM setpoints. Performing κ mapping at only a few Ångstroms larger tip sample spacings is impossible due to the tunneling current becoming

too small to be detected.

Although we demonstrated that $I(z)$ spectroscopy is not suited to measure the contact potential on the atomic scale, it might be very useful. Obviously it contains information that is complementary to KPFS. $I(z)$ measurements in combination with STS and KPFS might obtain other electronic properties of adatoms or molecules, e.g., their polarizability or the decay of orbital densities.

9.7 Conclusion

After investigating different examples of adsorbates with local variations of the contact potential difference and the STM images, we conclude the following: (i) κ maps strongly depend on the particular bias voltage at which they are acquired. (ii) κ maps do not reflect even qualitatively the $V^\star$ maps acquired by means of KPFS; even contrary results are possible. (iii) Even clear-cut cases of charged versus neutral atoms and molecules with strong polar bonds cannot be assigned from κ measurements. (iv) The artifacts expected from simple geometry considerations are clearly visible in locally resolved κ maps, and are often the dominating feature. We hence conclude that κ measurements must not be directly interpreted in terms of surface dipoles or local variations of the work function on sub-molecular length scales.

10 Summary and Outlook

The results presented in this thesis enlarge the toolbox of SPM and widen the applicability of combined STM and AFM. They increase the amount of possible reaction schemes to be investigated in detail in on-surface chemistry. The findings of this thesis can be grouped in three main topics:

Geometric structure determination — going 3D
The main improvement in this field is the possibility to investigate molecular structures not only planar and adsorbed not only parallel to the sample surface:

In chapter 5 we recorded full 3D data sets for chemical structure determination of the helical DPAT molecule. Even though the acquisition of such 3D data sets is time consuming, they provided plenty of structural details, such as apparent out-of-surface tilt angles of individual carbon rings in the adsorbed molecule to 5° accuracy.

For symmetric molecules like 2H-TPP and Cu-TPP investigated in chapter 6, imaging in planes perpendicular to the sample surface allows for a quick data acquisition. These vertical images made the direct characterization of faint conformational details possible in real space. These details, which were not accessible in conventional imaging modes, were decisive to unambiguously distinguish 2H-TPP from Cu-TPP molecules.

Vertical imaging also enabled the quantitative characterization of the vertical movement of the central copper ion in Cu-TPP upon tip-induced conformational switching.

On-surface chemical reactions — detailed characterization of reactant and product

The capabilities of structure determination allow to deduce a richness of detail in on-surface chemistry experiments — many of them not accessible in wet chemistry:

In chapters 5 and 7 we examined molecules before and after a reaction with atomic precision. In chapter 7, we induced a metal-organic complex formation reaction with the SPM tip, such that the electronic as well as the geometric structure of the same molecule could be fully characterized before and after the reaction. This enables maximum control over the reactant and the reaction conditions.

The observed energetic positions and shapes of molecular and complex's orbitals were rationalized from the linear combination of orbitals method.

In chapter 5 we identified a potential three-step reaction pathway from atomically resolved AFM images of molecules before and after a thermally activated planarization reaction. This pathway includes an almost 180° out-of-plane rotation of one half of the molecule, that has been observed for the first time in an on-surface chemical reaction with SPM.

At step edges we observed a different reaction product as compared to terraces, which is explained by the locally increased reactivity at substrate defects.

Intramolecular charge distribution — resolving polar bonds
Intramolecular charge distributions are among the driving forces in many fields.

In chapter 9 we benchmarked STM-based work function determination against KPFS on the sub-molecular length scale for different example cases. The experiments were performed in a distance regime where KFPS works reliably.

Apparently, the STM-derived κ data did not correspond to the AFM-derived KPFS results. The κ data turned out to be dominated by geometric artifacts and must not be directly interpreted in terms of the sample's work function or dipole distribution. This settles a long-standing controversy about the interpretation of such κ data.

In chapter 8 we identified bias dependent vertical relaxations in the tip-sample junction as one important reason why KPFS fails to deduce the charge distribution at very close tip-sample distances. These relaxations are of general nature and not specific for the studied systems.

We used the dependence of the electric field on the tip-sample distance to introduce a novel AFM-based spectroscopy scheme. We successfully tested this novel method with KPFS in the distance regime where KPFS shows no artifacts. Moreover, it makes reliable data acquisition at smallest tip-sample spacing possible and we were able to resolve charge-related contrast along single polar bonds.

Outlook

The combination of these results may pave the way for an even deeper insight into the details of chemical reactions in the future — such as characterizing chemical reaction intermediates in single molecular reactions induced by the SPM tip.

To further increase the richness of detail deduced from SPM experiments, additional signal channels can be employed in the experiment. Recently, the damping signal of the AFM cantilever was used to perform Kelvin probe force microscopy experiments [226, 227]. Deriving the same physical quantity from two independent signal channels may further improve the interpretation of KPFS results.

The results presented in this thesis were at the limit of spatial resolution in SPM. However, all experiments were very slow and hence there was no temporal resolution. Employing a pump-probe scheme, temporal resolution from single microseconds [228] to picoseconds [229] was achieved in AFM setups recently. In combination with ultra-fast THz-pulses [230, 231], SPM may be able to directly deduce the charge carrier dynamics in single molecules with femtosecond temporal resolution in real space.

A Additional data for the investigation of bond polarity

A.1 Assignment of side groups in ClAnCN

Figure A.1 shows the identification of side groups in ClAnCN: To assign the chlorine atom and the carbonitrile group in ClAnCN, we acquired an AFM data set on 9,10-anthracenedicarbonitrile, from which the carbonitrile group could be clearly recognized.

A.2 Details of fitting procedure

To fit $\Delta f(z, V_i)$ (after background subtraction) in the case of the dipole maps, we use a Lennard-Jones model for the short range interaction potential U:

$$U = -U_0 \left(\frac{z_0^{12}}{(z - z_{\text{off}})^{12}} - 2 \frac{z_0^6}{(z - z_{\text{off}})^6} \right)$$

where U_0 denotes the minimum of the interaction potential, z_0 the equilibrium distance, and z_{off} an offset in the tip sample distance. This offset accounts for the difference between the tip-substrate spacing z and the distance between the CO of the functionalized tip and the molecule on the sample. Since the AFM oscillation amplitude was

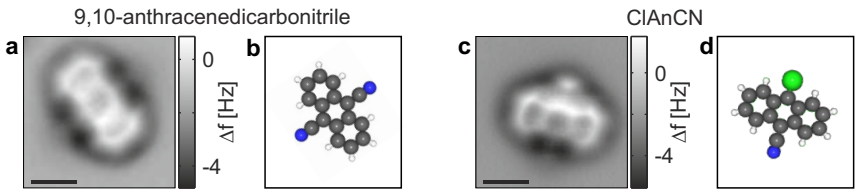

Figure A.1: Assignment of side groups in ClAnCN: **a** Constant-height Δf image of 9,10-anthracenedicarbonitrile adsorbed on bilayer NaCl. ($\Delta z = 0.4\,\text{Å}$ from the STM SP of 2 pA at 0.5 V) **b** Ball model of 9,10-anthracenedicarbonitrile oriented like in the experiment. **c** Constant-height Δf image of ClAnCN adsorbed on bilayer NaCl. ($\Delta z = 1.45\,\text{Å}$ from the STM SP of 2 pA at 0.1 V) **d** Ball model of ClAnCN oriented like in the experiment. The positions of the chlorine atom and the carbonitirle group were assigned from the comparison with experimental data depicted in panel a. (Scale bars 5 Å.)

only 0.5 Å, we approximate the Δf signal as the stiffness of the tip-sample interaction [35]:

$$\begin{aligned}\Delta f(z)_{\mathrm{LJ}} &= \frac{f_0}{2k_0}\frac{\partial^2}{\partial z^2}U \\ &= -\frac{f_0}{2k_0}U_0\left(156\,\frac{z_0^{12}}{(z-z_{\mathrm{off}})^{14}} - 84\,\frac{z_0^{6}}{(z-z_{\mathrm{off}})^{8}}\right)\end{aligned}$$

Where f_0 denotes the resonance frequency and k_0 the stiffness of the cantilever without tip sample interaction.

To obtain the parameters U_0, z_0 and z_{off} at each individual pixel of the grid, this equation is fitted to the $\Delta f(z, V_1)$ curve after background subtraction. As discussed in section 8.4, the difference of two $\Delta f(z, V_i)$ curves at different bias voltages V_i consists of two parts: An electrostatic contribution approximately proportional to $p\,\Delta V/z^3$ and a contribution stemming from vertical relaxations δz. The latter is proportional to the derivative of $\Delta f(z)_{\mathrm{LJ}}$ with respect to the tip-sample spacing z. Hence, we fit the difference of two $\Delta f(z, V_i)$ curves

recorded at different bias voltages to

$$\begin{aligned}\Delta\Delta f(z,\Delta V) &= \Delta f(z,V_2) - \Delta f(z,V_1) \\ &= \frac{f_0}{2k_0}\left\{p\frac{2\Delta V}{z^3} + \delta z\, U_0\left(\frac{2184\, z_0^{12}}{(z-z_{\mathrm{off}})^{15}} - \frac{672\, z_0^6}{(z-z_{\mathrm{off}})^9}\right)\right\}\end{aligned}$$

Using the previously determined parameters U_0, z_0, and z_{off}, this fit yields the dipole p and the vertical relaxations within the junction δz.

A.3 Full set of dipole maps deduced using different interaction potentials

To investigate the influence of different interaction potentials used in the fitting procedure we fit one of the $\Delta f(z,V_i)$ curves to the second derivative of a Morse potential:

$$U_{\mathrm{M}} = -U_{0,\mathrm{M}}\left(1 - e^{-a\left(z-z_{\mathrm{off}}\right)}\right)^2$$

Here, $U_{0,\mathrm{M}}$ denotes the minimum of the interaction potential, a its width and z_{off} is the position of the potential minimum relative to the general offset in the z-scale. In analogy to the procedure presented in section A.2 we obtain as a fit parameter the dipole and vertical relaxations by fitting $\Delta\Delta f(z,\Delta V)$. Figure A.2 shows dipole maps for all molecules under investigation from the fitting using a Lennard-Jones type (left column) and a Morse potential (right column) for the nonelectrostatic tip sample interactions. Despite small variations in the contrast of individual maps (e.g. Figs. A.2i and k), the dipole maps show no strong dependence of the interaction potential used for the fit. This shows how robust the results are with respect to different fitting functions.

Figures A.2e—m show the full set of dipole maps recorded on $F_{12}C_{18}Hg_3$ and $H_{12}C_{18}Hg_3$ molecules. The map depicted in panel

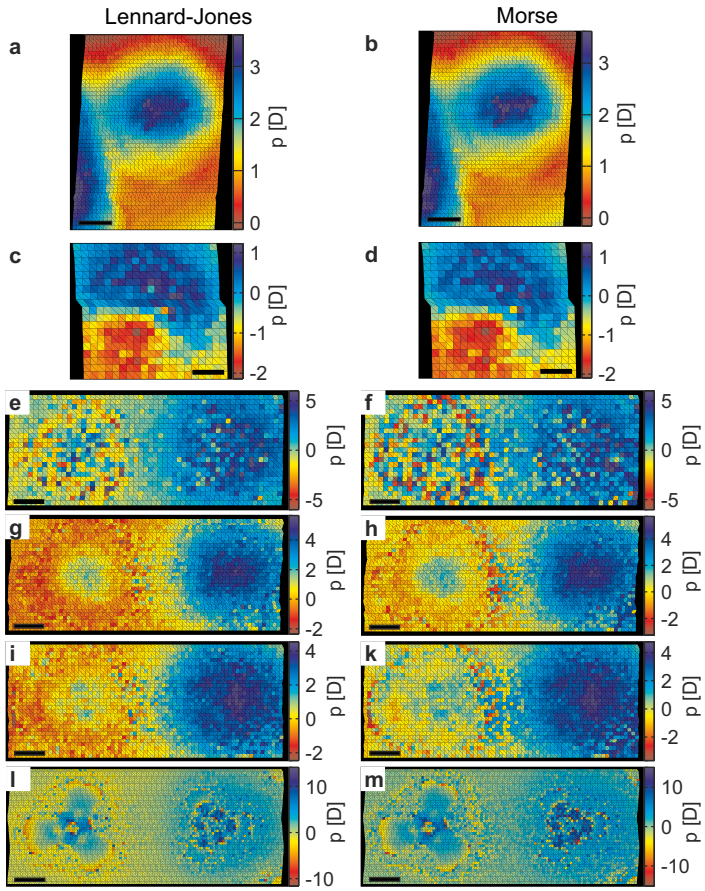

Figure A.2: Full set of dipole maps deduced from the new method for Lennard-Jones type (left column) and Morse potential (right column): **a** and **b** Dipole maps for PTCDA on clean copper: 12.6 Å $\leq z \leq$ 9.6 Å; V_i = -0.4 V and 0.75 V. **c** and **d** Dipole maps for ClAnCN on bilayer NaCl on copper: 18.2 Å $\leq z \leq$ 16.2 Å; V_i = -0.5 V and 0.5 V. **e—m** Dipole maps for $F_{12}C_{18}Hg_3$ and $H_{12}C_{18}Hg_3$ on clean copper: **e** and **f** 11.0 Å $\leq z \leq$ 10.5 Å; V_i = -0.2 V and 0.3 V. **g** and **h** 12.0 Å $\leq z \leq$ 9.8 Å; V_i = 0.0 V and 0.5 V. **i** and **k** 11.5 Å $\leq z \leq$ 9.9 Å; V_i = -0.2 V and 0.35 V. **l** and **m** 10.1 Å $\leq z \leq$ 9.6 Å; V_i = -0.2 V and 0.5 V. (Scale bars 5 Å.)

e was recorded relatively far from the surface and the variation in tip height was quite small. Therefore, this map appears quite noisy. However, it reproduces the contrast of $V^\star$ maps at the corresponding tip height (cf. Figs. 8.3c—d) quite well. Data presented in Figs. A.2g and i was recorded at similar range of tip sample spacings. Fig. A.2g was recorded with one of the two $\Delta f(z, V_i)$ curves at zero applied bias. The observation that both maps show similar contrast provides further support, that phantom force [68] can be ruled out as main contribution to our signal.

Whereas the z-ramps for Fig. A.2g were recorded at voltages symmetric around $V^\star$, the data for Fig. A.2i was recorded at two bias voltages being both more negative than $V^\star$. This confirms that the analysis is robust against shifting the bias voltages with respect to $V^\star$.

When going even closer towards the sample, the lateral resolution and contrast increase, as depicted in Fig. A.2l.

A.4 DFT-calculated charge distribution of $F_{12}C_{18}Hg_3$ and $H_{12}C_{18}Hg_3$

The adsorption geometry and charge distribution of $F_{12}C_{18}Hg_3$ and $H_{12}C_{18}Hg_3$ molecules on Cu(111) were calculated using the plane-wave density-functional-theory code VASP [192]. Vanderbilt ultrasoft pseudopotentials [232] were used. The exchange-correlation functional was described within the PW91 generalized gradient approximation [233]. The copper surface was represented by a 3-layer 8×8 Cu(111) slab. The one atomic layer at the bottom of the Cu slab was kept fixed during the geometry optimization. Only the Γ point of the supercell Brillouin zone was considered in the calculations.

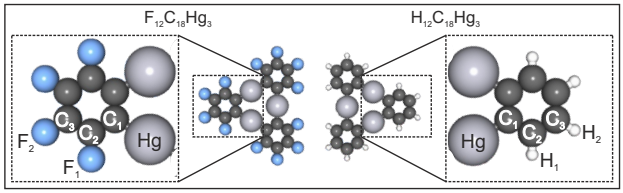

Figure A.3: Labeling of characteristic atoms in $F_{12}C_{18}Hg_3$ and $H_{12}C_{18}Hg_3$ molecules for calculated charges presented in Tab. A.1.

Table A.1: DFT-calculated charges using Bader analysis [234] for different atoms of $F_{12}C_{18}Hg_3$ (left part) and $H_{12}C_{18}Hg_3$ (right part) molecules in gas phase (Q_{gas}) and adsorbed on the Cu(111) surface (Q_{surf}). Positions of the characteristic atoms are marked in Fig. A.3.

Atom	Q_{gas}	Q_{surf}	Atom	Q_{gas}	Q_{surf}
Hg	0.559	0.449	Hg	0.447	0.384
C_1	-0.135	-0.114	C_1	-0.179	-0.227
C_2	0.662	0.621	C_2	-0.072	-0.031
C_3	0.715	0.727	C_3	-0.028	-0.037
F_1	-0.767	-0.773	H_1	0.014	0.036
F_2	-0.755	-0.763	H_2	0.027	0.057

Bibliography

[1] G. Binnig et al. 'Surface Studies by Scanning Tunneling Microscopy'. In: *Phys. Rev. Lett.* 49 (1982), 57.

[2] D. M. Eigler and E. K. Schweizer. 'Positioning single atoms with a scanning tunnelling microscope'. In: *Nature* 344 (1990), 524.

[3] R. M. Feenstra. 'Scanning tunneling spectroscopy'. In: *Surf. Sci.* 299-300 (1994), 965.

[4] J. Repp et al. 'Molecules on Insulating Films: Scanning-Tunneling Microscopy Imaging of Individual Molecular Orbitals'. In: *Phys. Rev. Lett.* 94 (2005), 026803.

[5] G. Binnig, C. F. Quate, and C. Gerber. 'Atomic Force Microscope'. In: *Phys. Rev. Lett.* 56 (1986), 930.

[6] L. Gross et al. 'The Chemical Structure of a Molecule Resolved by Atomic Force Microscopy'. In: *Science* 325 (2009), 1110.

[7] F. J. Giessibl. 'Atomic resolution on Si(111)-(7x7) by noncontact atomic force microscopy with a force sensor based on a quartz tuning fork'. In: *Appl. Phys. Lett.* 76 (2000), 1470.

[8] S.-W. Hla et al. 'Inducing All Steps of a Chemical Reaction with the Scanning Tunneling Microscope Tip: Towards Single Molecule Engineering'. In: *Phys. Rev. Lett.* 85 (2000), 2777.

[9] F. Mohn et al. 'Reversible Bond Formation in a Gold-Atom - Organic-Molecule Complex as a Molecular Switch'. In: *Phys. Rev. Lett.* 105 (2010), 266102.

[10] D. G. de Oteyza et al. 'Direct Imaging of Covalent Bond Structure in Single-Molecule Chemical Reactions'. In: *Science* 340 (2013), 1434.

[11] J. M. R. Weaver and D. W. Abraham. 'High resolution atomic force microscopy potentiometry'. In: *J. Vac. Sci. Technol. B* 9 (1991), 1559.

[12] M. Nonnenmacher, M. P. O'Boyle, and H. K. Wickramasinghe. 'Kelvin probe force microscopy'. In: *Appl. Phys. Lett.* 58 (1991), 2921.

[13] F. Mohn et al. 'Imaging the charge distribution within a single molecule'. In: *Nat. Nanotechnol.* 7 (2012), 227.

[14] B. Schuler et al. 'Contrast Formation in Kelvin Probe Force Microscopy of Single π-Conjugated Molecules'. In: *Nano Lett.* 14 (2014), 3342.

[15] G. Binnig et al. 'Tunneling through a controllable vacuum gap'. In: *Appl. Phys. Lett.* 40 (1982), 178.

[16] C. J. Chen. *Introduction to Scanning Tunneling Microscopy*. Oxford University Press, New York, 2008.

[17] G. Binnig and H. Rohrer. 'Scanning tunneling microscopy'. In: *Surf. Sci.* 126 (1983), 236.

[18] G. Binnig et al. '7 x 7 Reconstruction on Si(111) Resolved in Real Space'. In: *Phys. Rev. Lett.* 50 (1983), 120.

[19] J. Bardeen. 'Tunnelling from a Many-Particle Point of View'. In: *Phys. Rev. Lett.* 6 (1961), 57.

[20] J. Tersoff and D. R. Hamann. 'Theory and Application for the Scanning Tunneling Microscope'. In: *Phys. Rev. Lett.* 50 (1983), 1998.

[21] J. Tersoff and D. R. Hamann. 'Theory of the scanning tunneling microscope'. In: *Phys. Rev. B* 31 (1985), 805.

[22] R. Wiesendanger. *Scanning Probe Microscopy and Spectroscopy*. Oxford University Press, 2008.

[23] P. W. Anderson. 'Localized Magnetic States in Metals'. In: *Phys. Rev.* 124 (1961), 41.

[24] D. M. Newns. 'Self-Consistent Model of Hydrogen Chemisorption'. In: *Phys. Rev.* 178 (1969), 1123.

[25] D. Meschede, ed. *Gerthsen Physik*. Springer, Berlin, 2006.

[26] M. A. Lantz et al. 'Quantitative Measurement of Short-Range Chemical Bonding Forces'. In: *Science* 291 (2001), 2580.

[27] T. R. Albrecht and C. F. Quate. 'Atomic resolution imaging of a nonconductor by atomic force microscopy'. In: *J. Appl. Phys.* 62 (1987), 2599.

[28] G. Binnig et al. 'Atomic Resolution with Atomic Force Microscope'. In: *Europhys. Lett.* 3 (1987), 1281.

[29] J. E. Jones. 'On the Determination of Molecular Fields. II. From the Equation of State of a Gas'. In: *Proc. R. Soc. Lond. A* 106 (1924), 463.

[30] H. Hamaker. 'The London—van der Waals attraction between spherical particles'. In: *Physica* 4 (1937), 1058.

[31] F. J. Giessibl. 'Advances in atomic force microscopy'. In: *Rev. Mod. Phys.* 75 (2003), 949.

[32] F. J. Giessibl. 'Forces and frequency shifts in atomic-resolution dynamic-force microscopy'. In: *Phys. Rev. B* 56 (1997), 16010.

[33] J. E. Sader and S. P. Jarvis. 'Accurate formulas for interaction force and energy in frequency modulation force spectroscopy'. In: *Appl. Phys. Lett.* 84 (2004), 1801.

[34] F. J. Giessibl. 'A direct method to calculate tip-sample forces from frequency shifts in frequency-modulation atomic force microscopy'. In: *Appl. Phys. Lett.* 78 (2001), 123.

[35] T. R. Albrecht et al. 'Frequency modulation detection using high-Q cantilevers for enhanced force microscope sensitivity'. In: *J. Appl. Phys.* 69 (1991), 668.

[36] F. J. Giessibl. 'Atomic Resolution of the Silicon (111)-(7×7) Surface by Atomic Force Microscopy'. In: *Science* 267 (1995), 68.

[37] Y. Sugawara et al. 'Defect Motion on an InP(110) Surface Observed with Noncontact Atomic Force Microscopy'. In: *Science* 270 (1995), 1646.

[38] P. Samori, ed. *Scanning Probe Microscopies Beyond Imaging.* Wiley-VCH, 2006.

[39] Lord Kelvin. 'V. Contact electricity of metals'. In: *Philos. Mag.* 46 (1898), 82.

[40] W. A. Zisman. 'A new method of measuring contact potential difference in metals'. In: *Rev. Sci. Instrum.* 3 (1932), 367.

[41] K. Besocke and S. Berger. 'Piezoelectric driven Kelvin probe for contact potential difference studies'. In: *Rev. Sci. Instrum.* 47 (1976), 840.

[42] H. Wolter, M. Schmidt, and K. Wandelt. 'Surfactant induced layer-by-layer growth of Cu on Ru(0001) as revealed by oscillatory work function changes'. In: *Surf. Sci.* 298 (1993), 173.

[43] M. Pfeiffer, K. Leo, and N. Karl. 'Fermi level determination in organic thin films by the Kelvin probe method'. In: *J. Appl. Phys.* 80 (1996), 6880.

[44] R. Bennewitz et al. 'Aspects of Dynamic Force Microscopy on NaCl/Cu(111): Resolution, Tip-Sample Interactions and Cantilever Oscillation Characteristics'. In: *Surf. Interface Anal.* 27 (1999), 462.

[45] R. Stomp et al. 'Detection of Single-Electron Charging in an Individual InAs Quantum Dot by Noncontact Atomic-Force Microscopy'. In: *Phys. Rev. Lett.* 94 (2005), 056802.

[46] S. Hattori et al. 'Coulomb blockade behaviors in individual Au nanoparticles as observed through noncontact atomic force spectroscopy at room temperature'. In: *Nanotechnology* 23 (2012), 185704.

[47] N. Kocić et al. 'Periodic Charging of Individual Molecules Coupled to the Motion of an Atomic Force Microscopy Tip'. In: *Nano Lett.* 15 (2015), 4406.

[48] P. Rahe, R. P. Steele, and C. C. Williams. 'Consecutive Charging of a Molecule-on-Insulator Ensemble Using Single Electron Tunnelling Methods'. In: *Nano Lett.* 16 (2016), 911.

[49] R. Blaszczyszyn, M. Blaszczyszyn, and R. Meclewski. 'Work function of the adsorption system of potassium on tungsten'. In: *Surf. Sci.* 51 (1975), 396.

[50] T. V. W. Janssens et al. 'Surface potential around potassium promoter atoms on Rh(111) measured with photoemission of adsorbed Xe, Kr, and Ar'. In: *Phys. Rev. B* 49 (1994), 14599.

[51] K. Besocke, B. Krahl-Urban, and H. Wagner. 'Dipole moments associated with edge atoms; A comparative study on stepped Pt, Au and W surfaces'. In: *Surf. Sci.* 68 (1977), 39.

[52] K. Wandelt. 'The local work function: Concept and implications'. In: *Appl. Surf. Sci.* 111 (1997), 1.

[53] H. N. McMurray and G. Williams. 'Probe diameter and probe-specimen distance dependence in the lateral resolution of a scanning Kelvin probe'. In: *J. Appl. Phys.* 91 (2002), 1673.

[54] N. D. Lang and W. Kohn. 'Theory of Metal Surfaces: Work Function'. In: *Phys. Rev. B* 3 (1971), 1215.

[55] S. Kitamura, K. Suzuki, and M. Iwatsuki. 'High resolution imaging of contact potential difference using a novel ultrahigh vacuum non-contact atomic force microscope technique'. In: *Appl. Surf. Sci.* 140 (1999), 265.

[56] T. Hochwitz et al. 'Capacitive effects on quantitative dopant profiling with scanned electrostatic force microscopes'. In: *J. Vac. Sci. Technol. B* 14 (1996), 457.

[57] H. Jacobs et al. 'Surface potential mapping: A qualitative material contrast in SPM'. In: *Ultramicroscopy* 69 (1997), 39.

[58] H. Jacobs et al. 'Resolution and contrast in Kelvin probe force microscopy'. In: *J. Appl. Phys.* 84 (1998), 1168.

[59] L. Gross et al. 'Investigating atomic contrast in atomic force microscopy and Kelvin probe force microscopy on ionic systems using functionalized tips'. In: *Phys. Rev. B* 90 (2014), 155455.

[60] J. L. Neff and P. Rahe. 'Insights into Kelvin probe force microscopy data of insulator-supported molecules'. In: *Phys. Rev. B* 91 (2015), 085424.

[61] R. Smoluchowski. 'Anisotropy of the Electronic Work Function of Metals'. In: *Phys. Rev.* 60 (1941), 661.

[62] T. Glatzel, S. Sadewasser, and M. Lux-Steiner. 'Amplitude or frequency modulation-detection in Kelvin probe force microscopy'. In: *Appl. Surf. Sci.* 210 (2003), 84.

[63] U. Zerweck et al. 'Accuracy and resolution limits of Kelvin probe force microscopy'. In: *Phys. Rev. B* 71 (2005), 125424.

[64] Z. M. Ma et al. 'The stray capacitance effect in Kelvin probe force microscopy using FM, AM and heterodyne AM modes'. In: *Nanotechnology* 24 (2013), 225701.

[65] J. R. Matey and J. Blanc. 'Scanning capacitance microscopy'. In: *J. Appl. Phys.* 57 (1985), 1437.

[66] L. Gross et al. 'Measuring the Charge State of an Adatom with Noncontact Atomic Force Microscopy'. In: *Science* 324 (2009), 1428.

[67] S. Kawai et al. 'Atomic contact potential variations of Si(111)-7×7 analyzed by Kelvin probe force microscopy'. In: *Nanotechnology* 21 (2010), 245704.

[68] A. J. Weymouth et al. 'Phantom Force Induced by Tunneling Current: A Characterization on Si(111)'. In: *Phys. Rev. Lett.* 106 (2011), 226801.

[69] A. J. Weymouth and F. J. Giessibl. 'The effect of sample resistivity on Kelvin probe force microscopy'. In: *Appl. Phys. Lett.* 101 (2012), 213105.

[70] N. Pavlicek. 'Scanning Probe Methods Applied to Molecular Electronics'. PhD thesis. Universität Regensburg, 2013.

[71] M. Neu. 'Rasterkraftmikroskopie auf atomarer Skala: Van-der-Waals Wechselwirkung in molekularen Systemen'. PhD thesis. Universität Regensburg, 2013.

[72] G. Münnich. 'Cross-Sectional Scanning Probe Microscopy on GaAs: Tip-Induced Band Bending, Buried Acceptors and Adsorbed Molecules'. PhD thesis. Universität Regensburg, 2014.

[73] B. Voigtländer. *Scanning Probe Microscopy*. Springer, Berlin, 2015.

[74] F. Pielmeier et al. 'Impact of thermal frequency drift on highest precision force microscopy using quartz-based force sensors at low temperatures'. In: *Beilstein J. Nanotechnol.* 5 (2014), 407.

[75] D. R. Lide, ed. *CRC Handbook of Chemistry and Physics*. CRC press, 2009.

[76] W. Demtröder. *Experimentalphysik I*. Springer, 2008.

[77] J. Repp, G. Meyer, and K.-H. Rieder. 'Snell's Law for Surface Electrons: Refraction of an Electron Gas Imaged in Real Space'. In: *Phys. Rev. Lett.* 92 (2004), 036803.

[78] R. Bennewitz et al. 'Ultrathin films of NaCl on Cu(111): a LEED and dynamic force microscopy study'. In: *Surf. Sci.* 438 (1999), 289.

[79] L. Gross et al. 'Organic structure determination using atomic-resolution scanning probe microscopy'. In: *Nat. Chem.* 2 (2010), 821.

[80] N. Pavliček et al. 'Atomic Force Microscopy Reveals Bistable Configurations of Dibenzo[a,h]thianthrene and their Interconversion Pathway'. In: *Phys. Rev. Lett.* 108 (2012), 086101.

[81] I. Swart et al. 'Controlled Lateral Manipulation of Molecules on Insulating Films by STM'. In: *Nano Lett.* 12 (2012), 1070.

[82] D. M. Eigler, C. P. Lutz, and W. E. Rudge. 'An atomic switch realized with the scanning tunnelling microscope'. In: *Nature* 352 (1991), 600.

[83] L. Bartels, G. Meyer, and K.-H. Rieder. 'Controlled vertical manipulation of single CO molecules with the scanning tunneling microscope: A route to chemical contrast'. In: *Appl. Phys. Lett.* 71 (1997), 213.

[84] H. J. Lee and W. Ho. 'Single-Bond Formation and Characterization with a Scanning Tunneling Microscope'. In: *Science* 286 (1999), 1719.

[85] L. Gross et al. 'High-Resolution Molecular Orbital Imaging Using a p-Wave STM Tip'. In: *Phys. Rev. Lett.* 107 (2011), 086101.

[86] N. Pavliček et al. 'Symmetry Dependence of Vibration-Assisted Tunneling'. In: *Phys. Rev. Lett.* 110 (2013), 136101.

[87] S. P. Jarvis. 'Resolving Intra- and Inter-Molecular Structure with Non-Contact Atomic Force Microscopy'. In: *Int. J. Mol. Sci.* 16 (2015), 19936.

[88] L. Gross et al. *Noncontact Atomic Force Microscopy*. Ed. by S. Morita et al. Springer, 2015.

[89] A. Riss et al. 'Local Electronic and Chemical Structure of Oligo-acetylene Derivatives Formed Through Radical Cyclizations at a Surface'. In: *Nano Lett.* 14 (2014), 2251.

[90] S. Kawai et al. 'Atomically controlled substitutional boron-doping of graphene nanoribbons'. In: *Nat. Commun.* 6 (2015), 8098.

[91] T. Dienel et al. 'Resolving Atomic Connectivity in Graphene Nanostructure Junctions'. In: *Nano Lett.* 15 (2015), 5185.

[92] N. Pavliček et al. 'On-surface generation and imaging of arynes by atomic force microscopy'. In: *Nat. Chem.* 7 (2015), 623.

[93] B. Schuler et al. 'Unraveling the Molecular Structures of Asphaltenes by Atomic Force Microscopy'. In: *J. Am. Chem. Soc.* 137 (2015), 9870.

[94] B. Schuler et al. 'Reversible Bergman cyclization by atomic manipulation'. In: *Nat. Chem.* 8.8 (2016), 224.

[95] P. Ruffieux et al. 'On-surface synthesis of graphene nanoribbons with zigzag edge topology'. In: *Nature* 531 (2016), 489.

[96] J. Krüger et al. 'Tetracene Formation by On-Surface Reduction'. In: *ACS Nano* 10 (2016), 4538.

[97] N. Kocić et al. 'Control of Reactivity and Regioselectivity for On-Surface Dehydrogenative Aryl-Aryl Bond Formation'. In: *J. Am. Chem. Soc.* 138 (2016), 5585.

[98] Z. Majzik et al. 'Synthesis of a Naphthodiazaborinine and Its Verification by Planarization with Atomic Force Microscopy'. In: *ACS Nano* 10 (2016), 5340.

[99] H. Mönig et al. 'Submolecular Imaging by Noncontact Atomic Force Microscopy with an Oxygen Atom Rigidly Connected to a Metallic Probe'. In: *ACS Nano* 10 (2016), 1201.

[100] F. Mohn et al. 'Different tips for high-resolution atomic force microscopy and scanning tunneling microscopy of single molecules'. In: *Appl. Phys. Lett.* 102 (2013), 073109.

[101] W. Steurer et al. 'Toggling the Local Electric Field with an Embedded Adatom Switch'. In: *Nano Lett.* 15 (2015), 5564.

[102] N. Moll et al. 'The mechanisms underlying the enhanced resolution of atomic force microscopy with functionalized tips'. In: *New J. Phys.* 12 (2010), 125020.

[103] N. Moll et al. 'A simple model of molecular imaging with noncontact atomic force microscopy'. In: *New J. Phys.* 14 (2012), 083023.

[104] Z. Sun et al. 'Quantitative Atomic Force Microscopy with Carbon Monoxide Terminated Tips'. In: *Phys. Rev. Lett.* 106 (2011), 046104.

[105] M. Neu et al. 'Image correction for atomic force microscopy images with functionalized tips'. In: *Phys. Rev. B* 89 (2014), 205407.

[106] A. J. Weymouth, T. Hofmann, and F. J. Giessibl. 'Quantifying Molecular Stiffness and Interaction with Lateral Force Microscopy'. In: *Science* 343 (2014), 1120.

[107] P. Hapala et al. 'The mechanism of high-resolution STM/AFM imaging with functionalized tips'. In: *Phys. Rev. B* 90 (2014), 085421.

[108] N. Moll et al. 'Image Distortions of a Partially Fluorinated Hydrocarbon Molecule in Atomic Force Microscopy with Carbon Monoxide Terminated Tips'. In: *Nano Lett.* 14 (2014), 6127.

[109] C.-S. Guo et al. 'High-Resolution Model for Noncontact Atomic Force Microscopy with a Flexible Molecule on the Tip Apex'. In: *J. Phys. Chem. C* 119 (2015), 1483.

[110] N. Pavliček et al. 'High-resolution scanning tunneling and atomic force microscopy of stereochemically resolved dibenzo[a,h]-thianthrene molecules'. In: *Phys. Status Solidi B* 250 (2013), 2424.

[111] S. K. Hämäläinen et al. 'Intermolecular Contrast in Atomic Force Microscopy Images without Intermolecular Bonds'. In: *Phys. Rev. Lett.* 113 (2014), 186102.

[112] A. M. Sweetman et al. 'Mapping the force field of a hydrogen-bonded assembly'. In: *Nat. Ccommun.* 5 (2014), 3931.

[113] J. van der Lit et al. 'Submolecular Resolution Imaging of Molecules by Atomic Force Microscopy: The Influence of the Electrostatic Force'. In: *Phys. Rev. Lett.* 116 (2016), 096102.

[114] M. Ellner et al. 'The Electric Field of CO Tips and Its Relevance for Atomic Force Microscopy'. In: *Nano Lett.* 16 (2016), 1974.

[115] F. J. Giessibl. 'Advances in atomic force microscopy'. In: *Rev. Mod. Phys.* 75 (2003), 949.

[116] K. Ø. Hanssen et al. 'A Combined Atomic Force Microscopy and Computational Approach for the Structural Elucidation of Breitfussin A and B: Highly Modified Halogenated Dipeptides from Thuiaria breitfussi'. In: *Angew. Chem. Int. Ed.* 51 (2012), 12238.

[117] B. Schuler et al. 'Adsorption Geometry Determination of Single Molecules by Atomic Force Microscopy'. In: *Phys. Rev. Lett.* 111 (2013), 106103.

[118] C. Herranz-Lancho. 'Synthesis and Characterization of Molecules for Electronic Devices'. PhD thesis. Université de Strasbourg, 2013.

[119] M. Zander and W. H. Franke. 'Notiz über einfache Synthesen von Tetrabenzo[a,c,h,j]thianthren, Diphenanthro[9,10-b:9'10'-d]thiophen und Dibenzo[2,3:10,11]perylo[1,12-bcd]thiophen aus Phenanthren'. In: *Chem. Ber.* 106 (1973), 2752.

[120] F. Mohn, L. Gross, and G. Meyer. 'Measuring the short-range force field above a single molecule with atomic resolution'. In: *Appl. Phys. Lett.* 99 (2011), 53106.

[121] J. Cai et al. 'Atomically precise bottom-up fabrication of graphene nanoribbons'. In: *Nature* 466 (2010), 470.

[122] M. Treier et al. 'Surface-assisted cyclodehydrogenation provides a synthetic route towards easily processable and chemically tailored nanographenes'. In: *Nat. Chem.* 3 (2011), 61.

[123] J. Clayden et al. *Organic Chemistry.* Oxford University Press, 2001.

[124] H.-G. Franck and H. Buffleb. 'Kondensationsprodukte aus Phenanthren'. In: *Liebigs Ann. Chem.* 701 (1967), 53.

[125] A. Zhao et al. 'Controlling the Kondo Effect of an Adsorbed Magnetic Ion Through Its Chemical Bonding'. In: *Science* 309 (2005), 1542.

[126] S. Dahl et al. 'Role of Steps in N_2 Activation on Ru(0001)'. In: *Phys. Rev. Lett.* 83 (1999), 1814.

[127] R. T. Vang et al. 'Controlling the catalytic bond-breaking selectivity of Ni surfaces by step blocking'. In: *Nat. Mater.* 4 (2005), 160.

[128] F. Sedona et al. 'Tuning the catalytic activity of Ag(110)-supported Fe phthalocyanine in the oxygen reduction reaction'. In: *Nat. Mater.* 11 (2012), 970.

[129] W. Auwärter et al. 'A surface-anchored molecular four-level conductance switch based on single proton transfer'. In: *Nat. Nanotechnol.* 7 (2012), 41.

[130] C. Wäckerlin et al. 'Ammonia Coordination Introducing a Magnetic Moment in an On-Surface Low-Spin Porphyrin'. In: *Angew. Chem. Int. Ed.* 52 (2013), 4568.

[131] J. M. Gottfried. 'Surface chemistry of porphyrins and phthalocyanines'. In: *Surf. Sci. Rep.* 70 (2015), 259.

[132] M. Gottfried and H. Marbach. 'Surface-confined coordination chemistry with porphyrins and phthalocyanines: Aspects of formation, electronic structure, and reactivity'. In: *Z. physik. Chem.* 223 (2009), 53.

[133] W. Auwärter et al. 'Porphyrins at interfaces'. In: *Nat. Chem.* 7 (2015), 105.

[134] F. Buchner et al. 'Substrate-Mediated Phase Separation of Two Porphyrin Derivatives on Cu(111)'. In: *Chem. Eur. J.* 17 (2011), 10226.

[135] A. Wiengarten et al. 'Surface-Assisted Cyclodehydrogenation; Break the Symmetry, Enhance the Selectivity'. In: *Chem. Eur. J.* 21 (2015), 12285.

[136] S. Joshi et al. 'Control of Molecular Organization and Energy Level Alignment by an Electronically Nanopatterned Boron Nitride Template'. In: *ACS Nano* 8 (2014), 430.

[137] F. Bischoff et al. 'How Surface Bonding and Repulsive Interactions Cause Phase Transformations: Ordering of a Prototype Macrocyclic Compound on Ag(111)'. In: *ACS Nano* 7 (2013), 3139.

[138] W. Auwärter et al. 'Site-specific electronic and geometric interface structure of Co-tetraphenyl-porphyrin layers on Ag(111)'. In: *Phys. Rev. B* 81 (2010), 245403.

[139] W. Auwärter et al. 'Conformational Adaptation and Selective Adatom Capturing of Tetrapyridyl-porphyrin Molecules on a Copper (111) Surface'. In: *J. Am. Chem. Soc.* 129 (2007), 11279.

[140] A. Weber-Bargioni et al. 'Visualizing the Frontier Orbitals of a Conformationally Adapted Metalloporphyrin'. In: *Chem. Phys. Chem.* 9 (2008), 89.

[141] J. Xiao et al. 'Temperature-Dependent Chemical and Structural Transformations from 2H-tetraphenylporphyrin to Copper(II)-Tetraphenylporphyrin on Cu(111)'. In: *J. Phys. Chem. C* 116 (2012), 12275.

[142] M. Stark et al. 'Coverage Dependent Disorder-Order Transition of 2H-Tetraphenylporphyrin on Cu(111)'. In: *Langmuir* 29 (2013), 4104.

[143] M. Röckert et al. 'Abrupt Coverage-Induced Enhancement of the Self-Metalation of Tetraphenylporphyrin with Cu(111)'. In: *J. Phys. Chem. C* 118 (2014), 1661.

[144] K. Diller et al. 'Self-metalation of 2H-tetraphenylporphyrin on Cu(111): An x-ray spectroscopy study'. In: *J. Chem. Phys* 136 (2012), 014705.

[145] K. Seufert et al. 'Cis-dicarbonyl binding at cobalt and iron porphyrins with saddle-shape conformation'. In: *Nat. Chem.* 3 (2011), 114.

[146] F. Klappenberger. 'Two-dimensional functional molecular nanoarchitectures — Complementary investigations with scanning tunneling microscopy and X-ray spectroscopy'. In: *Prog. Surf. Sci.* 89 (2014), 1.

[147] W. Auwärter et al. 'Self-assembly and conformation of tetrapyridyl-porphyrin molecules on Ag(111)'. In: *J. Chem. Phys.* 124 (2006), 194708.

[148] T. Houwaart et al. 'Scrutinizing individual CoTPP molecule adsorbed on coinage metal surfaces from the interplay of STM experiment and theory'. In: *Surf. Sci.* 635 (2015), 108.

[149] L. Gross et al. 'Bond-order discrimination by atomic force microscopy'. In: *Science* 337 (2012), 1326.

[150] C. Moreno et al. 'Imaging Three-Dimensional Surface Objects with Submolecular Resolution by Atomic Force Microscopy'. In: *Nano Lett.* 15 (2015), 2257.

[151] S. P. Jarvis et al. 'Measuring the mechanical properties of molecular conformers'. In: *Nat. Commun.* 6 (2015), 8338.

[152] F. Moresco et al. 'Conformational Changes of Single Molecules Induced by Scanning Tunneling Microscopy Manipulation: A Route to Molecular Switching'. In: *Phys. Rev. Lett.* 86 (2001), 672.

[153] X. H. Qiu, G. V. Nazin, and W. Ho. 'Mechanisms of Reversible Conformational Transitions in a Single Molecule'. In: *Phys. Rev. Lett.* 93 (2004), 196806.

[154] J. Brede et al. 'Dynamics of molecular self-ordering in tetraphenyl porphyrin monolayers on metallic substrates'. In: *Nanotechnology* 20 (2009), 275602.

[155] F. Buchner et al. 'Ordering aspects and intramolecular conformation of tetraphenylporphyrins on Ag(111)'. In: *Phys. Chem. Chem. Phys.* 12 (2010), 13082.

[156] P. Stoltze. 'Simulation of surface defects'. In: *J. Phys.: Condens. Matter* 6 (1994), 9495.

[157] J. Repp et al. 'Substrate Mediated Long-Range Oscillatory Interaction between Adatoms: Cu /Cu(111)'. In: *Phys. Rev. Lett.* 85 (2000), 2981.

[158] J. Mielke et al. 'Adatoms underneath Single Porphyrin Molecules on Au(111)'. In: *J. Am. Chem. Soc.* 137 (2015), 1844.

[159] G. Rojas et al. 'Surface state engineering of molecule-molecule interactions'. In: *Phys. Chem. Chem. Phys.* 14 (2012), 4971.

[160] V. Iancu et al. 'Manipulating Kondo Temperature via Single Molecule Switching'. In: *Nano Lett.* 6 (2006), 820.

[161] S. P. Jarvis et al. 'Physisorption Controls the Conformation and Density of States of an Adsorbed Porphyrin'. In: *J. Phys. Chem. C* 119 (2015), 27982.

[162] C. Quest. 'Kombiniertes STM/AFM auf synthetischen Phenazin-Gold-Komplexen'. Diploma thesis. Universität Regensburg, 2011.

[163] G. Pawin et al. 'A Surface Coordination Network Based on Substrate-Derived Metal Adatoms with Local Charge Excess'. In: *Angew. Chem. Int. Ed.* 47 (2008), 8442.

[164] R. Gutzler et al. ‘Surface mediated synthesis of 2D covalent organic frameworks: 1,3,5-tris(4-bromophenyl)benzene on graphite(001), Cu(111), and Ag(110)’. In: *Chem. Commun.* 29 (2009), 4456.

[165] L. Grill et al. ‘Nano-architectures by covalent assembly of molecular building blocks’. In: *Nat. Nanotechnol.* 2 (2007), 687.

[166] L. Lafferentz et al. ‘Controlling on-surface polymerization by hierarchical and substrate-directed growth’. In: *Nat. Chem.* 4 (2012), 215.

[167] A. DiLullo et al. ‘Molecular Kondo Chain’. In: *Nano Lett.* 12 (2012), 3174.

[168] S. Maier et al. ‘Nanoscale Engineering of Molecular Porphyrin Wires on Insulating Surfaces’. In: *Small* 4 (2008), 1115.

[169] M. Kittelmann et al. ‘On-Surface Covalent Linking of Organic Building Blocks on a Bulk Insulator’. In: *ACS Nano* 5 (2011), 8420.

[170] J. R. Hahn and W. Ho. ‘Oxidation of a Single Carbon Monoxide Molecule Manipulated and Induced with a Scanning Tunneling Microscope’. In: *Phys. Rev. Lett.* 87 (2001), 166102.

[171] A. Shiotari et al. ‘Imaging Covalent Bonding between Two NO Molecules on Cu(110)’. In: *Phys. Rev. Lett.* 106 (2011), 156104.

[172] J. Repp et al. ‘Imaging Bond Formation Between a Gold Atom and Pentacene on an Insulating Surface’. In: *Science* 312 (2006), 1196.

[173] P. Liljeroth et al. ‘Single-Molecule Synthesis and Characterization of Metal - Ligand Complexes by Low-Temperature STM’. In: *Nano Lett.* 10 (2010), 2475.

[174] G. te Velde et al. ‘Chemistry with ADF’. In: *J. Comput. Chem.* 22 (2001), 931.

[175] J. Bjork, S. Stafstrom, and F. Hanke. 'Zipping Up: Cooperativity Drives the Synthesis of Graphene Nanoribbons'. In: *J. Am. Chem. Soc.* 133 (2011), 14884.

[176] J. Repp et al. 'Controlling the Charge State of Individual Gold Adatoms'. In: *Science* 305 (2004), 493.

[177] J. Repp, P. Liljeroth, and G. Meyer. 'Coherent electron-nuclear coupling in oligothiophene molecular wires'. In: *Nat. Phys.* 6 (2010), 975.

[178] F. E. Olsson et al. 'Multiple Charge States of Ag Atoms on Ultrathin NaCl Films'. In: *Phys. Rev. Lett.* 98 (2007), 176803.

[179] I. Swart, T. Sonnleitner, and J. Repp. 'Charge State Control of Molecules Reveals Modification of the Tunneling Barrier with Intramolecular Contrast'. In: *Nano Lett.* 11 (2011), 1580.

[180] J. E. Lennard-Jones. 'The electronic structure of some diatomic molecules'. In: *J. Chem. Soc. Faraday Trans.* 25 (1929), 668.

[181] L. Pauling. 'The Application of the Quantum Mechanics to the Structure of the Hydrogen Molecule and Hydrogen Molecule-Ion and to Related Problems'. In: *Chem. Rev.* 5 (1928), 173.

[182] P. W. Atkins. *Physical Chemistry.* Oxford University Press, 1998.

[183] R. G. Mortimer. *Physical Chemistry.* Ed. by J. Walker. Benjamin/Cummings Pub. Co., 1993.

[184] M. Petty. *Molecular Electronics: From Principles to Practice.* Wiley Series in Materials for Electronic & Optoelectronic Applications. John Wiley & Sons, 2007.

[185] S. A. Burke et al. 'Determination of the local contact potential difference of PTCDA on NaCl: a comparison of techniques'. In: *Nanotechnology* 20 (2009), 264012.

[186] S. Sadewasser et al. 'New Insights on Atomic-Resolution Frequency-Modulation Kelvin-Probe Force-Microscopy Imaging of Semiconductors'. In: *Phys. Rev. Lett.* 103 (2009), 266103.

[187] W. Steurer et al. ‘Manipulation of the Charge State of Single Au Atoms on Insulating Multilayer Films’. In: *Phys. Rev. Lett.* 114 (2015), 036801.

[188] T. Leoni et al. ‘Controlling the Charge State of a Single Redox Molecular Switch’. In: *Phys. Rev. Lett.* 106 (2011), 216103.

[189] W. Steurer et al. ‘Probe-based measurement of lateral single-electron transfer between individual molecules’. In: *Nat. Commun.* 6 (2015), 8353.

[190] P. Sartori and A. Golloch. ‘Darstellung und Eigenschaften von Tetrafluorphthalsäure-Derivaten’. In: *Chem. Ber.* 101 (1968), 2004.

[191] G. Wittig and F. Bickelhaupt. ‘o-Dilithium-benzol’. In: *Chem. Ber.* 91 (1958), 883.

[192] G. Kresse and J. Furthmüller. ‘Efficient iterative schemes for ab initio total-energy calculations using a plane-wave basis set’. In: *Phys. Rev. B* 54 (1996), 11169.

[193] J. D. Jackson. *Classical Electrodynamics*. Wiley, New York, 2001.

[194] A. Sadeghi et al. ‘Multiscale approach for simulations of Kelvin probe force microscopy with atomic resolution’. In: *Phys. Rev. B* 86 (2012), 075407.

[195] P. Hapala et al. ‘Origin of High-Resolution IETS-STM Images of Organic Molecules with Functionalized Tips’. In: *Phys. Rev. Lett.* 113 (2014), 226101.

[196] M. Corso et al. ‘Charge Redistribution and Transport in Molecular Contacts’. In: *Phys. Rev. Lett.* 115 (2015), 136101.

[197] D. Z. Gao et al. ‘Using Metallic Noncontact Atomic Force Microscope Tips for Imaging Insulators and Polar Molecules: Tip Characterization and Imaging Mechanisms’. In: *ACS Nano* 8 (2014), 5339.

[198] J. Gómez-Rodríguez, J. Gómez-Herrero, and A. Baró. 'Imaging cos(s, z): A method to separate the geometric and compositional contributions on STM barrier height profiles'. In: *Surf. Sci.* 220 (1989), 152.

[199] R. Schuster et al. 'Distance dependence and corrugation in barrier-height measurements on metal surfaces'. In: *Ultramicroscopy* 42 (1992), 533.

[200] S. Selci et al. 'STM topographic and barrier imaging of self-assembled InAs-GaAs dots'. In: *Mater. Sci. Eng.: B* 88 (2002), 168.

[201] M. Yoshitake and S. Yagyu. 'The effect of bias voltage on the measurement of local barrier height'. In: *Surf. Interface Anal.* 36 (2004), 1106.

[202] J. Kim et al. 'Quantum size effects on the work function of metallic thin film nanostructures'. In: *Proc. Natl. Acad. Sci. U.S.A.* 107 (2010), 12761.

[203] M. Becker and R. Berndt. 'Influence of band structure on the apparent barrier height in scanning tunneling microscopy'. In: *Phys. Rev. B* 81 (2010), 035426.

[204] M. Payne and J. Inkson. 'Measurement of workfunctions by tunnelling and the effect of the image potential'. In: *Surf. Sci.* 159 (1985), 485.

[205] C. D. Ruggiero, T. Choi, and J. A. Gupta. 'Tunneling spectroscopy of ultrathin insulating films: CuN on Cu(100)'. In: *Appl. Phys. Lett.* 91 (2007), 253106.

[206] F. Schulz et al. 'Epitaxial hexagonal boron nitride on Ir(111): A work function template'. In: *Phys. Rev. B* 89 (2014), 235429.

[207] A. Sakai. *Advances in Scanning Probe Microscopy*. Ed. by T. Sakurai and Y. Watanabe. Springer, Berlin, 2000.

[208] M. Herz et al. 'Simultaneous current-, force-, and work-function measurement with atomic resolution'. In: *Appl. Phys. Lett.* 86 (2005), 153101.

[209] J. Jia et al. 'Steps on the Au/Cu(111) surface studied by local work function measurement with STM'. In: *Appl. Phys. A* 66 (1998), 1125.

[210] T. Yamada, J. Fujii, and T. Mizoguchi. 'STM, STS, and local work function study of Cs/p-GaAs(1 1 0)'. In: *Surf. Sci.* 479 (2001), 33.

[211] L. Vitali et al. 'Portrait of the potential barrier at metal-organic nanocontacts'. In: *Nat. Mater.* 9 (2010), 320.

[212] T. Aoki and T. Yokoyama. 'Mapping the surface electrostatic potentials of Au(111) by using barrier-height measurements'. In: *Phys. Rev. B* 89 (2014), 155423.

[213] F. Huber et al. 'Intramolecular Force Contrast and Dynamic Current-Distance Measurements at Room Temperature'. In: *Phys. Rev. Lett.* 115 (2015), 066101.

[214] H.-C. Ploigt et al. 'Local work function changes determined by field emission resonances: NaCl/Ag(100)'. In: *Phys. Rev. B* 76 (2007), 195404.

[215] T. König et al. 'Work Function Measurements of Thin Oxide Films on Metals—MgO on Ag(001)'. In: *J. Phys. Chem. C* 113 (2009), 11301.

[216] L. Olesen et al. 'Apparent Barrier Height in Scanning Tunneling Microscopy Revisited'. In: *Phys. Rev. Lett.* 76 (1996), 1485.

[217] J. Kröger, H. Jensen, and R. Berndt. 'Conductance of tip-surface and tip-atom junctions on Au(111) explored by a scanning tunnelling microscope'. In: *New J. Phys.* 9 (2007), 153.

[218] S. J. Altenburg and R. Berndt. 'Local work function and STM tip-induced distortion of graphene on Ir(111)'. In: *New J. Phys.* 16 (2014), 053036.

[219] G. Münnich et al. 'Fixing the Energy Scale in Scanning Tunneling Microscopy on Semiconductor Surfaces'. In: *Phys. Rev. Lett.* 111 (2013), 216802.

[220] T. König et al. 'Measuring the Charge State of Point Defects on MgO/Ag(001)'. In: *J. Am. Chem. Soc.* 131 (2009), 17544.

[221] S. Kawai et al. 'Obtaining Detailed Structural Information about Supramolecular Systems on Surfaces by Combining High-Resolution Force Microscopy with ab Initio Calculations'. In: *ACS Nano* 7 (2013), 9098.

[222] Y. Liu, M. Weinert, and L. Li. 'Determining charge state of graphene vacancy by noncontact atomic force microscopy and first-principles calculations'. In: *Nanotechnology* 26 (2015), 035702.

[223] S. Duhm et al. 'PTCDA on Au(111), Ag(111) and Cu(111): Correlation of interface charge transfer to bonding distance'. In: *Organic Electronics* 9 (2008), 111.

[224] L. Romaner et al. 'Theoretical study of PTCDA adsorbed on the coinage metal surfaces, Ag(111), Au(111) and Cu(111)'. In: *New J. Phys.* 11 (2009), 053010.

[225] M. Eremtchenko, J. Schaefer, and F. Tautz. 'Understanding and tuning the epitaxy of large aromatic adsorbates by molecular design'. In: *Nature* 425 (2003), 602.

[226] Y. Miyahara et al. 'Kelvin Probe Force Microscopy by Dissipative Electrostatic Force Modulation'. In: *Phys. Rev. Appl.* 4 (2015), 054011.

[227] E. Inami and Y. Sugimoto. 'Accurate Extraction of Electrostatic Force by a Voltage-Pulse Force Spectroscopy'. In: *Phys. Rev. Lett.* 114 (2015), 246102.

[228] J. Murawski et al. ‘Pump-probe Kelvin-probe force microscopy: Principle of operation and resolution limits’. In: *J. Appl. Phys.* 118 (2015), 154302.

[229] J. Jahng et al. ‘Ultrafast pump-probe force microscopy with nanoscale resolution’. In: *Appl. Phys. Lett.* 106 (2015), 083113.

[230] T. L. Cocker et al. ‘An ultrafast terahertz scanning tunnelling microscope’. In: *Nature Photon.* 7 (2013), 620.

[231] M. Eisele et al. ‘Ultrafast multi-terahertz nano-spectroscopy with sub-cycle temporal resolution’. In: *Nature Photon.* 8 (2014), 841.

[232] D. Vanderbilt. ‘Soft self-consistent pseudopotentials in a generalized eigenvalue formalism’. In: *Phys. Rev. B* 41 (1990), 7892.

[233] J. P. Perdew et al. ‘Atoms, molecules, solids, and surfaces: Applications of the generalized gradient approximation for exchange and correlation’. In: *Phys. Rev. B* 48 (1993), 4978.

[234] G. Henkelman, A. Arnaldsson, and H. Jónsson. ‘A fast and robust algorithm for Bader decomposition of charge density’. In: *Comput. Mater. Sci.* 36 (2006), 354.

List of Abbreviations and Symbols

2H-TPP	free-base tetraphenylporphyrin
AFM	atomic force microscope/microscopy
ClAnCN	10-chloro-anthracene-9-carbonitrile
Cu-TPP	copper tetraphenylporphyrin
DFT	density functional theory
DPAT	diphenanthro[9,10-b:9',10'-d]thiophene
$F_{12}C_{18}Hg_3$	trimeric perfluoro-ortho-phenylene mercury
FM-AFM	frequency-modulation atomic force microscopy
$H_{12}C_{18}Hg_3$	trimeric ortho-phenylene mercury
HOMO	highest occupied molecular orbital
KPFS	Kelvin probe force spectroscopy
LJ	Lennard Jones
LUMO	lowest unoccupied molecular orbital
MALDI-TOF	matrix-assisted laser desorption and ionization – time of flight
NEXAFS	near-edge X-ray absorption fine structure
NMR	nuclear magnetic resonance
PTCDA	perylene-3,4,9,10-tetracarboxylic dianhydride
SPM	scanning probe microscopy
STM	scanning tunneling microscope/microscopy
STS	scanning tunneling spectroscopy
XPS	X-ray photoelectron spectroscopy

Δf	frequency shift
$\Delta f^\star$	maximum value of Kelvin parabola
Δz	vertical offset from STM setpoint
δz	bias voltage induced vertical relaxation of adsorbates
$\hbar$	reduced Planck constant
κ	inverse decay length of tunneling current
Φ	work function
ϕ	electrostatic potential
ϕ_b	barrier height for tunneling electrons
A	oscillation amplitude
C	electrostatic capacitance
CPD	(global) contract potential difference
e	elementary charge
E_F	Fermi energy
f	frequency
f_0	resonance frequency of free cantilever
I	tunneling current
k_0	spring constant of cantilever
k_ts	tip-sample coupling
L	length of cantilever beam
$LCPD$	local contact potential difference
m	oscillating mass
m_e	electron mass
p	electric dipole
Q	mechanical quality factor
q	localized charge
V	bias voltage
$V^\star$	maximum position of Kelvin parabola
z	tip-sample spacing

Contributors to this work

Most of the work presented throughout this thesis could not have been performed by one single person on its own. To do SPM on specialized molecules, state of the art chemistry is required for their synthesis. Only best available scientific know-how allows for reliable theory modeling of individual molecules including the metallic substrates they are adsorbed on.

The following list provides the relevant contributors to the projects of this thesis:

Chapter 5: DPAT molecules were synthesized by Coral Herranz-Lancho and Mario Ruben at the Karlsruhe Institute of Technology. They conducted NMR and MALDI-TOF experiments, too. Niko Pavliček performed a preliminary STM-based characterization of DPAT.

Chapter 6: This project was a collaboration between the Technical University of Munich and the University of Regensburg. Most experiments were performed in Regensburg together with Felix Bischoff. Data depicted in Fig. 6.4e was recorded by Felix Bischoff in Munich.

Chapter 7: Christina Quest and Ingmar Swart carried out preliminary STM experiments on the complex formation. The AFM experiments as well as the detailed investigation of the electronic structure of monomer and complex were done in collaboration with Mathias Neu. Ingmar Swart performed theory calculations on the orbital structures.

Chapters 8 and 9: $F_{12}C_{18}Hg_3$ and $H_{12}C_{18}Hg_3$ molecules were synthesized by Martin Fleischmann and Manfred Scheer at the chemistry department of the University of Regensburg. Martin Ondráček and Pavel Jelínek from the Nanosurf Lab in Prague performed DFT calculations on the adsorption geometry and the intramolecular charge distribution of these molecules. Leo Gross from the IBM research center in Zurich provided fruitful input for the discussion of κ mapping.

The experiments presented throughout this thesis required a state of the art SPM setup. The experience and the contributions of our group engineer Andreas Pöllmann were essential for the design, the build-up, and the maintenance of our low-temperature UHV equipment.

Acknowledgments

There were not only the immediate scientific contributions listed above but also quite some people who have accompanied me on the way through my postgraduate time. I would like to thank:

- First of all, I thank Jascha Repp for offering me the possibility to conduct research in his work group. In addition, I am grateful for his support throughout this time, and for offering projects of my own interest.

- I thank Andreas Pöllmann, the engineer of our group, without whom our work would not be possible. He was also the perfect office mate.

- I am grateful for Niko Pavliček's introduction to the automated data acquisition procedure and his help with the CPMD simulations.

- I acknowledge the cross-reading of this manuscript by Sujoy Karan.

- In addition to the collaborators within the team in Regensburg, I thank the entire work group for the nice working atmosphere.

- I thank Tobias Korn for his fast Raman spectroscopy characterization of our in house grown graphene samples — unfortunately, this project did not make it into this thesis.

- I am grateful for the main funding of my position through the RTG1570 — I thank Milena Grifoni for leading the RTG through both funding periods and I thank Robert Hrdina for his polite help in any kind of administrative issue in the framework of the RTG.
- I thank my parents. Not only for their financial support during the first part of my time at university, but also for their trust in me.

List of Publications

Papers

- F. Albrecht, F. Bischoff, W. Auwärter, J. Barth, and J. Repp. 'Direct identification and determination of conformational response in adsorbed individual non-planar molecular species using non-contact atomic force microscopy'. (submitted to Nano Letters).
- F. Albrecht, M. Fleischmann, M. Scheer, L. Gross, and J. Repp. 'Local tunneling decay length and Kelvin probe force spectroscopy'. In: *Phys. Rev. B* 92 (2015), 235443.
- J. Repp, F. Albrecht, M. Fleischmann, and M. Scheer. 'Visualisierung der Polarität chemischer Bindungen'. In: *Physik in unserer Zeit* 46 (2015), 266.
- F. Albrecht, J. Repp, M. Fleischmann, M. Scheer, M. Ondráček, and P. Jelínek. 'Probing Charges on the Atomic Scale by Means of Atomic Force Microscopy'. In: *Phys. Rev. Lett.* 115 (2015), 076101.
- F. Albrecht, N. Pavliček, C. Herranz-Lancho, M. Ruben, and J. Repp. 'Characterization of a Surface Reaction by Means of Atomic Force Microscopy'. In: *J. Am. Chem. Soc.* 137 (2015), 7424.
- F. Albrecht, M. Neu, C. Quest, I. Swart, and J. Repp. 'Formation and Characterization of a Molecule–Metal–Molecule Bridge in Real Space'. In: *J. Am. Chem. Soc.* 135 (2013), 9200.

- G. Münnich, F. Albrecht, C. Nacci, M. Utz, D. Schuh, K. Kanisawa, S. Fölsch, and J. Repp. 'Probing individual weakly-coupled π-conjugated molecules on semiconductor surfaces'. In: *J. Appl. Phys.* 112 (2012), 034312.

Presentations

- F. Albrecht, 'Combined STM/AFM applied to chemistry and charge distributions of single molecules', presented at the MOLESCO workshop, Regensburg (Sep. 2015)

- F. Albrecht, 'Identification of an On-Surface Reaction Pathway by Means of Atomic Force Microscopy', presented at the 7th International Workshop on Surface Physics (IWSP), Trzebnica (Jun. 2015)

- F. Albrecht, 'Scanning Probe Microscopy on Individual Organic Molecules', presented at the German-Thai Symposium on Nanoscience, Regensburg (May 2015).

- F. Albrecht, 'Combined STM/AFM on individual molecules – Geometry, electronic structure and chemical reactions', presented at the Talk Nano series of graduate school of Nanosceince, Regensburg (May 2015)

- F. Albrecht, 'Probing the Polar Nature of Bonds by means of Atomic Force Microscopy', presented at the DPG Frühjahrstagung, Berlin (Mar. 2015).

- F. Albrecht, 'Probing the Polar Nature of Bonds by means of Atomic Force Microscopy', presented at the High Resolution Scanning Probe Microscopy workshop (HRSPM), Prague (Feb. 2015)

- F. Albrecht, 'Distinguishing Cu-TPP and 2H-TPP adsorbed on Cu(111) in FM-AFM', presented at the E20 seminar, TUM, Munich (Feb. 2015)

Posters

- F. Albrecht, 'Structure determination of individual non-planar molecules by means of nc-AFM', presented at the 19th International Conference on non-contact Atomic Force Microscopy, Nottingham (Jul. 2016).

- F. Albrecht, 'Local Tunneling Decay Length and Kelvin Probe Force Spectroscopy', presented at the DPG Frühjahrstagung, Regensburg (Mar. 2016).

- F. Albrecht, 'Probing Charges on the Atomic Scale by Means of Atomic Force Microscopy', presented at the 598th WEH-Seminar on 'Frontiers in Scanning Probe Microscopy', Bad Honnef (Nov. 2015)

- F. Albrecht, 'Combined STM/AFM applied to chemistry of single molecules', presented at the International Conference on 'Single-Molecule Electronics', Regensburg (Sep. 2015).

- F. Albrecht, '3D structure determination of individual molecules by means of Atomic Force Microscopy', presented at the DPG Frühjahrstagung, Berlin (Mar. 2015).

- F. Albrecht, 'Kelvin Probe Force Microscopy on the submolecular scale', presented at the DPG Frühjahrstagung, Dresden (Mar. 2014).

- F. Albrecht, 'Combined STM/AFM study on cyclic trimeric perfluoro-ortho-phenylene mercury', presented at the 544th WEH-Seminar on 'Interactions with the Nanoworld: Local Probes with High Time, Energy and Force Resolution', Bad Honnef (Nov. 2013)
- F. Albrecht, 'Non-contact atomic force microscopy of individual organic molecules', presented at the International Workshop on 'Building Blocks for carbon-based electronics: From molecules to nanotubes', Regensburg (Apr. 2013).
- F. Albrecht, 'Combined STM/AFM study on cyclic trimeric perfluoro-ortho-phenylene mercury', presented at the DPG Frühjahrstagung, Regensburg (Mar. 2013).
- F. Albrecht, 'Combined STM/AFM study on LiF islands grown on Cu(331)', presented at the 15th International Conference on non-contact Atomic Force Microscopy, Český Krumlov (Jul. 2012).
- F. Albrecht, 'Non-contact atomic force microscopy of individual organic molecules', presented at the 14th International Conference on non-contact Atomic Force Microscopy, Lake Constance (Sep. 2011). **First prize in best poster award**